Spring 5-15-2017

Evolution of Olivine Crystallographic Preferred Orientation in the Upper Mantle -- Implications for the Interpretation of Seismic Anisotropy

Yuval Boneh
Washington University in St. Louis

Recommended Citation

Boneh, Yuval, "Evolution of Olivine Crystallographic Preferred Orientation in the Upper Mantle -- Implications for the Interpretation of Seismic Anisotropy" (2017). *Arts & Sciences Electronic Theses and Dissertations*. 1087.
https://openscholarship.wustl.edu/art_sci_etds/1087

WASHINGTON UNIVERSITY IN ST. LOUIS

Department of Earth and Planetary Sciences

Dissertation Examination Committee:
Philip Skemer, Chair
Katharine M. Flores
William B. McKinnon
Viatcheslav S. Solomatov
Douglas A. Wiens

Evolution of Olivine Crystallographic Preferred Orientation in the Upper Mantle – Implications for the Interpretation of Seismic Anisotropy

by
Yuval Boneh

A dissertation presented to
The Graduate School
of Washington University in
partial fulfillment of the
requirements for the degree
of Doctor of Philosophy

May 2017
St. Louis, Missouri

Table of Contents

List of Figures

List of Tables

Acknowledgments

Firstly, I would like to thank my mentor, Phil Skemer, for his continuous support during my path for graduation. Phil has encouraged me to think critically and develop my own views and was always open to share his experience or discuss my new research thoughts. I cannot thank him enough for his honest dedication for my growth as a scientist.

I would also like to thank my committee, Doug Wiens, Slava Solomatov, Bill McKinnon and Katharine Flores for their willing to invest time, meet, and discuss my research. During the last 5 years in the Rock Deformation lab I have been fortune to spend time, interesting discussions, and many coffee breaks with great people whom I learned a lot from: Brandon Mahan, Jolien Linckens, Rolf Bruijn, Héléne Couvy, Kelsey Prissel, Andrew Cross, Rachel Wells, Michael Sly, and Max Gavrilenko.

The department of Earth and Planetary sciences at Washington University in St. Louis has been a wonderful home for me for the last 5 years and gave me all the tools one could possible ask in terms of my academic and professional goals. I would also like to thank my dear friends: Katherine Becker, Amanda Bender, Karyn Blake, Vita Eruhimovitz, Cody Greer, Fabien Maillot, Garrecht Metzger, Merav Kweskin, Martin Pratt, and Olly Scott-Dye.

Lastly, I would like to thank my family. My Dad, Mum, and my two wonderful sisters for their boundless support and love throughout the years.

Yuval Boneh

Washington University in St. Louis

May 2017

“When you begin to see the possibilities of music, you desire to do something good for people, to help humanity free itself from its hang-ups” – John Coltrane

Dedicated to Jazz, and to the many Jazz musicians from whom I have been profoundly inspired, and learned the essence of devotion, passion and a deep sense of exploration.

ABSTRACT OF THE DISSERTATION

Evolution of Olivine Crystallographic Preferred Orientation in the Upper Mantle –
Implications for the Interpretation of Seismic Anisotropy

by

Yuval Boneh

Doctor of Philosophy in Earth and Planetary Sciences

Washington University in St. Louis, 2017

Professor Philip Skemer, Chair

Earth's plate tectonics is the outermost manifestation of mantle convection. Understanding plate tectonics at the global scale requires understanding of regional processes near plate boundaries. Flow patterns in the upper mantle are generally inferred from observations of anisotropy of seismic wave speed. In plate interiors, where flow patterns are assumed to be simple, interpretation of seismic anisotropy is straightforward. However, near plate boundaries, where flow patterns are complex, different strategies for interpreting seismic anisotropy may be required.

This dissertation examines, using experimental and numerical tools, the effects of complex flow patterns on the evolution of olivine crystallographic preferred orientation (CPO). Chapter 2 presents a set of experiments designed to simulate the effects of complex deformation histories on the evolution of olivine CPO. These experiments demonstrate that crystallographic re-alignment of olivine requires larger strains to reach steady state, compared to experiments with simpler deformation histories. In Chapter 3, we present numerical models that assess the effect of deformation history on olivine CPO evolution at high strains and with different deformation geometries. The models were benchmarked to the experiments described in Chapter

2, and from this analysis new model parameters are proposed that improve fit between experiments and numerical simulations. In Chapter 4, we assess the CPO predictions of numerical models under complex strain histories using data of CPO evolution from the literature as reference. The CPO is depicted and assessed using the textural strength, orientation, and symmetry. The CPO evolution from these texture elements indicates the similarities and differences between the two models and between the models and the reference CPOs. In Chapter 5, we examine whether a CPO of highly strained mantle is preserved during annealing. Through experiments under hydrostatic conditions we demonstrate a mechanism for which the CPO is modified with the microstructural recovery processes. It is concluded that seismic anisotropy in the upper mantle may be affected by the flow history, both under dynamic or static conditions.

Chapter 1: Introduction

It has long been recognized that the physical properties of many materials depend on their crystallographic orientation which is so often used by material scientists in designing materials with specific physical properties. Geomaterials are of no exception, many minerals exhibit intrinsic anisotropic properties due to their crystallographic symmetry and arrangement such as: diffusion-rate, fracture strength, viscous strength, elastic properties, electric properties, and magnetic properties. In order for the anisotropic properties of a single crystal to affect a polycrystalline sample the sample's crystals must constitute crystallographic texture – a crystallographic preferred orientation (CPO). Indeed, the process of intragranular plastic deformation may induce CPO in rock according to the deformation geometry and conditions (Wenk and Van Houtte, 2004; Wenk and Christie, 1991). Many minerals of Earth's crust, mantle, and core exhibit detectable CPO, such as: quartz (Law et al., 1990; Lloyd et al., 1992; Toy et al., 2008), feldspar (Jiang et al., 2000; Prior and Wheeler, 1999; Tullis and Yund, 1985), micas (Dempsey et al., 2011), halite (Wenk et al., 2009), calcite (Bestmann et al., 2000; Kern and Wenk, 1983), olivine (Ave'lallemant and Carter, 1970; Nicolas et al., 1973), post-perovskite (Merkel et al., 2007; Miyagi et al., 2010), and ε-iron (Antonangeli et al., 2004; Mao et al., 1998). This work is focused on the evolution of olivine CPO, the resulting elastic anisotropy, and the degree to which olivine CPO in the upper mantle represents current or past mantle flow.

Olivine comprises >60% of the upper mantle and is elastically anisotropic, therefore, forming olivine CPO in the mantle may significantly affect its properties. The development of CPO in olivine aggregates due to plastic deformation was found in experiments performed in the dislocation creep regime, under uniaxial compression (Ave'lallemant and Carter, 1970; Nicolas et al., 1973) and simple shear (Zhang and Karato, 1995; Zhang et al., 2000). Olivine CPO was interpreted to evolve according to two competing processes: dislocation-glide, which aligns the CPO with strain, and dynamic-recrystallization, which aligns the CPO with the stress regime (Karato, 1987). Zhang and Karato (1995) have demonstrated through simple shear experiments that the olivine fast [100] axis aligns with the direction of shear, indicating that the dominant process in creating olivine CPO is kinematic. However, syn-deformational recovery process that align the olivine with the stress axes can also affect the CPO and may be related to the activity of grain-boundary-migration (Ave Lallemant, 1975; Lee et al., 2002).

Elastic anisotropy in the upper mantle was first recognized by the work of Hess (1964) and later was integrated in the global preliminary reference Earth model – PREM (Dziewonski and Anderson, 1981). Ever since, there has been on-going investigation of seismic anisotropy of the upper mantle, mainly using shear wave splitting and surface waves, in order to infer upper mantle deformation and kinematics regimes (e.g., Becker et al., 2003; Savage, 1999). Olivine is elastically anisotropic, with P and S -wave velocity anisotropy of 23.8% and 16.0%, respectively. Since olivine is elastically anisotropic and ubiquitous in the upper mantle, it is believed to be the main cause for the anisotropy in the upper mantle (e.g., Karato and Wu, 1993). Indeed, natural sample from the mantle, xenoliths and obducted ophiolites, have demonstrated that olivine CPO is indeed a pervasive phenomenon in the upper mantle (Ben Ismaïl and Mainprice, 1998; Boullier and Nicolas, 1975). For interpreting seismic anisotropy, a simplify view in which shear direction (i.e., mantle flow) is aligned with olivine's crystallographic texture, is often used and is based on Zhang and Karato experiments in simple shear (1995) and on a database of natural olivine CPO's published by Ben-Ismail and Mainprice (1998). Although this paradigm has been useful in modeling much of the seismic anisotropy in the upper mantle, in more complex mantle flow regimes these simplified assumptions may not be accurate (Becker et al., 2014; Castelnau et al., 2006; Skemer and Hansen, 2016b; Skemer et al., 2012). In addition, observations of olivine CPO evolution in mantle shear zones indicated that starting with the ambient regional CPO may complicate and affect the CPO evolution (Skemer et al., 2010; Warren et al., 2008; Webber et al., 2010).

Here I investigate the effect of a previous stage of deformation on olivine CPO evolution through deformation (Chapter 2 - 4) and under static conditions (Chapter 5). I will explore the implications of these results to the way seismic anisotropy is interpreted as mantle kinematics.

Chapter 2: The effect of deformation history on the evolution of olivine CPO

An edited version of this chapter was published by *Earth and Planetary Science Letters*.

Boneh, Y., and P. Skemer (2014), The effect of deformation history on the evolution of olivine CPO, *Earth Planet. Sci. Lett.*, *406*(0), 213-222, doi:10.1016/j.epsl.2014.09.018.

Abstract

Olivine crystallographic preferred orientation (CPO) is the primary cause of seismic anisotropy in the upper mantle. In tectonic environments with complex flow patterns, for example corner flow near mid-ocean ridges or subducting slabs, the interpretation of seismic anisotropy may be complicated by evolving thermochemical deformation conditions and the integrated deformation history. To understand how deformation history influences CPO evolution, deformation experiments were conducted on samples of Åheim dunite, which has a strong pre-existing texture. Experiments were performed in a triaxial geometry using a Griggs apparatus at P = 1 GPa, T = 1473 K, up to a maximum strain of ~0.7. To simulate different deformation histories, samples were deformed in three different configurations, with the pre-existing foliation perpendicular, oblique, and parallel to the shortening axis of deformation. Distinct patterns of CPO development are observed for each experimental configuration. Likewise, texture strength, symmetry, and orientation evolved differently in each set of experiments. These data are interpreted as evidence that CPO did not reach steady state and that achieving steady state texture requires larger strains than previously thought. It is concluded that the integrated deformation history plays a significant role in CPO evolution and the consequent interpretation of seismic anisotropy in Earth's mantle.

2.1 Introduction

Olivine is the most abundant mineral in the upper mantle and its rheology plays an important role in mantle convection and the dynamics of Earth's tectonic plates (Hirth and Kohlstedt, 2003; Karato and Wu, 1993). Over a wide range of deformation conditions, strained crystal lattices align themselves in particular patterns described as crystallographic preferred orientation (CPO). The formation and evolution of CPO in olivine is related to the kinematics of flow (Karato, 1988; Wenk and Christie, 1991), the magnitude of strain (Nicolas et al., 1973; Skemer et al., 2012; Zhang and Karato, 1995), and the thermodynamic conditions of deformation (Couvy et al., 2004; Jung et al., 2006; Katayama and Karato, 2006; Raterron et al., 2007). The CPO generated by olivine deformation is widely considered to be the primary cause for seismic anisotropy in the upper mantle (Karato et al., 2008; Long and Becker, 2010; Mainprice et al., 2000; Nicolas and Christensen, 1987; Savage, 1999), and may also play an important role in the generation of rheological anisotropy (Hansen et al., 2012a; Montési, 2013; Skemer et al., 2013; Tommasi et al., 2009).

The most common olivine texture, which is developed by the dominant activity of the [100](010) slip system, aligns the olivine’s seismically fastest crystallographic axis [100] with the direction of flow. This A-type texture has been widely observed in both natural samples (Ben Ismaïl and Mainprice, 1998; Nicolas and Christensen, 1987) and laboratory deformation experiments (Zhang and Karato, 1995). The ubiquity of these observations provides a strong basis for the inferring mantle flow patterns from seismic anisotropy (Montagner, 2002; Montagner and Tanimoto, 1991; Savage, 1999; Silver et al., 1999; Tanimoto and Anderson, 1985) and for the parameterization of models that predict seismic anisotropy from numerical simulations of mantle flow (Becker et al., 2003; Becker et al., 2006; Conrad et al., 2007; Faccenda and Capitanio, 2012; Kaminski and Ribe, 2001; Tommasi et al., 2000).

To infer mantle flow from seismic anisotropy, important assumptions must be made about the rate that CPO evolves. Specifically, it is necessary to assume that a steady state texture develops quickly and does not lag significantly behind changes in kinematics (Kaminski et al., 2004). However, recent experimental (Hansen et al., 2014; Skemer et al., 2011), geological (Skemer et al., 2010; Warren et al., 2008; Webber et al., 2010), and numerical studies (Castelnau et al., 2009) have shown that olivine CPO may evolve more slowly than previously thought. Of particular importance may be the influence of pre-existing olivine CPO on subsequent texture evolution (Skemer et al., 2012). In settings of complex mantle flow, such as mid-ocean ridges and mantle wedges of subduction zones, the kinematics and the conditions of deformation change rapidly over short length scales (Leo et al., 2014; Li et al., 2014). Yet in spite of its importance to the interpretation of seismic anisotropy, the effect of deformation history on subsequent texture evolution is poorly understood.

To explore the influence of deformation history on texture evolution in olivine, we have conducted high pressure/temperature laboratory deformation experiments on dunite with a pre-existing CPO. Experiments were conducted in three different configurations, to simulate three deformation histories. These experiments demonstrate that the accumulation of CPO depends strongly on the initial orientation of the pre-existing CPO, with respect to the geometry of deformation.

2.2 Methods

2.2.1 Starting material and experimental procedure

Triaxial deformation experiments were performed using a solid medium Griggs apparatus at a confining pressure of 1 GPa, temperature of 1200°C, and strain rates of $3.9 – 5.4*10^{-6}$ [1/sec] (Table 2.1). The starting material for these experiments is the Åheim dunite, which is composed mainly of olivine (~95%), with small amount of orthopyroxene (~2%), chlorite (~2%), and spinel (~1%) (Chopra and Paterson, 1981), and has been used in numerous laboratory experiments (Berckhemer et al., 1982; Chopra and Paterson, 1981, 1984; Druiventak et al., 2011; Jackson et al., 1992; Jin et al., 1994; Keefner et al., 2005; Van der Wal et al., 1993; Wendt et al., 1998). The Åheim dunite was chosen specifically for its coarse grain-size (~0.3 mm)(Fig. 2.1A) and for its relatively strong initial texture (Fig. 2.1B).

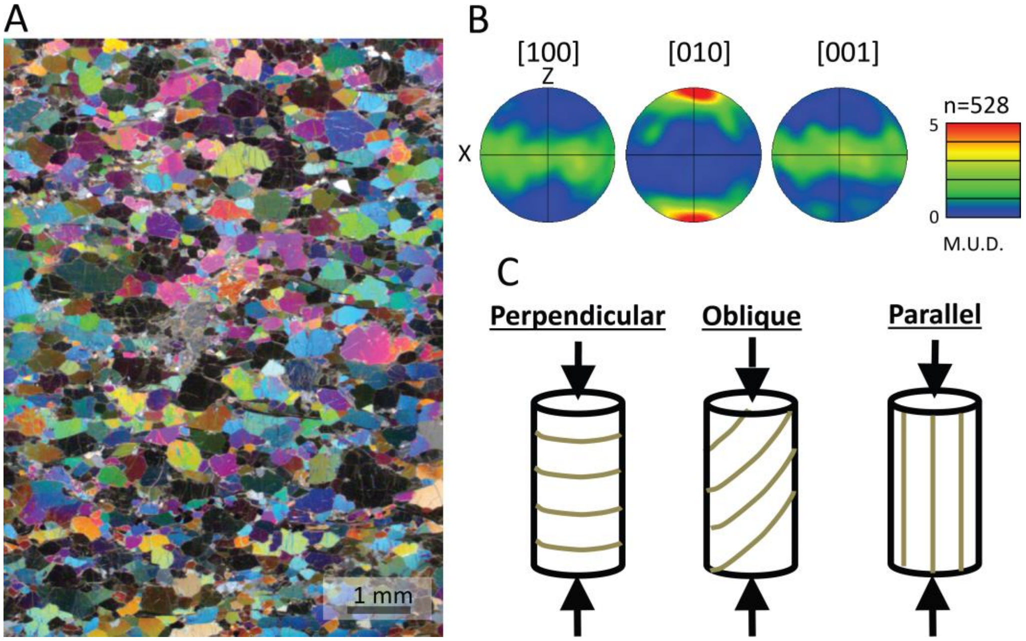

Figure 2.1 – (A) Microstructure of undeformed Åheim dunite in cross-polarized transmitted light. (B) Pole figures of olivine's pre-existing crystal preferred orientation (CPO). Olivine exhibits a point maximum of [010] axes, perpendicular to the foliation plane, and well-developed girdles of the [100] and

[001] crystal axes parallel to the foliation plane. n is the number of unique grains in the dataset. Color contours are multiples of uniform distribution (MUD), which ranges from zero (blue) to five (red). (C) Three experimental configuration described in this study, with the foliation (brown lines) perpendicular, oblique, and parallel to the existing foliation. Thick black arrows show the direction of shortening.

Samples were obtained from the same block characterized by (Jackson et al., 1992). Cores, extracted using a diamond coring bit, were ground into right cylinders with a diameter of 5.1 mm and with a length of 12.0 mm. Samples were cored in three different orientations with respect to the sample foliation. In the first orientation, the sample’s long axis, which is also the axis of shortening and the coring direction, is perpendicular to the foliation plane (Fig. 2.1C, henceforth this geometry is described to be "perpendicular"). In the second orientation, the sample core is at 45° to the foliation plane (Fig. 2.1C, "oblique"). In the third orientation, the sample core is parallel to the foliation plane (Fig. 2.1C, "parallel").

Samples were encased in a nickel capsule with a small amount of NiO powder added at the top of the capsule to buffer oxygen fugacity within the stability field of olivine (Nitsan, 1974). Prior to the experiment, samples were dried in a vacuum oven for a minimum of 24 h at 120°C to evaporate any adsorbed surface water. For high pressure and temperature experiments in the Griggs apparatus, soft-fired pyrophyllite, porous MgO, and barium carbonate, were used to form the confining pressure medium. This assembly is employed for its stability at high temperatures, allowing us to achieve maximal strains at strain-rates consistent with deformation by the dislocation creep mechanism. However, this pressure medium imposes substantial friction on the sigma-1 piston, limiting the utility of the mechanical data collected by the load cell. For each experiment, the sample was pressurized and heated slowly, over a period of 12 hours, in order to minimize premature deformation of the sample. When the target temperature and pressure was achieved, deformation was initiated at a constant strain-rate. A hit-point was observed in the load - displacement record after a run-in of ~4 mm. Samples quenched at the hit-point confirm some pre-hit strain (ε~0.2), but with relatively little recrystallization or modification of the microstructure. Experimental conditions and data are summarized in Table 2.1.

Table 2.1 – Summary of experiments parameters and texture elements. All experiments are under conditions of ∼1 GPa and 1200° C respectively.

Exp #	Configu-ration	Natural Strain	Strain-rate [1/sec]	ϴ°	M - index	[100] P	[100] G	[100] R	[010] P	[010] G	[010] R	[001] P	[001] G	[001] R
UF	-	0.000	-	0	0.13	0.012	0.517	0.471	0.450	0.160	0.390	0.065	0.384	0.449
116	perp	0.217	*	0	0.10	0.008	0.300	0.692	0.374	0.103	0.524	0.037	0.459	0.505
114	perp	0.328	4.55E-06	0	0.09	0.108	0.256	0.636	0.362	0.032	0.606	0.112	0.271	0.617
125	perp	0.406	4.27E-06	0	0.08	0.083	0.228	0.690	0.336	0.065	0.599	0.102	0.293	0.605
122	perp	0.507	3.91E-06	0	0.12	0.082	0.380	0.538	0.424	0.049	0.527	0.072	0.346	0.582
126	perp	0.653	4.43E-06	0	0.11	0.073	0.449	0.478	0.409	0.087	0.503	0.033	0.333	0.634
130	obl	0.187	*	33	0.09	0.033	0.361	0.607	0.368	0.074	0.558	0.061	0.319	0.620
128	obl	0.410	4.08E-06	30	0.08	0.065	0.258	0.677	0.327	0.105	0.567	0.018	0.401	0.581
129	obl	0.482	3.77E-06	18	0.14	0.171	0.297	0.533	0.437	0.084	0.479	0.148	0.306	0.546
143	obl	0.685	5.35E-06	17	0.15	0.211	0.292	0.497	0.450	0.127	0.423	0.149	0.316	0.534
127	obl	0.717	4.78E-06	0	0.15	0.209	0.315	0.476	0.446	0.069	0.486	0.178	0.254	0.568
138	para	0.207	*	80	0.06	0.032	0.156	0.812	0.217	0.227	0.556	0.140	0.220	0.640
133	para	0.360	4.50E-06	50	0.06	0.107	0.114	0.779	0.141	0.379	0.480	0.207	0.136	0.657
146	para	0.370	4.45E-06	55	0.06	0.125	0.121	0.754	0.180	0.332	0.488	0.117	0.165	0.718
134	para	0.415	4.27E-06	25	0.05	0.076	0.126	0.798	0.044	0.486	0.471	0.210	0.063	0.727
147	para	0.610	4.94E-06	40	0.06	0.142	0.179	0.679	0.061	0.544	0.395	0.139	0.020	0.841

* - strain occurred during initial loading of the sample and strain-rate is poorly constrained.
ϴ° - angle between the normal to the shear plane and the [010] point maxima.
'Exp' – experiments; 'UF' – Undeformed; 'perp' – perpendicular; 'obl' – oblique; 'para' - parallel

2.2.2 Microstructural and chemical analysis

Following each experiment, the sample was removed from the pressure medium and a 30 micron thick petrographic thin section was prepared parallel to the axis of compression and perpendicular to the initial foliation. The normal to the thin section plane, for samples in oblique and parallel geometries, is oriented parallel to the strike of the pre-existing foliation. Thin-sections were polished using progressively fine SiC and diamond abrasives. A final chemical-mechanical polish in colloidal silica was used to prepare the thin section for electron microscopy. CPO were measured using a JEOL 7001-FLV SEM system with an Oxford Instruments Electron Backscatter Diffraction (EBSD) detector. The SEM was run in a low vacuum mode to prevent charging of the sample surface. Analyses were performed at an acceleration voltage of 20 keV and a beam current of 18 nA. The stage was tilted at 70° to the electron beam with working distance of 23-25 mm. All samples were analyzed by rastering the beam across the sample in 5 micron steps. The area analyzed by EBSD with a 5 micron step size ranged from 4-10 mm^2. An equivalent area in the starting material contains 50-150 unique grains. EBSD mapping produced data sets with 500-3000 unique recrystallized grains. Although these datasets are small for quantitative texture study (Skemer et al., 2005), we are limited by the relatively small ratio of the experimental sample size to the initial grain size. Data were analyzed using the Oxford Instruments Channel 5 software package. Numerical smoothing was used to fill un-indexed points when a minimum of five adjacent pixels was found to have a common orientation. Two additional corrections for the indexed data were performed: (1) We apply a correction for olivine mis-indexing due to olivine pseudo-symmetry (e.g., Fliervoet et al., 1999). (2) Using an underlying band contrast image, large individual grains with a few separated numerical domains of a common orientation were manually interpolated to produce a single grain. Comparisons of smoothed and unmodified data were used to ensure that no artifacts resulted from the smoothing procedure. Individual grains were identified based on continuous domains with consistent orientations. Pole figures were plotted using one data point per grain. In recrystallized materials with narrow grain-size distributions, one point per grain analyses are effectively equivalent to volume weighted analyses. Except at the lowest strains, the experimental samples are almost completely recrystallized, so there is little bias imposed by the one point per grain method. Grains with less than four contiguous pixels of constant orientation points were excluded from the data set in order to avoid skewing results with spurious data.

Several scalar elements of texture are calculated, including strength, symmetry, and orientation, to quantify how different aspects of texture evolve during these experiments. Texture strength was calculated using the M-index (Skemer et al., 2005). The M-index is scaled such that a random CPO has M = 0 and a single crystal has M = 1. Texture symmetry was quantified by the three eigenvalues of each pole figure (using the Unicef Careware software, Mainprice (1990)) according to the following relations (Vollmer, 1990):

$$P = \lambda_1 - \lambda_2 \tag{2.1}$$

$$G = 2(\lambda_2 - \lambda_3) \tag{2.2}$$

$$R = 3\lambda_3 \tag{2.3}$$

where P represents the strength of the pole figure's point maxima, G represents the degree to which the pole figure exhibits a girdled texture, and R is the random element of texture. Eigenvalues are ranked such that $\lambda_1 \geq \lambda_2 \geq \lambda_3$ and $\lambda_1+\lambda_2+\lambda_3=P+G+R=1$. Finally, the orientations of crystal axes with respect to the kinematics of deformation were measured. The orientation of a point maximum in a particular pole figure was determined by the position of the greatest density of points. Error bars were set by the full width of the point maxima at half of the maximum amplitude.

Although experiments were conducted under nominally dry conditions, water content was measured using Fourier transform infrared spectroscopy (FTIR) on double polished thick sections (30-175 microns thick). FTIR was performed using a Digital Excalibur 3000 spectrometer, UMA-600 microscope, and a KBr beam-splitter. Unpolarized IR absorption spectra was recorded for 8-10 arbitrarily oriented crystals for undeformed Åheim dunite and from six deformed samples with a range of strains and experiment durations. Water concentrations were determined using the Paterson (1982) calibration, adjusted by a factor of 3 to agree with the updated calibration of Bell et al. (2003).

2.3 Results

EBSD maps of undeformed Åheim dunite and recrystallized grains in samples deformed in perpendicular, oblique, and parallel configurations are shown in Figure 2.2. Grain-sizes, calculated using the line intercept method with a stereological correction factor of 1.5 (Mendelson, 1969) are 350±70 μm for the undeformed sample and 30±20 μm for the recrystallized grains in deformed samples. Most of the samples deformed to high strains are recrystallized and the grain size appears to reach a steady state that is assumed to be controlled by the stress applied during deformation.

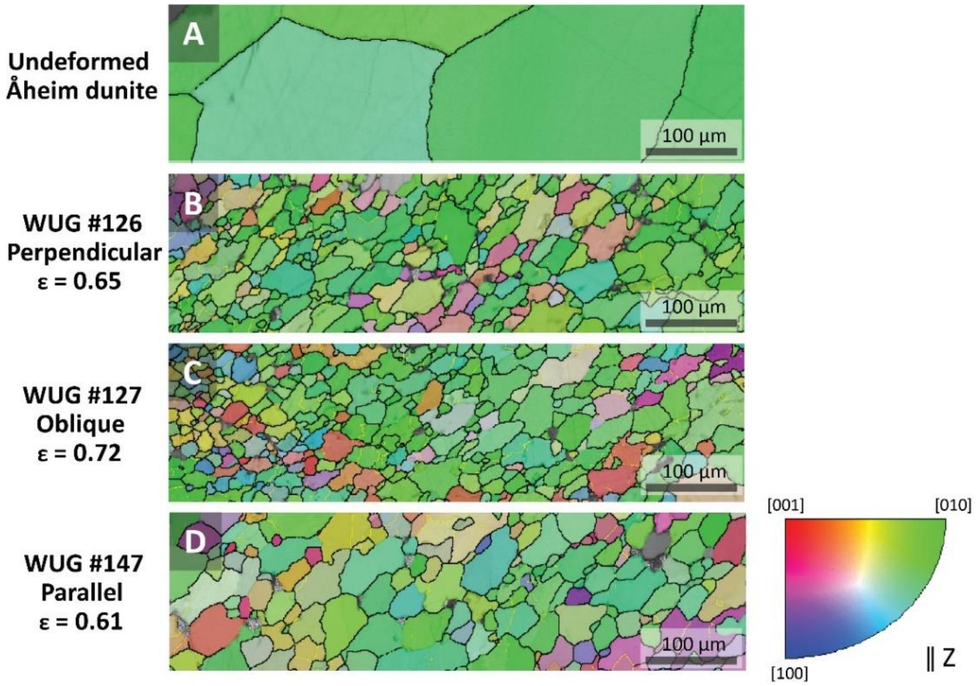

Figure 2.2 –EBSD maps of (A) undeformed Åheim dunite, and recrystallized grains of samples deformed in (B) perpendicular, (C) oblique, and (D) parallel configurations. Maps are generated with one-micron resolution. Strain is denoted by ε. The undeformed dunite grain-size is about a magnitude of order larger than the recrystallized grain-sizes. Coloration shows the orientation of grains relative to the axis of shortening (Z-direction). The predominant green color reflects the large number of grains that are oriented with [010] parallel to Z. Grain boundaries, shown by black lines, are crystallographic interfaces with a misorientation of >10 degrees. Subgrain boundaries with misorientation of 2-10 degrees are shown as thin yellow lines.

Water concentration measurements confirm that the initial water content in the olivine starting material (4000±2000 ppm H/Si) was reduced to below the detection limit for the FTIR spectrometer (<150 ppm H/Si) in all deformed samples analyzed. These results suggest that any water present in the olivine or produced by dehydration of the chlorite diffused out of the samples during the initial heating and pre-hit annealing stages (8-12 hours). This is consistent with the diffusion rate of hydrogen in olivine (Mackwell and Kohlstedt, 1990), which at these conditions predicts a time scale for water loss on the order of ~1-2 hours. Therefore, the samples were deformed at conditions considered to be effectively dry.

CPO data for 15 experiments in three configurations illustrate the effect of deformation history on the texture evolution. Figure 2.3 shows the pole figures for each series of experiments, arranged from the lowest to the highest strains. The first row of the figure shows the initial CPO of the Åheim dunite in each of its configurations. Each series of experiments evolves differently.

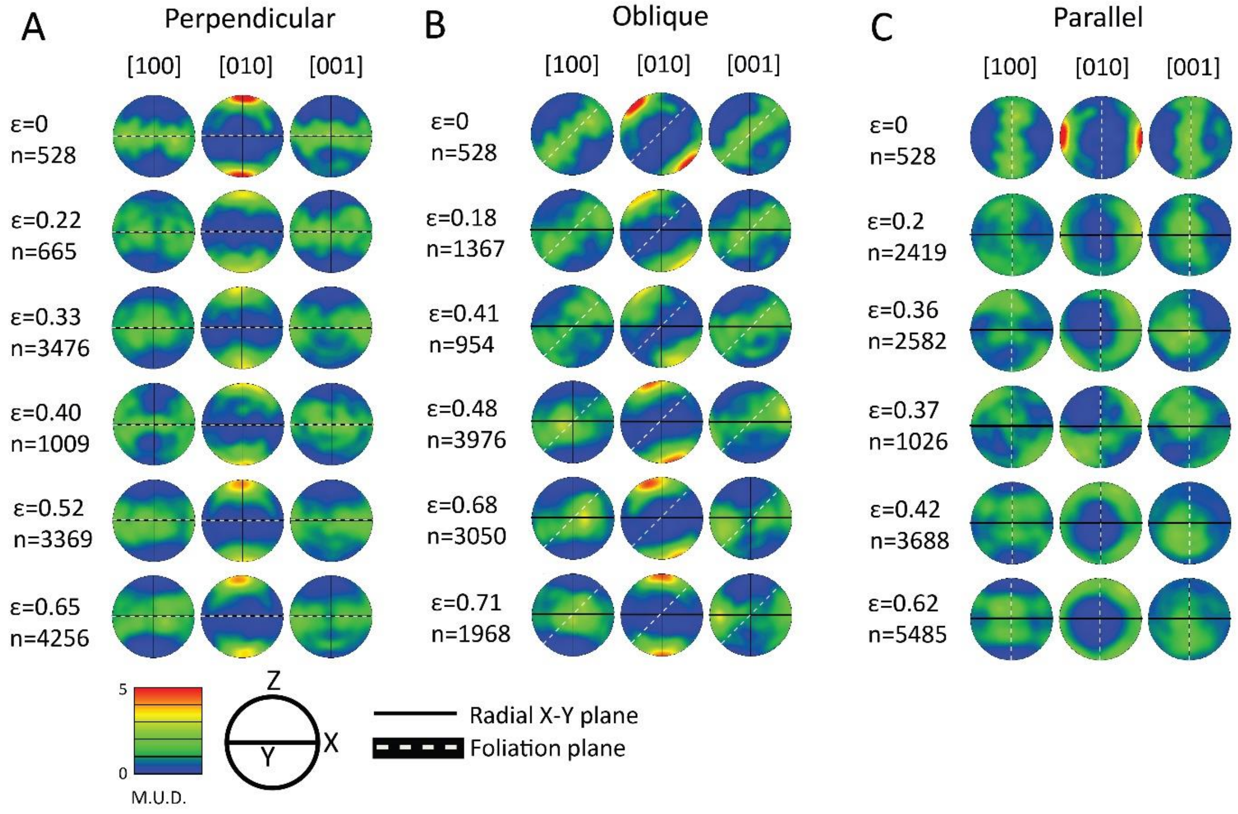

Figure 2.3 – Upper hemisphere pole figures showing the CPO evolution with strain for perpendicular (A), oblique (B), and parallel experiments (C). The thick horizontal line is the (X-Y) plane. Z is the shortening axis. The dashed line shows schematically the initial orientation of the foliation in the starting material. The first pole figure in each column represents the initial texture, which differs only by its initial orientation relative to the kinematics of deformation. Strain (ε) increases from top to bottom. n is the number of (Skemer et al., 2005) unique grains in the dataset. Color contours are multiples of uniform distribution (MUD).

Samples deformed in the perpendicular configuration (Fig. 2.3A) develop a [010] point maximum that is parallel to the axis of shortening. An axi-symmetric girdle develops in the [100] and [001] pole figures, which is similar in orientation to the starting material. There is no rotation of the CPO as a function of strain. Samples deformed in the oblique configuration (Fig. 2.3B) exhibit progressive rotation of [010] point maxima from an initial orientation perpendicular to the foliation towards the axis of shortening (Z). There is also an associated rotation of [100] and [001] girdles towards the radial (X-Y) plane. Within this girdle, a secondary [100] point maximum develops parallel to the initial strike of the foliation, which can be seen in the Y-direction of the pole figure. At the largest strains, the CPO of the samples in the perpendicular and oblique configurations are similar. Samples deformed in the parallel configuration (Fig. 2.3C) exhibit a dispersed CPO, with the [010] point maximum becoming progressively distributed in a girdle perpendicular to the radial plane and parallel to the shortening axis. Even at the largest strains, samples deformed in the parallel configuration do not approach the same CPO pattern achieved in the perpendicular and oblique configurations.

Figure 2.4A shows the evolution of CPO strength as a function of strain for the samples deformed in perpendicular (red circles), oblique (orange triangles), and parallel (yellow squares) configurations. CPO strength does not stabilize at a finite value over the range of strains achieved in the experiments. Moreover, for each of the three sets of experiments the strength of the CPO evolves differently. Samples deformed in the perpendicular configuration undergo an initial decrease, followed by a slight increase in CPO strength. CPO at the largest strain ($M = 0.11$) is marginally lower than the strength of the CPO of the starting material ($M = 0.13$). Samples deformed in the oblique configuration also exhibit an initial drop in CPO strength, which subsequently increases with strain to a maximum value of $M = 0.16$. Samples deformed in the parallel geometry show a weaker texture strength ($M = 0.06$), which is largely unchanged with increasing strain.

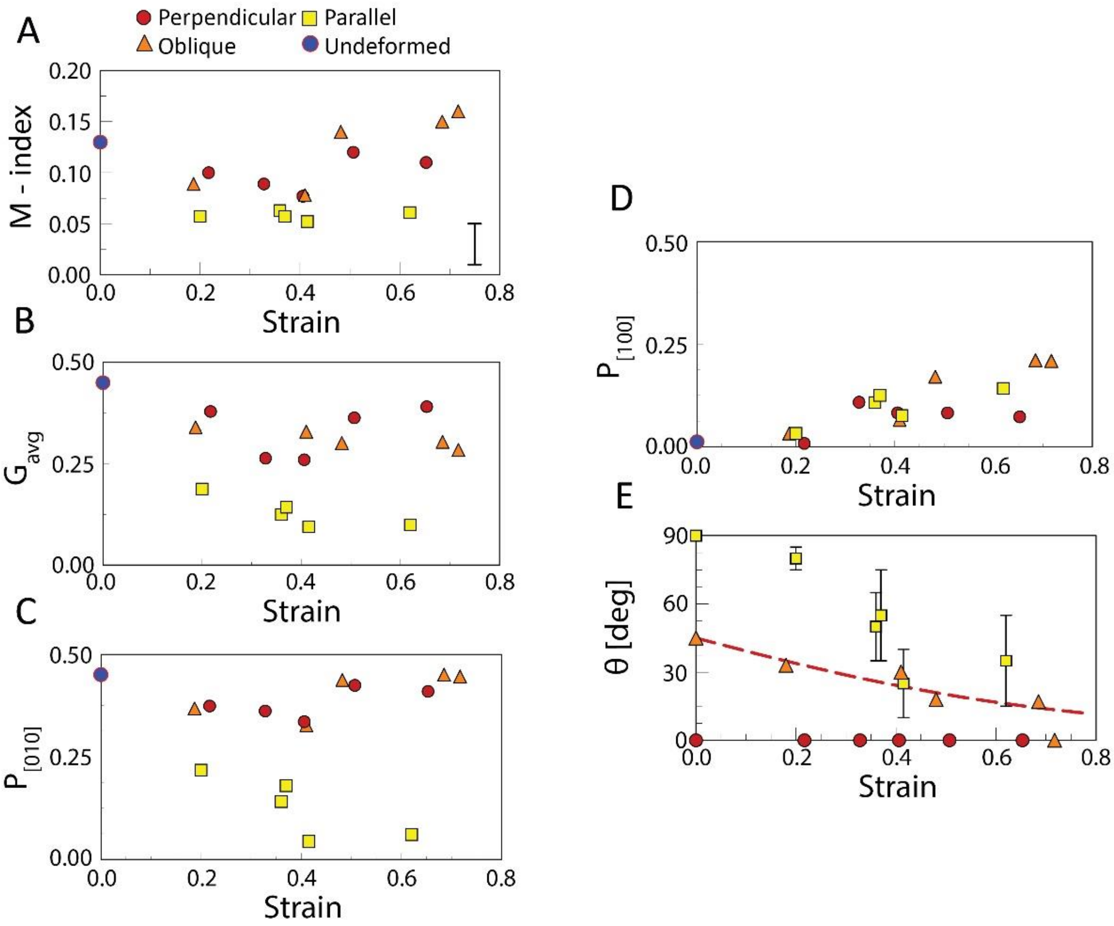

Figure 2.4 – Three elements of sample texture: strength (A), symmetry (B-D), and orientation (E), as a function of strain. Samples deformed in perpendicular, oblique, and parallel configurations are shown by red circles, orange triangles and yellow squares, respectively. The blue circle shows the texture of undeformed Åheim dunite. Data shown are based on one point-per grain analyses, to highlight the texture evolution of the recrystallized grains. (A) Texture strength quantified using the M-index technique (Skemer et al., 2005). A representative error bar (±0.02) is shown in the lower right. The strength increases in the samples deformed with perpendicular and oblique geometries. The strength of samples deformed in parallel geometry decreases with strain. (B-D) Texture symmetry described by an average of $G_{[100]}$ and $G_{[001]}$ (B), $P_{[010]}$,(C), and $P_{[100]}$ (D) (G – girdle, P – point, see text for details). (E) Texture rotation is described by the angle Ө, which is the angle between [010] and the shortening axis. The broken red line shows the orientation of a passively rotating 45° plane in pure shear (Ramsay, 1967, pg 67).

Figures 2.4B and 2.4C show the average value of the girdles in the [100] and [001] pole figures using:

$$G_{avg} = 0.5(G_{[100]} + G_{[001]}) \qquad (2.4)$$

and the evolution of $P_{[010]}$, respectively. For the samples deformed in perpendicular configurations, G_{avg} initially decreases from 0.38 to 0.26 and subsequently increases from 0.26 to 0.39 at higher strains. $P_{[010]}$ increases slightly with strain from 0.35 to 0.43, reflecting the strengthening CPO. For the samples deformed in oblique configurations, G_{avg} decreases slightly with strain from 0.34 to 0.28 while $P_{[010]}$ increases slightly from 0.39 to 0.46. For the samples deformed in parallel configurations, G_{avg} has low initial value of 0.19 that decreases with strain to 0.10. $P_{[010]}$ has low initial value of 0.22, that decreases with strain to 0.05. Figure 2.4D shows the evolution of $P_{[100]}$ with strain. Strength of $P_{[100]}$ increases from 0.01 in the undeformed sample to 0.2 in the most deformed sample.

Figure 2.4E illustrates the rotation of the [010] axes with progressive strain. ϴ is defined as the angle between the densest concentration of [010] axes and the shortening direction (Fig. 2.4E). For samples deformed in perpendicular configuration, the newly imposed deformation plane is parallel to the pre-existing foliation plane, thus, no rotation is expected or observed. For samples deformed in the oblique configuration, the orientation of the [010] point maximum rotates progressively towards the shortening axis. The rotation initially follows the trajectory of an object passively rotated during coaxial deformation (broken line, Fig. 2.4E) (Ramsay, 1967). At the highest strain the [010] axes are nearly parallel to the shortening direction, and the sample diverges from the passive rotation trajectory. For samples deformed in parallel configuration, the [010] point maximum disperses with strain, exhibiting a very weak point maximum. Consequently, the estimated uncertainty in ϴ is large.

2.4 Discussion

The CPO of olivine affects many geophysical processes and represents an important cornerstone of our interpretation of deformation within Earth's mantle. Due to olivine's intrinsic rheological anisotropy, there is a strong relationship between the strength of the deformation induced CPO and the instantaneous shear strength of an olivine aggregate (Hansen et al., 2012a; Tommasi et al., 2009). Therefore, it is clear that steady-state CPO is required to attain steady-state rheology. Similarly, interpreting seismic anisotropy in terms of mantle flow requires knowledge of whether or not CPO been aligned with the instantaneous deformation field. Hence, it is important to assess the rate at which olivine CPO evolves, and the conditions under which olivine CPO achieves steady state.

2.4.1 CPO development in samples with initially weak textures

Previous experimental studies have explored the initial formation and evolution of CPO in both pure shear (Nicolas et al., 1973) and simple shear (Bystricky et al., 2000; Hansen et al., 2014; Zhang and Karato, 1995) on materials with initially weak CPO. Nicolas et al. (1973) provide the first systematic data on CPO development in olivine, through a series of triaxial deformation experiments that generated an axi-symmetric CPO. Zhang and Karato (1995) followed with the first experiments in a simple shear geometry, which generated the expected orthorhombic CPOs often observed in nature (e.g. Ben Ismaïl and Mainprice, 1998; Nicolas and Christensen, 1987). Subsequent experiments in torsion (Bystricky et al., 2000) provided additional data at shear strains of up to $\gamma = 5$. Zhang and Karato (1995) show that olivine [100] axes rotate towards the shear direction at relatively small strains ($\gamma = 1$) and are generally assumed to be stable at that point (Bystricky et al., 2000). These observations support the paradigm, widely used in interpreting seismic anisotropy, that olivine CPO evolves relatively quickly, and reaches a stable configuration at low strains (e.g. Skemer et al., 2012). However, in each of these sets of experiments, fabric strength continues to increase with progressive strain, indicating that true steady state was not achieved. Hansen et al. (2014), building on these experiments, performed torsion tests on olivine up to strains of $\gamma = 20$. These authors interpret their results to show that other elements of texture, including the strength and symmetry of the CPO, continue to evolve up to shear strains of $\gamma = 10$, and suggest that larger strains may be required to reach steady state.

2.4.2 CPO development in samples with initially strong textures

Most experimental studies on the evolution of olivine CPO have focused on synthetic starting materials with initially weak or random CPO. However, laboratory experiments (Skemer et al., 2011; Wendt et al., 1998) and geologic studies of shear zone evolution (Michibayashi and Mainprice, 2004; Skemer et al., 2010; Warren et al., 2008; Webber et al., 2010) have demonstrated that pre-existing texture may alter the rate at which CPO evolves.

In this study, olivine with a pre-existing CPO is deformed in an axially symmetric geometry, under conditions that favor the activity of the [100](010) slip system. Three different sample orientations are used to simulate three different deformation histories. At these deformation conditions the CPO that is expected to form is axi-symmetric, with a [010] point maximum parallel to the shortening axis (towards the Z axis) and [100] and [001] girdles in the radial plane (i.e., X-Y plane)(Karato et al., 2008; Nicolas et al., 1973). To determine whether steady-state CPO is achieved in our experiments we analyze a number of metrics that quantify the strength, symmetry, and orientation of texture. Our assertion is that for texture to reach steady state, three things are required: (1) The strength of the CPO must approach a steady state value. (2) The symmetry elements (point, girdle, and random) for all pole figures must approach steady values. (3) The alignment of the CPO with respect to the deformation geometry must cease to rotate with progressive strain. Microstructural observation and texture quantification reveal that the microstructure did not reach a steady state for any of the three samples configurations. Pole figures (Fig. 2.3) illustrate the differences in CPO development between samples deformed in the three different geometries. Samples deformed in the perpendicular geometry show a relatively well-developed texture, which we interpret to be due to the similarity between the initial texture and the predicted steady-state texture. Samples deformed in the oblique geometry appear to show a texture that is similar to the predicted steady state texture, but also exhibit a pronounced orthorhombic symmetry at high strain. Samples deformed in parallel geometry do not exhibit a texture that resembles the predicted CPO, even at the highest strains. Considered together, all three deformation geometries show features of transient CPO evolution, but do not converge towards a steady-state texture.

2.4.3 Development of an apparent B-type fabric

The highest strain samples from the oblique and parallel configurations exhibit a quasi-orthorhombic CPO with point maxima, rather than the predicted girdles, in the radial plane. This is particularly evident in experiments with oblique configurations, in which the initial foliation is 45 degrees from the axis of compression. In these pole figures (Fig. 2.3B) there is a clear [100] point maximum parallel to Y (the direction in the radial plane that is parallel to the initial strike of the foliation), and a complementary [001] point maximum parallel to X (the direction in the radial plane perpendicular to the initial strike of the foliation). $P_{[100]}$ is also observed to increase with progressive strain (Fig. 2.4D). The symmetry of this CPO is unexpected. Theoretical treatments of CPO evolution predict that deformation with axisymmetric kinematics should generate a texture that is also axially symmetric (Ribe and Yu, 1991; Wenk et al., 1991). Triaxial deformation experiments confirm this prediction (e.g. Nicolas et al., 1973). Lower symmetry is expected when there is a significant component of simple shear (Wenk and Tomé, 1999), however there is no shape change that would indicate this occurred in our experiments.

The orientation of [100] axes could lead to the interpretation that the CPO generated in these experiments is "B-type" (Jung and Karato, 2001), which has been widely cited as a plausible explanation for trench-parallel shear wave splitting (e.g. Long and Silver, 2009). Strictly, the B-type CPO is generated by the predominant activity of the [001](010) slip system. However at these deformation conditions, the [100](010) and associated A-type CPO are favored.

We interpret the CPO of samples deformed in oblique and parallel geometries as an ‘apparent B-type’ fabric that is a consequence of the pre-existing texture. In oblique and parallel configurations, some fraction of the grains in the starting material have [100] axes that are located initially in the radial plane. By definition, these [100] axes are parallel to the strike of the initial foliation, and therefore parallel to the Y-axis of our deformation geometry. This subset of grains is already at or near its steady state orientation and although their Schmidt factor is low these grains do not require significant rotational deformation to reach the radial plane. Other grains, whose [100] axes are initially distributed elsewhere in the girdle and therefore not located in the radial plane, require larger strains to adopt the predicted steady-state CPO. Hence, we conclude that this apparent B-type CPO is not a steady-state texture, but instead represents a transient stage in the evolution towards axially symmetric texture. Due to the limited maximum strain of a triaxial deformation experiment, it is unclear how much additional strain would be required to fully obscure the pre-existing texture.

2.4.4 Seismic anisotropy

The results of this study emphasize the important role of deformation history on texture evolution, and highlight the impact of transient CPO on the interpretation of seismic anisotropy (Skemer et al., 2012). Figure 2.5 shows the predicted anisotropic signature of the undeformed sample and samples with the highest strains from experiments in the perpendicular, oblique and parallel configurations. EBSD data used in this calculation are weighted by grain area, so a few larger relict grains can have a proportionately large influence on the results. It is clear that the samples deformed in each configuration exhibit distinct seismic properties, both in terms of the magnitude and orientation of the anisotropy. As with the CPO, seismic anisotropy did not achieve steady-state in our experiments, but rather continued to evolve throughout the full range of strains achieved here (Fig. 2.6). The long transient stage of texture evolution could readily generate shear wave splitting signatures that do not represent the present day mantle flow direction. Similarly, the transient reorganization of CPO could produce an apparently weak CPO that would manifest itself as weak anisotropy.

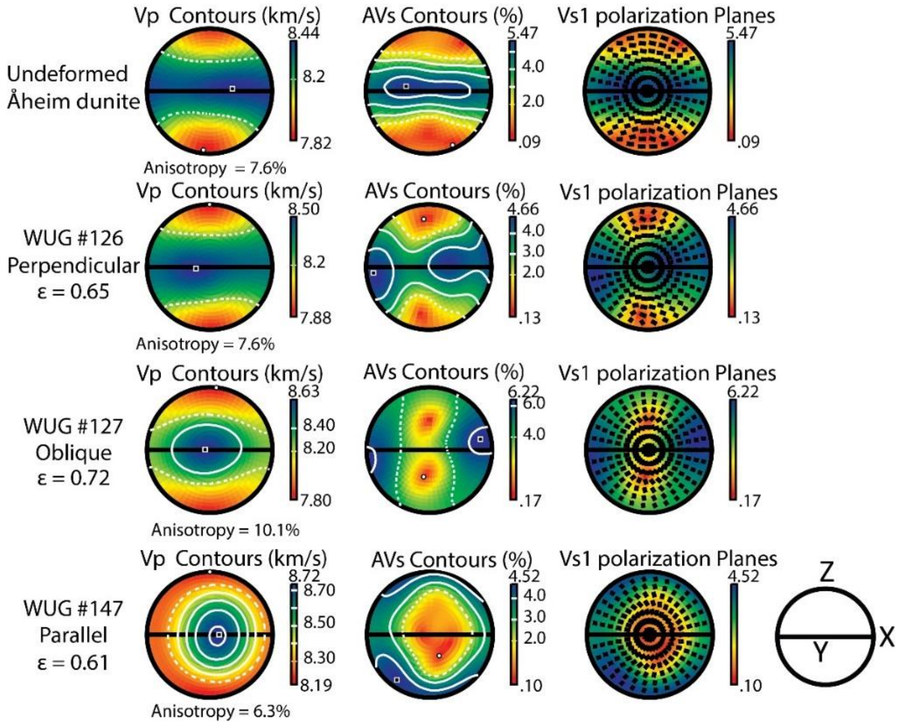

Figure 2.5 – Upper hemisphere pole figures (same orientation as Figure 2.3) showing seismic anisotropy calculated by weighted area for the undeformed sample, and highly deformed samples with perpendicular, oblique and parallel configurations using elastic constants from (Abramson et al., 1997). The left column shows the P-wave velocity (Vp) in units of [km/s]. The middle column shows the percent difference between the fast and slow S-wave velocities (AVs = 200 (V_{max} –V_{min})/ (V_{max} +V_{min})). The direction of maximum/minimum velocities is denoted by black box and white circle respectively. The right column shows the orientation of the fastest S-wave (Vs1) with respect to deformation plane. Colors in the right column are contours of AVs, identical to the middle column of pole figures. The undeformed and perpendicular configuration samples exhibit anisotropy similar to an A-type fabric, while the oblique and parallel configuration samples are more similar to a B-type fabric (Mainprice, 2007).

Mantle flow around subduction-zones, as an example, is complicated by large temperature and compositional gradients, horizontal and sub-vertical flow in the direction of convergence, and trench parallel flow, particularly near slab edges (Blackman and Kendall, 2002; Faccenda and Capitanio, 2012; Jadamec and Billen, 2012; McKenzie, 1979). The complexity of this environment has presented a challenge to the interpretation of seismic anisotropy (Long and Becker, 2010). Many of the features of plate boundary seismic anisotropy have been attributed to the effects of pressure (Jung et al., 2009), water content (Katayama and Karato, 2006; Long and Becker, 2010), asthenospheric entrainment by the subducted slab (Song and Kawakatsu, 2012), or 3-D flow patterns (Faccenda and Capitanio, 2012; Long and Silver, 2008). Based on our experimental results, other observations from naturally deformed rocks (Michibayashi and Mainprice, 2004; Skemer et al., 2012; Warren et al., 2008; Webber et al., 2010), and data from numerical simulations (Castelnau et al., 2009; Di Leo et al., 2014) it is increasingly evident that deformation history must also be a factor in the interpretation of seismic anisotropy.

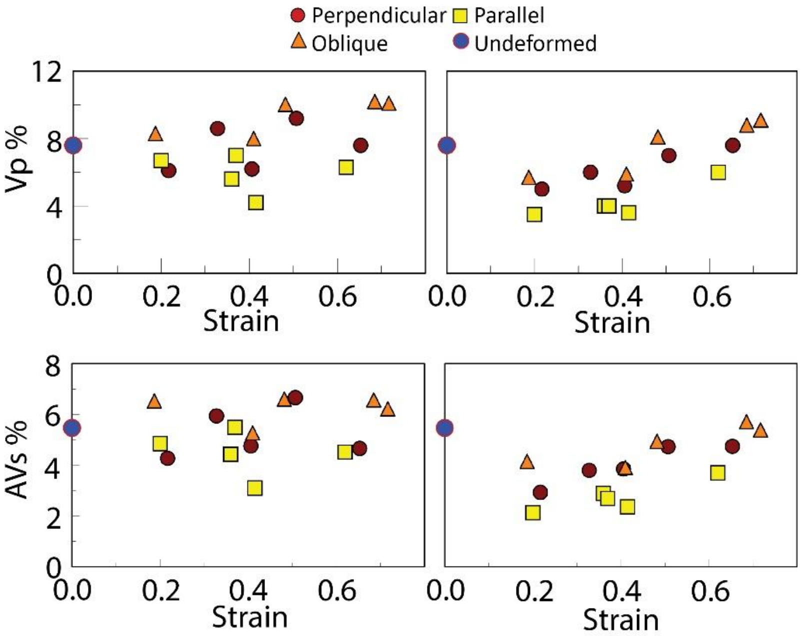

Figure 2.6 – Anisotropy of seismic wave velocities Vp and Vs in %, calculated by weighted area for samples in three different configurations. Samples deformed in perpendicular, oblique, and parallel geometries are shown by red circles, orange triangles and yellow squares, respectively. Blue circles show the anisotropic properties of the starting material. (A) and (C) show the seismic wave velocities Vp and AVs, respectively, calculated using all the data, which includes a small number of relict grains. (B) and (D) show the calculated seismic velocities using grains with diameter smaller than 50 µm representing only the recrystallized grains (neoblasts). Within the set of neoblasts, anisotropy increases with strain for all three samples configurations. Neither Vp nor AVs anisotropy reaches a plateau indicating that steady state was not achieved.

2.5 Conclusions

Experiments performed on natural Åheim dunite with pre-existing texture were deformed to strains up to 0.7. Using three different pre-existing texture orientations we show that deformation history of olivine aggregates greatly influence the way texture evolves with strain. Based on quantification of pole figures in terms of texture strength, symmetry, and alignment, we assert that the texture in all three experimental configurations did not reach a steady state. Rapid changes in mantle flow direction may be associated with long transient stages in which texture evolves slowly towards a steady state. It is concluded that any interpretation of seismic anisotropy in terms of mantle flow must consider the integrated deformation history of the region of interest.

Chapter 3: Modeling olivine CPO evolution with complex deformation histories: Implications for the interpretation of seismic anisotropy in the mantle

An edited version of this chapter was published by ‘*Geochemistry, Geophysics, Geosystems’* of the American Geophysical Union.

Boneh, Y., L. F. G. Morales, E. Kaminski, and P. Skemer (2015), Modeling olivine CPO evolution with complex deformation histories: Implications for the interpretation of seismic anisotropy in the mantle, Geochem. Geophys. Geosyst., 16, 3436–3455, doi:10.1002/2015GC005964.

Abstract

Relating seismic anisotropy to mantle flow requires detailed understanding of the development and evolution of olivine crystallographic preferred orientation (CPO). Recent experimental and field studies have shown that olivine CPO evolution depends strongly on the integrated deformation history, which may lead to differences in how the corresponding seismic anisotropy should be interpreted. In this study, two widely-used numerical models for CPO evolution – D-Rex and VPSC – are evaluated to further examine the effect of deformation history on olivine texture and seismic anisotropy. Building on previous experimental work, models are initiated with several different CPOs to simulate unique deformation histories. Significantly, models initiated with a pre-existing CPO evolve differently than the CPOs generated without pre-existing texture. Moreover, the CPO in each model evolves differently as a function of strain. Numerical simulations are compared to laboratory experiments by Boneh and Skemer (2014). In general, the D-Rex and VPSC models are able to reproduce the experimentally observed CPOs, although the models significantly over-estimate the strength of

the CPO and in some instances produce different CPO from what is observed experimentally. Based on comparison with experiments, recommended parameters for D-Rex are: $M^* = 10$, $\lambda^* = 5$, and $\chi = 0.3$, and for VPSC: $\alpha = 10 - 100$. Numerical modeling confirms that CPO evolution in olivine is highly sensitive to the details of the initial CPO, even at strains greater than 2. These observations imply that there is a long transient interval of CPO realignment which must be considered carefully in the modeling or interpretation of seismic anisotropy in complex tectonic settings.

3.1 Introduction

Patterns of flow in Earth's interior provide insight into the convective forces that drive plate motions. However, flow patterns are difficult to determine uniquely as Earth's interior is largely invisible to direct observation. Geophysical data, such as the velocity and anisotropy of seismic waves, represents our primary window into the internal structure of the planet. In the upper mantle, anisotropy of seismic wave velocities is caused mainly by the preferential alignment of seismically anisotropic grains in polycrystalline rock – often called crystallographic preferred orientation (CPO). CPO develops through the activity of specific deformation mechanisms, which cause individual crystal lattices to rotate into favored orientations with respect to the kinematics of flow (Ave Lallemant, 1975; Nicolas and Christensen, 1987).

Models of CPO evolution provide tools to both predict and interpret seismic anisotropy. This can be implemented in a forward manner by coupling geodynamic flow simulations or physical models to a numerical or conceptual model for CPO evolution, leading to predictions for seismic anisotropy in a given setting (Blackman et al., 1996; Chastel et al., 1993; Conrad et al., 2007; Druken et al., 2011; Druken et al., 2013; Faccenda and Capitanio, 2012; Faccenda and

Capitanio, 2013; Paczkowski et al., 2014; Tommasi, 1998). CPO modeling can also be applied in an inverse way to relate seismological observations to the kinematics of mantle flow (Alpert et al., 2013; Becker et al., 2006b).

To interpret seismic anisotropy in terms of mantle flow it is typically assumed that CPO is near steady state, which means that the current CPO reflects only the macroscopic deformation kinematics of the region sampled by the seismic waves. This assumption implies that the rate of CPO evolution along a particular flowline is significantly smaller than the rate of deformation evolution, as quantified by the Grain-Orientation-Lag (GOL) parameter introduced by Kaminski and Ribe (2002). Boneh and Skemer (2014) proposed an additional set of empirical criteria for determining whether steady-state CPO has been achieved. Texture can be considered in steady-state if the strength, symmetry, and orientation of the crystallographic orientation patterns do not change with progressive strain. Using similar criteria, recent experiments on polycrystalline olivine show that very large strains are necessary (up to a shear strain of 10) in order to achieve textural steady-state (Hansen et al., 2014). Experiments and field observations have also demonstrated that pre-existing textures introduced by complex deformation histories significantly modify the rate and patterns of subsequent CPO evolution (Boneh and Skemer, 2014; Skemer et al., 2010; Skemer et al., 2011; Warren et al., 2008; Webber et al., 2010). These studies demonstrate that there is considerable variability in the rate of texture development, especially in comparison to experiments that do not take into account pre-existing texture (Skemer et al., 2012). Furthermore, experiments by Hansen et al. (2012a) have demonstrated that the shear strength of polycrystalline olivine is a function of texture strength, confirming that microstructure and rheology are coupled up to very large strains (Knoll et al., 2009).

Collectively, these data corroborate inferences from natural shear zones, which are thought to experience long transient evolution of both microstructure and rheology.

The protracted evolution of olivine CPO suggests that deformation history should have a significant impact on the interpretation of seismic anisotropy (Kaminski and Ribe, 2002; Skemer et al., 2012). The viability of the forward modeling approach is contingent on the capability of numerical models to simulate CPO evolution with complex deformation history. A wide range of theoretical models using different physical backgrounds and hypotheses have been proposed to simulate texture evolution, including the viscoplastic self-consistent approach (Lebensohn and Tomé, 1993; Tommasi et al., 2000; Wenk et al., 1991), second order viscoplastic self-consistent approach (Castañeda, 2002; Raterron et al., 2014), the kinematic model D-Rex (Kaminski and Ribe, 2001; Kaminski et al., 2004), and equilibrium-based models (Chastel et al., 1993). In many cases, these models have been parameterized through comparison with laboratory experiments, such as the results of Nicolas et al. (1973) and Zhang and Karato (1995), which describe the formation and evolution of olivine deformed in uniaxial compression and simple shear, respectively. However, a limitation of these comparisons is that the starting materials of most of laboratory experiments and corresponding simulations have a “random” texture, in which there is no significant quantifiable alignment of grains. Indeed, it is challenging to model CPO evolution with complex deformation histories and kinematics (Blackman and Kendall, 2002; Castelnau et al., 2009), which contributes to the difficulty of interpreting seismic anisotropy near plate boundaries (e.g., Becker et al., 2014; Blackman, 2007; Castelnau et al., 2009).

In this study we compare numerical models of CPO evolution with recent experimental results that demonstrate the effect of deformation history on CPO (Boneh and Skemer, 2014). We employ two widely-used methods for texture development modelling: the viscoplastic self-consistent (VPSC) approach as described in Tommasi et al. (2000), which is based on the reorientation of crystals through intracrystalline slip and grain interactions, and the D-Rex approach (Kaminski and Ribe, 2001), which considers intracrystalline slip and dynamic recrystallization but does not model mechanical interactions between grains. The VPSC approach has been used to simulate olivine texture in mantle flow, shear zones and lithospheric plate interactions (Bonnin et al., 2012; Di Leo et al., 2014; Li et al., 2014; Tommasi et al., 1999; Tommasi et al., 2009). D-Rex is often used to simulate larger strains, when dynamic recrystallization must be taken into account. D-Rex is also preferred in larger-scale geodynamic models, due to its relative ease of computation (Becker et al., 2006a; Conder and Wiens, 2007; Faccenda and Capitanio, 2012; Hedjazian and Kaminski, 2014; Kaminski and Ribe, 2002). In contrast to the standard approach of comparing CPO evolution in experiments and models with a random set of initial grain orientations, we have initiated our models using the same natural CPO and the same deformation configurations previously explored experimentally by Boneh and Skemer (2014). This approach allows for the direct comparison between experiments and numerical modeling and provides new insights about the effect of pre-existing crystallographic orientation on the texture development.

3.2 Methods

Both the VPSC and D-Rex models are described extensively elsewhere (Kaminski and Ribe, 2001; Kaminski et al., 2004; Lebensohn and Tomé, 1993; Tommasi et al., 2000). Here we will highlight only the main features and differences between these models. For both models, the rotation of grains is implemented through the glide of dislocations along specific crystal slip systems. Models consider the experimentally determined olivine slip systems and their critical resolved shear stress (CRSS); deformation follows the viscoplastic law:

$$\dot{\gamma}_s = \dot{\gamma}_0(\tau_r^s \, / \, \tau_0^s)^n \qquad (3.1)$$

$\dot{\gamma}_s$ is the slip system strain-rate, $\dot{\gamma}_0$ is the reference strain-rate, τ_r^s is the resolved shear stress (a function of the Schmidt factor – the orientation of the slip system with respect to the imposed stress), τ_0^s is the critical resolved stress, and n is the stress exponent.

3.2.1 D-Rex model

Modeling texture through the kinematic approach of D-Rex assumes crystal reorientation through the local velocity gradient:

$$d_{ij} = G_{ij}\nu - \varepsilon_{ijk}w_k \qquad (3.2)$$

Where G_{ij} is the Schmidt factor, which relates the crystal and imposed stress orientations, ν is the slip rate on the softest slip system for a given grain, ε_{ijk} is the macroscopic (aggregate) strain rate, and w is the rotation rate. In order to satisfy the strain compatibility a minimization technique is used to minimize the difference between the single crystal and aggregate strain (Ribe and Yu, 1991). The residual strain, ~10% (Kaminski and Ribe, 2001), is assumed to be accounted for by processes that do not impose crystal rotation, such as diffusive mass transfer and/or grain boundary migration. (Ribe and Yu, 1991).

D-Rex simulates dynamic recrystallization through two dimensionless parameters that account for grain boundary migration and grain nucleation (*M** and λ* respectively). D-Rex also simulates the effects of “grain boundary sliding” through the dimensionless parameter χ (Kaminski and Ribe, 2001). Grain growth is incorporated using a parameter for grain-boundary migration:

$$M^* = \frac{A\mu bM}{\upsilon} \qquad (3.3)$$

where A is dimensionless constant, μ is the shear modulus, b is Burger vector, *M* is a dimensionless grain-boundary mobility, and υ is the dislocation velocity.

Grain size reduction through dynamic recrystallization is incorporated into D-Rex using a parameter for the nucleation of strain-free grains

$$\lambda^* = ln(\alpha_V)\left(\frac{\rho_0}{\rho}\right) \qquad (3.4)$$

Where λ* is dimensionless nucleation parameter, α_V is the non-recrystallized volume fraction of the crystal, and ρ_0 and ρ are a reference dislocation density and the crystal's dislocation density, respectively, the ratio of which acts as the driving force for nucleation. The two parameters, *M** and λ*, account for competing processes. *M** is responsible for the migration of grain boundaries, which cause highly strained crystals ('soft' grains) to be invaded by weakly strained crystals ('hard' grains) increasing the number of grains in hard orientations. λ* accounts for the nucleation of new grains, which cause the highly strained soft grains to nucleate new grains with zero strain in the same orientation. Due to their low stain energy, these grains then grow by grain boundary migration, increasing the volume fraction of grains in soft orientations. One effect of grain size reduction by nucleation of new small grains is that these grains may accommodate strain by mechanisms that do not invoke crystallographic rotation (diffusion creep and/or grain boundary sliding). This effect is represented by parameter χ, which disables the rotation of grains below a specific grain volume fraction threshold (Kaminski et al., 2004).

3.2.2 VPSC model

In the VPSC approach, each grain’s strain and stress is considered in terms of the bulk aggregate strain and stress by using the “one site” grain interaction simplification which simulates interaction of each grain with a surrounding homogeneous equivalent medium (HEM) (Eshelby, 1957):

$$\dot{\epsilon}_{ij} - \dot{E}_{ij} = -\alpha M_{ijkl}(s_{kl} - \Sigma_{kl}) \quad (3.5)$$

Where $\dot{\epsilon}_{ij}$ is the grain strain-rate, $\dot{E}_{ij}$ is the average strain-rate of the aggregate, α is parameter that describes grain interaction with its surroundings, M_{ijkl} is the interaction tensor that includes grain rheology and shape, s_{kl} is the grain deviatoric stress, and Σ_{kl} is the average stress of the aggregate. Through this approach, microscopic stress and strain rates may vary significantly with respect to the averaged (macroscopic) values. The grain interaction parameter, α, represents the grain response and ranges between the upper bound, in which α is equal to zero and homogeneous strain is assumed (Taylor, 1938), and the lower bound, in which α approaches infinity, and homogeneous stress is assumed (Sachs, 1928). Limitations of the VPSC compared to full-field models (models that include aggregate microstructure) have been shown, in particular, the effect of secondary slip systems (Castelnau et al., 2008; Castelnau et al., 2010; Detrez et al., 2015) and the overestimation of texture strength (Castelnau et al., 2006).

3.2.3 Differences between VPSC and D-Rex

The fundamental difference between VPSC and D-Rex is that the former is physics-based (mean-field) model while the latter is an ad-hoc (far-field) model. In VPSC interaction between grains are considered via the HEM assumption while stress compatibility is maintained, which allows a meaningful representation of the relative activity of different slip system (Tommasi et al., 2000). The formulation of the VPSC approach in the present study does not include processes like dynamic recrystallization or relaxation processes like dislocation climb and grain boundary sliding, although this has been implemented recently by Signorelli and Tommasi (2015). In contrast, D-Rex includes ad hoc parameters that are intended to simulate microphysical processes in addition to deformation: dynamic recrystallization and grain boundary sliding. In addition, the calculation of intracrystalline deformation in D-Rex is analytical. Hence the code requires fewer computations, which allows it to be easily coupled to larger geodynamic models.

3.2.4 Model starting conditions

Both VPSC and D-Rex models are initiated using input textures comprised of 1000 grain orientations. In some tests, simulations are initiated using random crystal orientations. In most of the present study however, we use the CPO of a natural dunite from Åheim, Norway as the starting texture. This is the CPO of the same rock specimen that we used as the starting material for the experiments of Boneh and Skemer (2014) and has been widely used in other rock mechanics studies (Chopra and Paterson, 1981; Chopra and Paterson, 1984; Jackson et al., 1992; Keefner et al., 2011; Van der Wal et al., 1993; Wendt et al., 1998). The texture of the Åheim dunite was measured by Electron Backscatter Diffraction (EBSD), (see Boneh and Skemer, 2014, for details of microstructural characterization). The Åheim dunite is foliated and exhibits a strong axial girdle (AG) texture, characterized by the alignment of [010] axes normal to the foliation of this rock, while [100] and [001] are distributed along single continuous girdles parallel to the foliation (Fig. 3.1A). Such a pattern reflects a history of nearly uniaxial deformation (Mainprice, 2015; Nicolas et al., 1973; Wenk et al., 1991). In both the Boneh and Skemer (2014) experiments and in the models described in this study, the Åheim dunite texture

(Fig. 3.1A) was deformed in three different configurations in which the sample and/or CPO is rotated to angles of 0, 45, and 90 degrees with respect to the shortening axis (Fig. 3.1B).

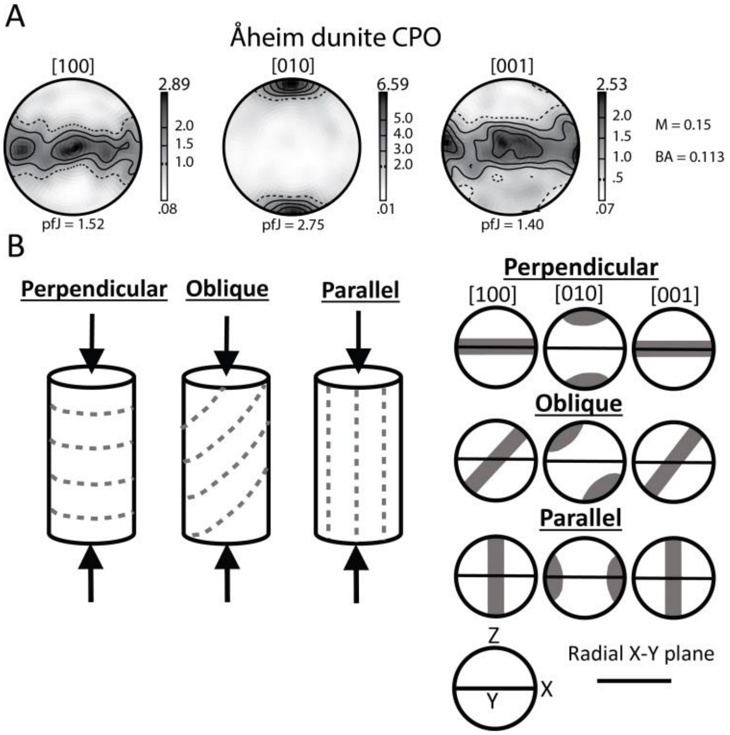

Figure 3.1 – (A) Pole figures showing the olivine crystallographic preferred orientation (CPO) of Åheim dunite. The Åheim dunite exhibits a girdle of orientations in [100] and [001] parallel to the foliation plane. The foliation is also marked as dotted lines in (B). Contour intervals are linear and scaled to multiples of uniform distribution, m.u.d. (scale bars on left side of each pole figure). Texture strength (M-index) and texture symmetry (BA-index) are listed to the right of the pole figures. (B) Three configurations of the Åheim dunite samples in which the axis of shortening is perpendicular, oblique, or parallel to the dunite initial foliation. On the right are schematic illustrations of the initial texture for each of the three configurations. Pole figures are in a X-Y-Z reference frame in which the shortening axis is parallel to the Z direction and the X – Y plane is in the radial plane, perpendicular to the shortening axis.

The stress exponent used in the models (n = 3.5, Table 3.1) has been well established by rock deformation experiments for olivine single crystals in various orientations (Bai et al., 1991; Durham and Goetze, 1977), as well as for polycrystals (Karato et al., 1986). To maintain consistency and to facilitate comparison with previous studies, the relative strength of olivine’s primary slip-systems for VPSC and D-Rex (Table 3.1) are taken from Tommasi et al. (2000) and Kaminski and Ribe (2001), respectively. These critical resolved shear stresses are chosen to represent the most ubiquitous olivine texture (A-type, of Jung and Karato, 2001), which is dominated by slip on the [100](010) slip system (Ben Ismaïl and Mainprice, 1998). The [100](010) slip system is also inferred to be the dominant slip system in the Boneh and Skemer (2014) experiments. The deformation geometry is uniaxial compression with the corresponding strain tensor with $\varepsilon_{11} = \varepsilon_{33} = 0.5$, $\varepsilon_{22} = -1$ and $\varepsilon_{i \neq j} = 0$. The parameters used are $\alpha = 100$ for VPSC, and $M^* = 10$, $\lambda^* = 5$, $\chi = 0.3$, for D-Rex. Rationale for this choice of parameters is discussed in section 3.4.2.

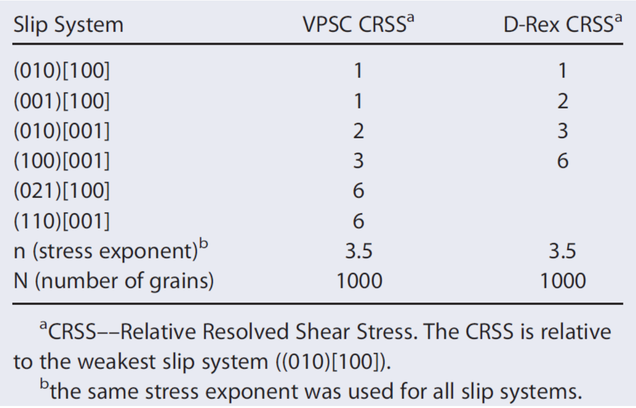

Slip System	VPSC CRSS[a]	D-Rex CRSS[a]
(010)[100]	1	1
(001)[100]	1	2
(010)[001]	2	3
(100)[001]	3	6
(021)[100]	6	
(110)[001]	6	
n (stress exponent)[b]	3.5	3.5
N (number of grains)	1000	1000

[a] CRSS––Relative Resolved Shear Stress. The CRSS is relative to the weakest slip system ((010)[100]).

[b] the same stress exponent was used for all slip systems.

Table 3.1 - Models input parameters

3.2.5 Quantifying texture and anisotropy

Texture is characterized by its strength, its symmetry, and its orientation with respect to the reference frame of deformation. Texture symmetry and orientation control the orientation of anisotropy detected seismologically. Texture strength influences mainly the magnitude of the anisotropy up to a limit, after which the magnitude reaches saturation (Hedjazian and Kaminski, 2014).

In order to evaluate texture evolution with increasing strain we use several quantitative parameters. Texture strength is quantified using the M-index method, ranging from M = 0, for a perfect random texture, to M = 1, for perfect crystallographic alignment (e.g., a single grain) (Skemer et al., 2005), and the pole figure strength (pfJ) parameter (e.g., Mainprice et al., 2014) for individual pole figures, which ranges from 1 for a perfect random texture to infinity for perfect alignment. As [100], [010] and [001] are all two-fold rotation axes, the results from pfJ can be directly compared.

Texture symmetry is quantified using the parameters Point (P), Girdle (G), and Random (R), which describe whether the CPO is best represented by a point maximum (Point), an equal distribution of points along a plane (Girdle), or a uniformly distributed texture with no preferred orientation (Random) (Vollmer, 1990). These three symmetry parameters, calculated from eigenvalues of the orientation tensor (Mainprice et al., 2014), always sum to 1, and therefore can be plotted in a ternary diagram (e.g., Falus et al., 2011; Higgie and Tommasi, 2012; Morales and Tommasi, 2011; Tommasi et al., 2008; Vauchez et al., 2005). P, G, and R components for specific pole figures are denoted using subscript notation: (e.g. the girdle component of the [100] pole figure is denoted $G_{[100]}$). Another way to quantify a specific coaxial texture is the BA-index, in which a specific point and girdle components are compared to the point and girdle sum so that the dependence of the texture symmetry on the random component is minimized:

$$BA = 0.5\ [2 - \left(\frac{P_{010}}{G_{010}+P_{010}}\right) - \left(\frac{G_{100}}{G_{100}+P_{100}}\right)] \quad (3.6)$$

The BA-index represents symmetry that includes point maxima in the [010] and girdle in the [100] and is scaled to range from BA = 0 to BA = 1 (Mainprice et al., 2014). BA = 0 corresponds to a “perfect” axial girdle (AG) texture while BA = 1 would represent the absence of an AG texture.

Pole figures of CPO and seismic velocities were calculated and plotted using D. Mainprice software (Petrophysical software, Unicef Careware, http://www.gm.univ-montp2.fr/PERSO/mainprice/) (Mainprice, 1990), which assumes Voigt-Reuss-Hill average and elastic constants for olivine from Abramson et al. (1997) in calculating the seismic velocities. We also apply a code by Savransky and Kasdin (2012) to convert grains orientations output from directional cosines (eq. 1 in (Kaminski and Ribe, 2001)) to Euler angles. Pole figures of CPO used for Movie S1 (supplementary materials) were generated using MTEX (Bachmann et al., 2010; Mainprice et al., 2011).

3.3 Results

3.3.1 CPO development with different starting textures

In Figure 3.2, CPOs generated by D-Rex and VPSC models are compared with the experiments of Boneh and Skemer (2014). Results are shown for the three initial configuration: perpendicular (Fig. 3.2A), oblique (Fig. 3.2B), and parallel (Fig. 3.2C). Models are run to the same finite strains achieved experimentally (0.65, 0.68, and 0.62, for the three configurations, respectively).

In the perpendicular configuration (Fig. 3.2A), the experimental texture exhibits a fiber texture (i.e., the coaxial AG-fabric) with girdles in [100] and [001] and a strong point maxima of [010], which is similar to the initial texture symmetry (Fig. 3.1A). Both models show significantly stronger texture than the experiments. For example, the [010] axes in the experimental CPO have a pole figure J-index strength (pfJ) of ~ 2 compared to 5.5 in D-Rex and almost 17 in VPSC.

In the oblique configuration (Fig. 3.2B), the experimental texture shows the [010] point maximum rotated from its original position towards the shortening direction, and weak [100] and [001] point maxima. Both models predict a [010] point maximum rotation similar to the experiment, however, there is difference in the strength of this point maximum ([010] pfJ of 3.27, 4.9 and 11.45 for the experiments, D-Rex, and VPSC, respectively). In the experiments, D-Rex, and VPSC models, there is a pronounced [100] point maximum superimposed on a girdle in the axial plane, giving the texture a pseudo-orthorhombic symmetry.

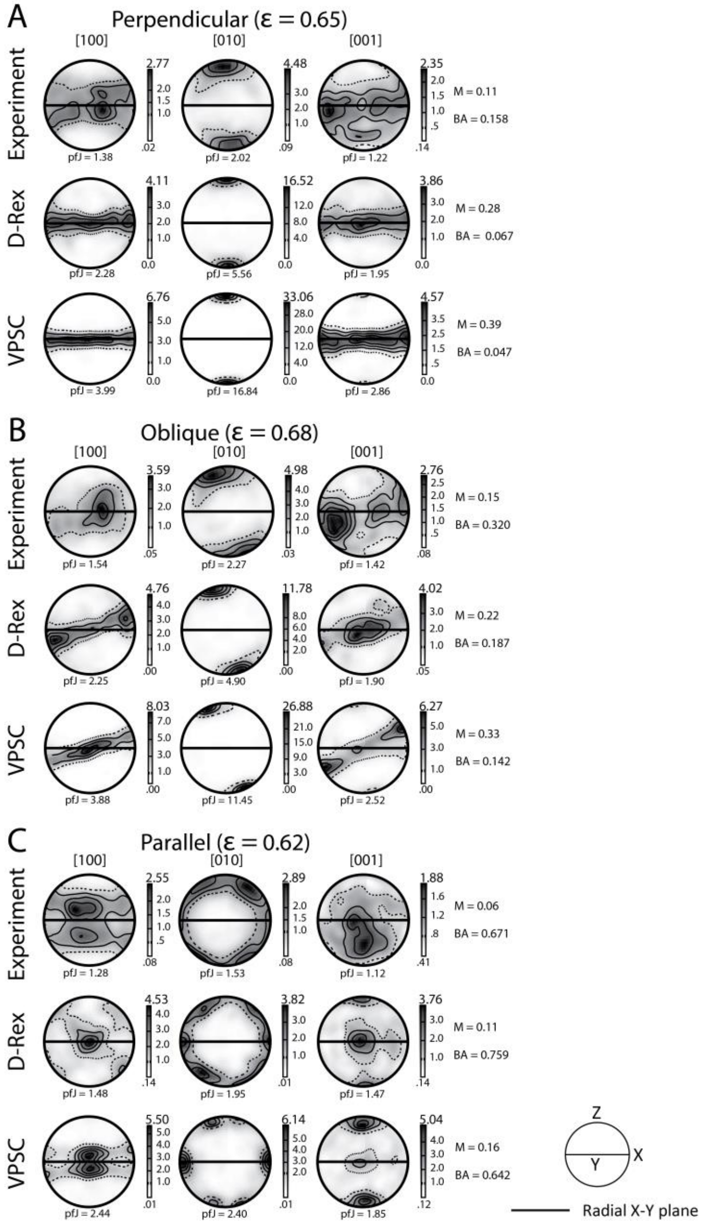

Figure 3.2 – Pole figures showing texture from experiments, VPSC, and D-Rex models for the three starting configurations: perpendicular (A), oblique (B) and parallel (C). Experimental data is taken from high strain experiments of Boneh and Skemer (2014). Parameters used in models: for D-Rex: $M^* = 10$, $\lambda^* = 5$, $\chi = 0.3$, and for VPSC: $\alpha = 100$ (other parameters are shown in Table 3.1). Scale bar to the right of each pole figure show the multiples of uniform distribution (m.u.d.). Pole figures projected in equal area and lower hemisphere. Texture strength of each pole figure (pfJ), the total texture strength (M-index), and the texture symmetry (BA-index) are given.

In the parallel configuration, the experimental texture shows a weak [100] girdle along the radial (X-Y) plane, a [010] girdle along the X-Z plane, and a very weak CPO, i.e., mostly random texture, in the [001] axis (pfJ of 1.12). Both models predict that the [010] axes are distributed along the X-Z plane with three distinct point maxima (one in the X direction and two at a symmetric and oblique angle away from the shortening axis). These three point maxima are more diffuse in D-Rex than in VPSC. For the [100] axis, D-Rex shows a point maximum parallel to Y with two weaker bands of data oriented in an “x” shape at a high angle to the radial plane. VPSC shows a stronger point maximum toward Y with “x” shaped bands forming a girdle subparallel to the radial plane. The “x” shaped features in the model’s CPO agree well with the experimental observations, although there is a difference in the strength and orientation of the bands. For the [001] axis, both VPSC and D-Rex have similar textures with two point maxima at the Y and Z directions. The models predict two point maxima in the [001] axis, parallel to the X and Y axis, but the experiments show a disperse crystals oriented toward Y axis (also among other strains in the parallel configurations, see Fig. 3.3C in Boneh and Skemer, 2014).

3.3.2 Evolution of texture symmetry

D-Rex and VPSC models were run over a range of strains to assess how CPO evolves as a function of strain. Texture evolution for D-Rex (square symbols) and VPSC (circle symbols) models are shown in Fig. 3.3 using a ternary diagram with Point, Girdle and Random texture components as end members. For each of olivine’s three crystallographic axes the symmetry trajectory is shown for the three configurations with pre-existing texture: perpendicular (dark red symbols), oblique (orange symbols), and parallel (yellow symbols), and for an initially random texture (gray symbols). Each point represents a strain-increment between the initial textures, with strain of zero, to strain of 2. The first two points represent texture for small finite strains of 0.01

and 0.05, while the next 20 points are equally spaced with strain intervals of 0.1 (between strain of 0.1 to 2). The starting point (i.e., strain = 0) from which texture evolves for the three configurations with pre-existing texture is shown as a blue star. The starting point for the random case, shown as black star, is defined as having symmetry of R = 1, and P = G = 0.

For models initiated with random texture D-Rex and VPSC produce similar results, which are essentially identical to the results of Kaminski and Ribe (2001) and Tommasi et al, (2000). Texture evolves from random to girdle in [100] and [001], and from random to point in [010], as expected from the experimental results of Nicolas et al., (1973). In the D-Rex model, $G_{[100]}$ increases from 0 to 0.91, $P_{[010]}$ increases from 0 to 0.78, while $G_{[001]}$ increases from 0 to 0.60. In the VPSC model, $G_{[100]}$ increases from 0 to 0.96, $P_{[010]}$ increases from 0 to 0.89, while $G_{[001]}$ increases from 0 to 0.78.

For models initiated with pre-existing texture, each of the three pre-textured configurations shows different symmetry evolution and they also evolve differently with respect to the initially un-textured scenario. For the D-Rex models, $G_{[100]}$ increases from 0.54 to 0.87, 0.64, and 0.71 for perpendicular, oblique and parallel configuration, respectively, $P_{[010]}$ increases from 0.49 to 0.89, 0.87, and 0.59 for perpendicular, oblique and parallel configuration, respectively. For the VPSC models $G_{[100]}$ evolves from 0.54 to 0.80, 0.53, and 0.43 for perpendicular, oblique and parallel configuration, respectively. $P_{[010]}$ increases from 0.49 to 0.99, 0.99, and 0.62 for perpendicular, oblique and parallel configuration, respectively.

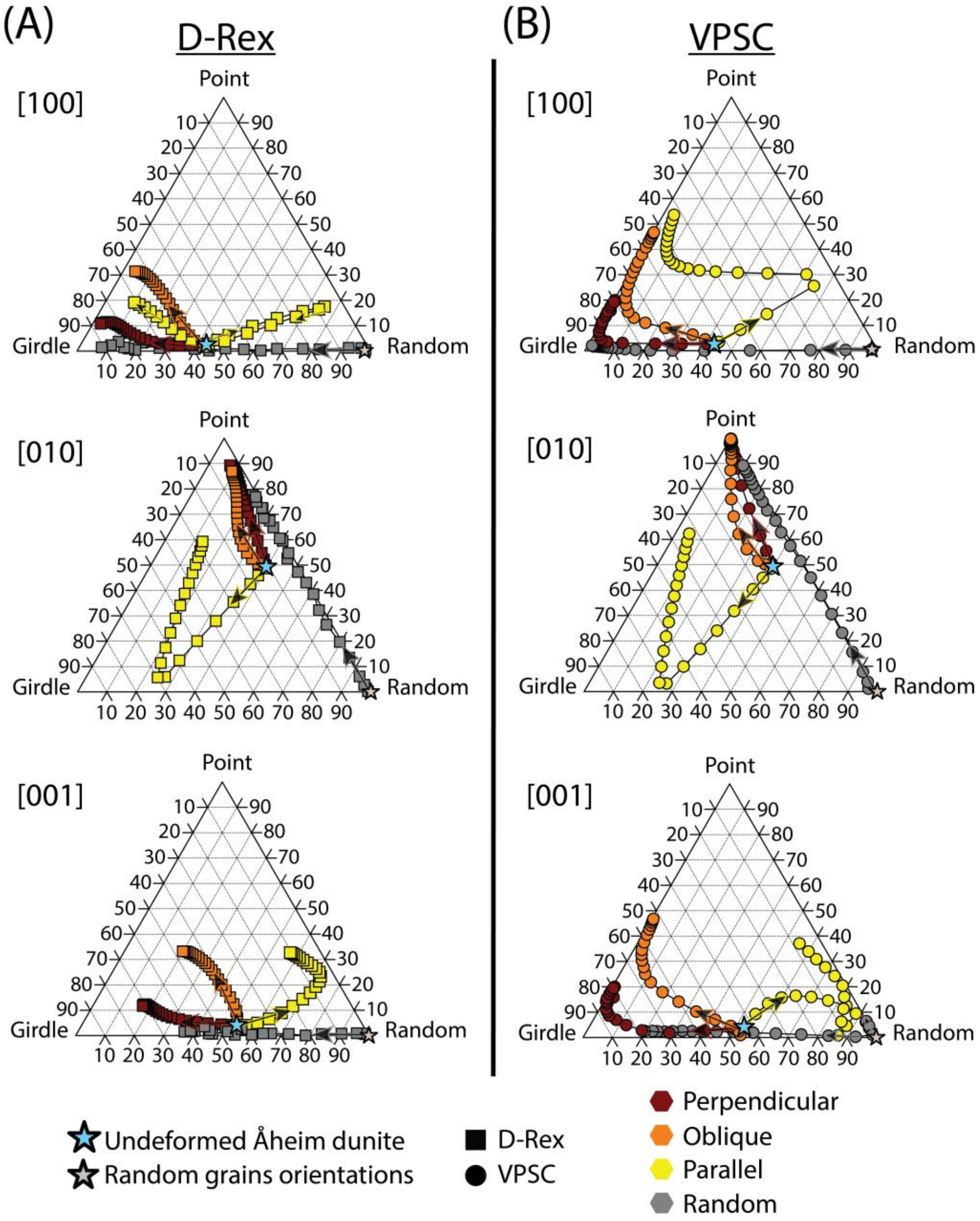

Figure 3.3 – Ternary diagram of texture symmetry parameters Point, Girdle and Random, calculated using eigenvalues of the orientation tensor (Vollmer, 1990), for: (A) D-Rex (square symbols), and (B) VPSC (circles symbols). There are total of 22 strain steps: ε = 0.01 and 0.05, and 20 steps in increments of 0.1 (from ε = 0.1 to 2). Three models with pre-existing configurations are shown: perpendicular (dark red), oblique (orange), and parallel (yellow), and an initially un-textured case is shown for reference (gray). Arrows show the initial trend of symmetry development from the initial texture. The symmetry of each configuration is shown to evolve differently as a function of strain.

D-Rex and VPSC show some notable differences in terms of their prediction of texture evolution. CPOs generated by the VPSC approach tend to evolve more quickly than CPOs generated by D-Rex. For example, in D-Rex the [100] axes in perpendicular and oblique configurations reach texture with Random parameter of $R_{[100]} < 0.05$ at 1.7 and 1.9 strain, respectively, while in VPSC $R_{[100]}$ requires strains of only 0.4 and 0.7, respectively. This effect is seen for the perpendicular and oblique configurations in the [001] axis as well. However, for the [010] axes the two models predict similar texture trajectories. The full set of texture data used in these calculations can be found in Table A3.1 and A3.2.

3.3.3 Texture strength and anisotropy

In order to further quantify the evolution of texture we calculate the total texture strength, using the M-index parameter (Skemer et al., 2005), and the maximum P-wave seismic anisotropy. The calculated texture strength and the associated seismic anisotropy are plotted as a function of strain (Fig. 3.4). Experimental data from Boneh and Skemer (2014) are shown as open symbols for comparison. Texture strength in D-Rex (Fig. 3.4A) for the perpendicular and oblique configurations show a small gradual increase of texture strength to values of $M = 0.36$ and $M = 0.31$, respectively (Fig. 3.4A), while the parallel configuration decreases slightly to a low and relatively constant value of $M = 0.13$. Texture strength in VPSC (Fig. 3.4B) for the perpendicular configuration shows an initial increase of strength up to strain of about 0.75 then a steady strength value until strain of 2 ($M = 0.45$ at $\varepsilon = 2$). For the oblique configuration the strength increases throughout the strain range ($M = 0.55$ at $\varepsilon = 2$). For the parallel configuration strength decreases initially and starts to increase again when the strain is about 1 ($M = 0.37$ at $\varepsilon = 2$). Texture strength of the initially random case after strain of 2 is slightly higher (D-Rex) or similar (VPSC) to the parallel configuration strength at the same strain (which is significantly lower than the perpendicular and oblique configurations). The texture strength in both models is stronger in the perpendicular and oblique configurations than in the parallel configuration.

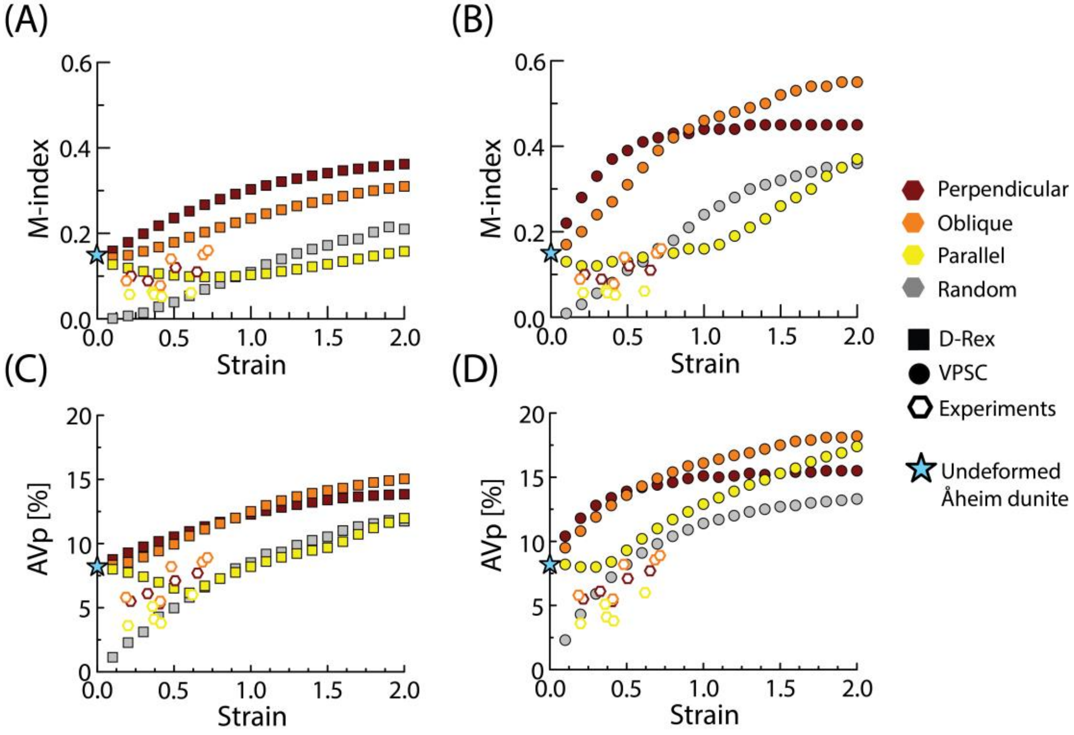

Figure 3.4 – Texture strength (A and B) and P-wave seismic anisotropy (AVp = 200 (Vp_{max} - Vp_{min}) / (Vp_{max} + Vp_{min})) (C and D) plotted as a function of strain. Numerical models are shown using solid symbols. Experimental data from Boneh and Skemer (2014) are shown as open symbols. Color denotes the configuration of the experiment or model: gray for initial random texture, dark red, orange, and yellow for perpendicular, oblique and parallel configuration, respectively. Texture strength is quantified using M-index (Skemer et al., 2005). Seismic anisotropy quantified using the maximum anisotropy of the P-wave velocity, in percent.

In Figures 3.4C and 3.4D, the P-wave seismic anisotropy in percentage (AVp = 200 (Vp_{max} - Vp_{min}) / (Vp_{max} + Vp_{min})) is shown with respect to strain for D-Rex and VPSC, respectively. In both models the trend of increasing seismic anisotropy with strain is similar although the models differ in terms of the magnitude of the anisotropy. Seismic anisotropy in D-Rex for the perpendicular and oblique configurations show a small gradual increase of texture strength to almost similar values of AVp = 14.8% and AVp = 15.5%, respectively (Fig. 3.4D), while the parallel configuration initially decreases to AVp = 4.6% at strain of 0.5 then increases up to AVp = 13.3% at strain of 2. Seismic anisotropy in VPSC for the perpendicular and oblique configurations shows a small gradual increase of texture strength to values of AVp = 15.5% and AVp = 18.2%, respectively (Fig. 3.4C), while the parallel configuration the seismic anisotropy stays at about to AVp = 8.2% for the strain of 0.5 and increases up to AVp = 17.4% at strain of 2.

3.4 Discussion

3.4.1 Texture evolution in uniaxial deformation experiments

The interpretation of seismic anisotropy relies on our understanding of the way crystals rotate and align in a polycrystalline aggregate under externally imposed deformation conditions. Nicolas et al., (1973) were the first to demonstrate how texture in olivine develops and strengthens as a function of strain in uniaxial compression. In these experiments, a CPO develops in which the [010] axes align parallel to the direction of compression and the [100] and [001] axes align within the radial plane, perpendicular to the compression axis. Put in terms of P, G, and R, the Nicolas et al., (1973) experiments predict that olivine in uniaxial compression should accumulate a strong $G_{[100]}$, $P_{[010]}$, and $G_{[001]}$, with a corresponding decrease in the R component of all three pole figures. For several decades, these experiments have provided an important basis for modeling and interpreting CPO and anisotropy in mantle rocks (e.g., Karato et al., 2008).

Building on the Nicolas et al. (1973) experiments, Boneh and Skemer (2014) showed the effect of deformation history on texture evolution in uniaxial compression. Unlike the Nicolas et al., 1973 experiments, which used samples with a weak pre-existing CPO, Boneh and Skemer conducted experiments on the Åheim dunite, which possesses a strong pre-existing texture.

Experiments were conducted in three different configurations to simulate distinct deformation histories. As with the Nicolas et al. experiments, Boneh and Skemer (2014) showed that texture evolves towards a symmetry characterized by strong point maxima in [010] and girdles in the [100] and [001] pole figures. However, for strains of ~ 0.6 – 0.7, texture evolution is still transient, and is far from the expected steady state, particularly in the oblique and parallel cases (Fig. 3.2). Moreover, each experimental configuration evolved differently as a function of strain. Here, we demonstrate that numerical models of texture evolution, run using identical starting conditions, lead to the same conclusions: that deformation history significantly influences the way texture accumulates with progressive strain (Fig. 3.2 - 3.4).

3.4.2 Comparison between numerical models and experiments

In general, comparison between numerical models and experiments reveals a similar texture signature but with significant differences in the CPO strength and the magnitude of the calculated anisotropy (Fig. 3.2 and Fig. 3.4). For the three configurations, models show the development of a [010] point maximum parallel to the shortening axis, in excellent agreement with the experiments (see further discussion in section 3.4.4). For the [100] and [001] axes there are some differences between the two models and the experiments (especially in the oblique and parallel configurations). For example, in the oblique configuration, D-Rex shows [100] and [001] point maximum near the X and Y directions, respectively while VPSC shows [100] and [001] point maximum near the Y and X directions, respectively (Fig. 3.2). In nearly all cases, the VPSC and D-Rex models overestimate the strength of the CPO, and therefore the magnitude of the seismic anisotropy.

With both the VPSC and the D-Rex models, parameterization is achieved mainly through comparison with laboratory experiments. The experimental benchmarks for the D-Rex models of Kaminski et al. (2004) and the VPSC models of Tommasi et al. (2000) are the experiments of Zhang and Karato (1995) and Nicolas et al. (1973). Both of these studies used olivine aggregates with near-random initial CPO. Hence, models parameterized through comparison with these experiments are not optimized to account for the effects of pre-existing texture, which should be ubiquitous in the upper mantle. In this study we have explored a range of model parameter space to determine those that best simulate CPO evolution in more complex geologic scenarios (Fig. 3.5).

As noted earlier, D-Rex includes three non-dimensional parameters that influence model results - M^*, λ^* and χ. We tested a range of values for each parameter ($M^* = 0 – 200$, $\lambda^* = 0 - 5$, and $\chi = 0 - 0.8$) and found that the M^* parameter has the most pronounced effect on the resulting texture while λ^*, and χ parameters have a relatively small influence that becomes negligible when recrystallization and recovery processes are slow (i.e., at low M^* values). Therefore, we use common values for grain nucleation and grain boundary sliding threshold: $\lambda^* = 5$ and $\chi = 0.3$ (Kaminski and Ribe, 2001; Kaminski et al., 2004) throughout the present study, and focus on the effect of parameter M^* on texture.

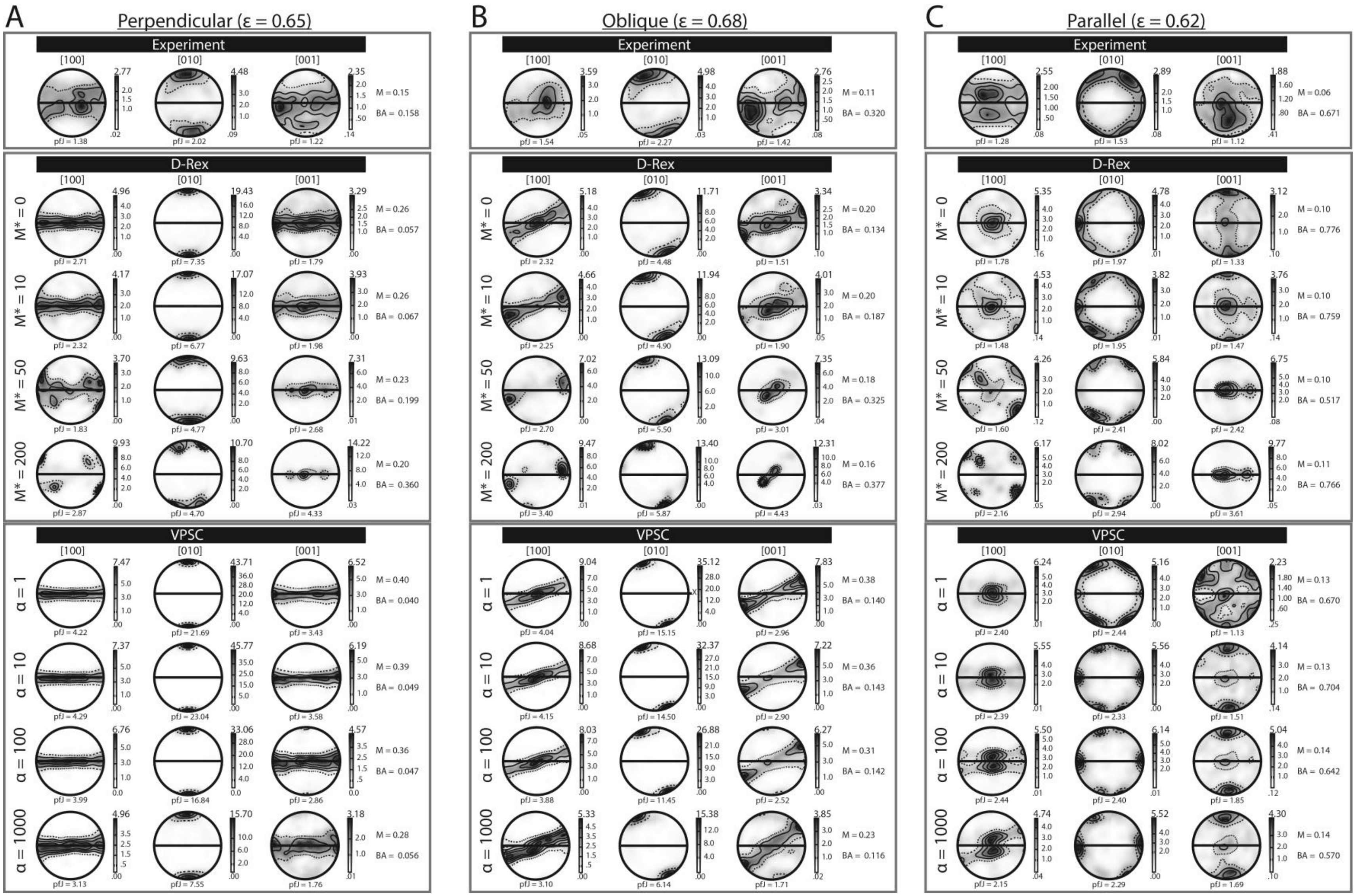
A
Perpendicular (ε = 0.65)
B
Oblique (ε = 0.68)
C
Parallel (ε = 0.62)
Experiment
D-Rex
VPSC
[100]
[010]
[001]
M* = 0
M* = 10
M* = 50
M* = 200
α = 1
α = 10
α = 100
α = 1000
M = 0.15
BA = 0.158
M = 0.26
BA = 0.057
M = 0.26
BA = 0.067
M = 0.23
BA = 0.199
M = 0.20
BA = 0.360
M = 0.40
BA = 0.040
M = 0.39
BA = 0.049
M = 0.36
BA = 0.047
M = 0.28
BA = 0.056
M = 0.11
BA = 0.320
M = 0.20
BA = 0.134
M = 0.20
BA = 0.187
M = 0.18
BA = 0.325
M = 0.16
BA = 0.377
M = 0.38
BA = 0.140
M = 0.36
BA = 0.143
M = 0.31
BA = 0.142
M = 0.23
BA = 0.116
M = 0.06
BA = 0.671
M = 0.10
BA = 0.776
M = 0.10
BA = 0.759
M = 0.10
BA = 0.517
M = 0.11
BA = 0.766
M = 0.13
BA = 0.670
M = 0.13
BA = 0.704
M = 0.14
BA = 0.642
M = 0.14
BA = 0.570

Figure 3.5 – Pole figures showing texture from experiments (top row), D-Rex (second through fifth rows), and VPSC (six through ninth rows) for the three starting configurations: perpendicular (A), oblique (B) and parallel (C). Models are shown for a range of parameters: for D-Rex, M* = 0, 10, 50 or 200, and for VPSC α = 1, 10, 100, or 1000. Experimental data is taken from high strain experiments of Boneh and Skemer (2014), and is the same as Figure 3.2. Scale bar to the right of each pole figure show the multiples of uniform distribution (m.u.d.). Pole figures projected in equal area and lower hemisphere. Texture strength of each pole figure (pfJ), the total texture strength (M-index) and texture symmetry (BA-index) are given.

Figure 3.5 shows model results for M^* values of: 0, 10, 50, and 200. Kaminski and Ribe (2001) showed that M^* between 50 to 200 fits textures from past experiments (Nicolas et al., 1973; Zhang and Karato, 1995) with larger values favored at higher temperatures when grain-boundary migration is more efficient. However, larger values of M^* appear to erase pre-existing texture efficiently or generate unexpected textures that are inconsistent with experimental results. Grain boundary migration (M^*) causes each grain to grow or shrink according to whether its strain energy is higher or lower than the average strain energy (eq. 14 in Kaminski and Ribe, 2001). The rate of new grain nucleation (λ^*) increases with higher ratio of dislocation density (eq. 4). Modeling both processes enhances texture evolution: grain nucleation produces a large volume fraction of strain-free nucleated grains that have the largest growth rate as they have the smallest strain energy compared to the average strain energy of the aggregate. Because the growth rate is proportional to both the difference in strain energy and the grain boundary mobility (M^*), the larger M^* the larger the growth rate of nucleated strain-free grains in soft orientations. For example, in Figure 3.5A we show CPOs generated in the perpendicular configuration. Experiments in this configuration produce an AG-type CPO with axial girdles in the [100] pole figures. However, in models for which M^* is large (50 and 200) the girdle is largely obscured by clusters of orientations that fall outside of the axial plane. Likewise, in Figure 3.5B, we see for M^* = 50 and 200 an elimination of the preexisting [100] girdle and the development of point maxima that are nearly perpendicular to the experimental observation.

Based on comparison with the Boneh and Skemer (2014) experiments we suggest that lower values of M^* (i.e., $M^* = 10$) may be more appropriate for modeling CPO evolution influenced by pre-existing texture. Although not considered here, future efforts may also benefit from implementation of D-Rex parameters that depend on both deformation mechanism and deformation history.

Using the VPSC model, we generate CPO pole figures with α values of 1, 10, 100, and 1000 (Fig. 3.5). The α parameter simulates grains interactions between two end members: when grains experience equal strain (α = 0) and when grains experience equal stress (α approaches infinity). The most commonly used values for α are α = 1, which is the tangent VPSC model (Lebensohn and Tomé, 1993; Molinari et al., 1987), and α = 10 -100, which assumes some relaxed strain compatibility (Tommasi et al., 2000). In Figure 3.5 we compare models for α = 1 – 1000. We find that α affects mainly the strength of the CPO and has only minor effect on the symmetry. The best fit with the experimental data is found to be α = 10 - 100. In the remainder of this study we chose to use α = 100.

3.4.3 The role of dynamic recrystallization and secondary deformation mechanism

Dynamic recrystallization by both subgrain rotation and grain boundary migration is expected and observed in experiments and nature. One of the main differences between the two numerical models is that D-Rex simulates the effects of dynamic recrystallization by nucleation and growth, while in our version of the VPSC model dynamic recrystallization is not modeled. Dynamic recrystallization in D-Rex is simulated by two processes, grain nucleation and grain boundary migration. The activity of these two recrystallization processes is controlled by the dislocation density. The effect of dynamic recrystallization is to increase the volume fraction of strain-free newly nucleated grains with a soft orientation relative to the imposed deformation. An example of the effect of dynamic recrystallization on texture can be seen in the [001] axis of the parallel configuration (Fig. 3.2C). For both models, there are two groups of grains that can be clearly seen as different maxima parallel to the Y and the Z axes. The first fraction of grains with [001] parallel to Z axis, have [100] orientated parallel to Y axis, and [010] parallel to X axis. This set of grains experience minimal rotation and have stayed approximately at their original orientation. The second fraction of grains with [001] oriented parallel to Y axis, have [100] oriented in an ‘x’ shape (D-Rex) or along the X – Y plane (VPSC), and [010] along the X – Z plane. These grains represent the population of grains that experienced significant reorientation. In D-Rex the two populations of grains represent a similar volume fraction of the aggregate while in VPSC the first fraction of grains (which represents grains with no rotation) is significantly larger than the second fraction of grains (which represents rotated grains). The experimental data show a dispersed [001] with a maximum around Y axis with no apparent point maxima parallel to the X axis. We interpret this observation to indicate that the pole figures from experiments contain very few grains from the fraction of relict orientations that experienced minimal rotation. Eliminating the extra [001] point maxima in D-Rex can be achieved by using a higher value for grain boundary mobility (*M**) although that will modify other aspects of texture and will yield a less ideal fit with the experiments.

A further element of D-Rex is a grain size threshold (χ) that simulates the activity of other deformation mechanisms such as diffusion creep and/or grain boundary sliding (GBS). This is implemented in a way that disables the rotation of small grains, hence decreasing the rate of evolution of the CPO when grain-size is reduced. Although the influence of diffusion creep and GBS on CPO evolution is complex (e.g. Wheeler, 2009), several observations have asserted that GBS acts to disperse texture (Skemer and Karato, 2008; Warren and Hirth, 2006). The high CPO strength in D-Rex, compared to experiments (Fig. 3.4A), suggests that an additional CPO weakening process for simulating GBS or diffusion creep mechanisms may be needed. Interestingly, although the pervasive recrystallization is observed in the samples from Boneh and Skemer (2014), the orientation and symmetry of the CPO simulated by VPSC is in good agreement with the experimental CPO (Fig. 3.2). This suggests that under some conditions grain size reduction via dynamic recrystallization causes a general CPO dispersion, weakening the texture but not significantly altering its symmetry or orientation.

Future versions of texture models may benefit from subroutines that progressively randomize texture when grain-size is reduced below a certain threshold and indeed there have been a number of recent advances in the simulation of dynamic recrystallization processes (e.g. the CDRX-VPSC model of Signorelli and Tommasi, 2015). Validation of new models will benefit from additional comparisons between existing models, such as the work by Castelnau et al. (2008), and comparisons with experimental results such as Boneh and Skemer (2014), applying the more stringent requirement that models must be able to reproduce a full spectrum of deformation histories.

3.4.4 Development of orthorhombic textures: transient or steady-state?

Under uniaxial deformation conditions, steady state CPO should be characterized by radial girdles of [100] and [001] axes and a point maximum in the [010] axis (Nicolas et al., 1973; Wenk et al., 1991). Girdles are expected in the [100] and [001] pole figures because under these imposed deformation conditions there is no preferred kinematic direction in the X-Y plane. Interestingly, Boneh and Skemer (2014) observed the development of an unexpected asymmetry in this texture: a point maximum in the [100] axis along the Y-axis (parallel to the strike of the foliation in the sample reference frame). In both VPSC and D-Rex models, the development of this point maxima is not observed when an initial random texture is used (gray symbols in Fig. 3.6A, B and C). However, in simulations initiated with a non-random texture, both VPSC and D-Rex predict a very dominant point maxima parallel to Y, in agreement with the experimental results. This is particularly apparent in the oblique and parallel configurations (Fig. 3.6B and 3.6C).

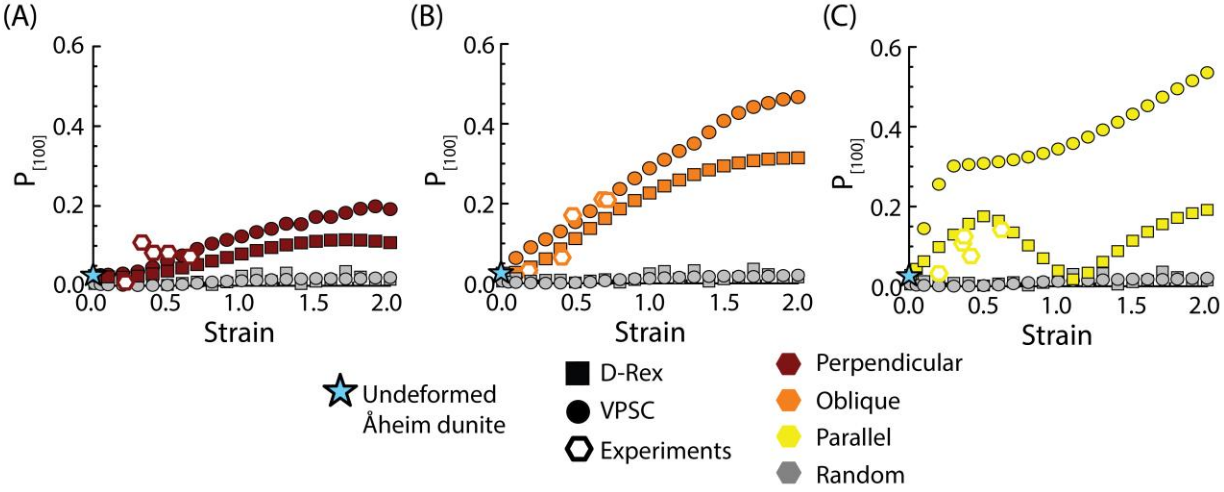

Figure 3.6 – The $P_{[100]}$ parameter is plotted versus strain for the three configurations: dark red for perpendicular (A), orange for oblique (B) and yellow for parallel (C) for D-Rex (squares), VPSC (circles) and experiments (open symbols). For reference, models initiated with a random texture are shown in gray (these results are the same in A, B, and C). Blue stars denote the initial $P_{[100]}$ of the undeformed Åheim dunite. Numerical models initiated with random textures do not display any perceptible increase in $P_{[100]}$ with strain. However models and experiments initiated using the pre-existing texture show a systematic increase of $P_{[100]}$ with strain, reflecting the generation and strengthening of CPOs with orthorhombic symmetries .

For the oblique and parallel cases, this quasi-orthorhombic texture under axial deformation can be explained when considering the influence of the pre-existing girdled texture. The [100] and [001] girdles in the Åheim dunite, in the oblique and parallel configurations, are in unstable positions with respect to the imposed deformation. However, within this girdle, a fraction of the grains have their [100] axes oriented along the foliation strike (Y axis). These grains, with the [100] axis already oriented parallel to the Y axis, do not need to rotate in order to align toward the X-Y plane; other grains with [100] axes oblique to the X-Y plane require some rotation to reach the steady-state orientation. Rotated grains are dispersed while the grains that do not rotate become a point maxima in the axis of rotation (Y-axis). This produces a transient pseudo-orthorhombic symmetry to the CPO.

For the perpendicular case, experiments and models are initiated with strong [100] and [001] girdles already oriented in accordance with the imposed deformation kinematics. Interestingly, a [100] point maxima still develops with strain, both for D-Rex and VPSC (Fig. 3.6A), although this behavior is not seen in models initiated with a random texture, which develop an almost ideal girdle in [100] (gray symbols in Fig. 3.3A, and 3.3B). A likely explanation is that the Åheim dunite does not have a perfect girdle to begin with and that the observed point maxima in models is a consequence of small initial perturbations in the natural CPO (Fig. 3.1A), which are enhanced with strain.

A critical question from the perspective of understanding CPO in the mantle is whether these textures are transient or steady state. If these textures are transient, how long are the transient CPOs maintained? If unexpected CPOs are preserved over long strain intervals this significantly changes the approach that must be used when interpreting seismic anisotropy in terms of mantle flow. To evaluate this, we look at how texture quantities vary as a function of strain. One way to quantify a coaxial texture, with a girdle in the [100] pole figure and a point maximum in the [010] pole figure, is through the BA-index defined in equation 3.6 (Mainprice et al., 2014). Figure 3.7 shows the BA-index development with strain for D-Rex and VPSC for the three different configurations with pre-existing texture and for an initial random texture. The models with an initial random texture exhibit a rapid decrease of the BA-index to extremely low, and apparently steady-state values (BA = 0.01 – 0.03 and 0.01 – 0.02 for D-Rex and VPSC, respectively). The strain required to reach this steady state value is minimal (ε ~ 0.2 - 0.3). This observation would imply that evolution of CPO is rapid and predictable. The pre-textured configurations also appear to reach a steady BA value however the strain required to reach this apparent steady state value is considerably larger, especially in the parallel configuration. Moreover, the magnitude in each configuration is significantly different (BA perpendicular > BA oblique > BA parallel > 0 for both models). The fact that the BA value of different configurations do not converge to zero illustrates the protracted effect of the initial texture on the ultimate steady-state. Models up to strains of 2 do not eliminate the inherited point maximum, and perhaps achieve a quasi-steady-state CPO that depends on the initial model conditions. Tests using D-Rex up to strains of ε = 10 observe no additional change in this observation.

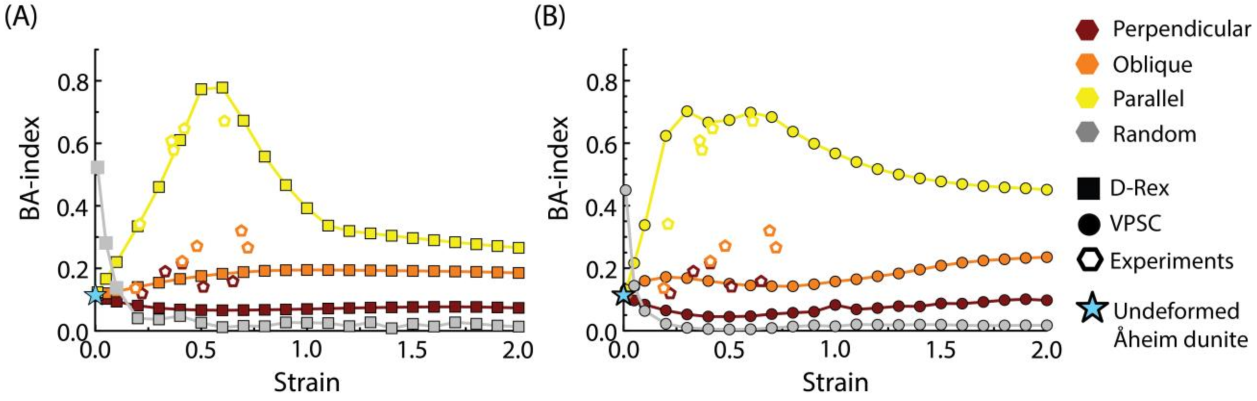

Figure 3.7 – The BA-index is plotted versus strain for D-Rex (A) and VPSC (B) for the three configurations: perpendicular in dark red, oblique in orange, and parallel in yellow. Models initiated with a random texture are shown in gray. Blue stars denote the initial $P_{[100]}$ of the undeformed Åheim dunite. Models initiated with a random texture converge rapidly to BA ~ 0, indicating that the CPO achieves a nearly perfect axial girdle (AG). All of the pre-textured configurations appear to stabilize at some non-zero BA-index, reflecting deviations from the idealized texture. There is no convergence of BA values at high strain, indicating that deformation history influences CPO symmetry over long transient strain intervals.

3.4.5 Seismic anisotropy resulting from transient CPO evolution

At the conditions prevalent in the upper mantle, convection driven flow at large or small scales will generate CPO as a natural consequence of deformation (Karato et al., 2008). Near plate boundaries, where deformation conditions and kinematics change rapidly, progressive deformation will continuously overprint a long and complex convective history. If texture evolution is slow in comparison to these changes, seismic anisotropy will reflect the transient nature of the CPO (Kaminski and Ribe, 2002; Lassak et al., 2006). Seismic anisotropy detects CPO strength, symmetry, and orientation but is primarily sensitive to the latter two characteristics.

The numerical simulations presented in section 3.3.2 emphasize that the details of the deformation history affect significantly the consequent CPO (Fig. 3.3). In Figure 8A-C, we show how these CPOs manifest as different seismic signatures. In Figure 3.8D-E, we show for comparison the calculated seismic anisotropy for three other common CPOs. This illustrates how different deformation histories may yield similar anisotropies – note for example, the similarity between the anisotropy generated in the parallel configuration and the anisotropy generated by a “B-type” fabric. Experiments and models are generally in agreement although the models over-predict the magnitude of anisotropy, in some cases by a factor of two. Experiments and models in the perpendicular configuration show the strongest agreement, which is to be expected because there is assumed to be no change in deformation kinematics between the pre-existing deformation and imposed deformation stages. Data for the parallel configuration are also in excellent agreement. The anisotropy in this configuration is quite distinct from the predicted steady-state anisotropy, with a strong P-wave velocity maximum parallel to the Y direction (see section 3.4.4). The oblique configuration shows the greatest difference between the experiment and the models. The fastest P-wave direction in the VPSC and in the experimental data is roughly parallel to the Y-direction, as is also seen in the parallel configuration. However, in the D-Rex model the fastest P-wave direction is sub-parallel to the X-axis (Fig. 3.8B). Hence the two models predict anisotropy that is roughly orthogonal. In general, all three deformation or simulation configurations predict distinct seismic signatures. In Fig. 3.9 P-wave velocities are shown with respect to the azimuth angle along the plane normal to the shortening axis (X-Y plane) for experiments, D-Rex, and VPSC (Fig. 3.9A, B and C, respectively). The P-wave velocities vary significantly depending on the direction of wave propagation for the oblique (experiments and VPSC) and parallel (experiments, D-Rex, and VPSC) datasets, reflecting the relict textures.

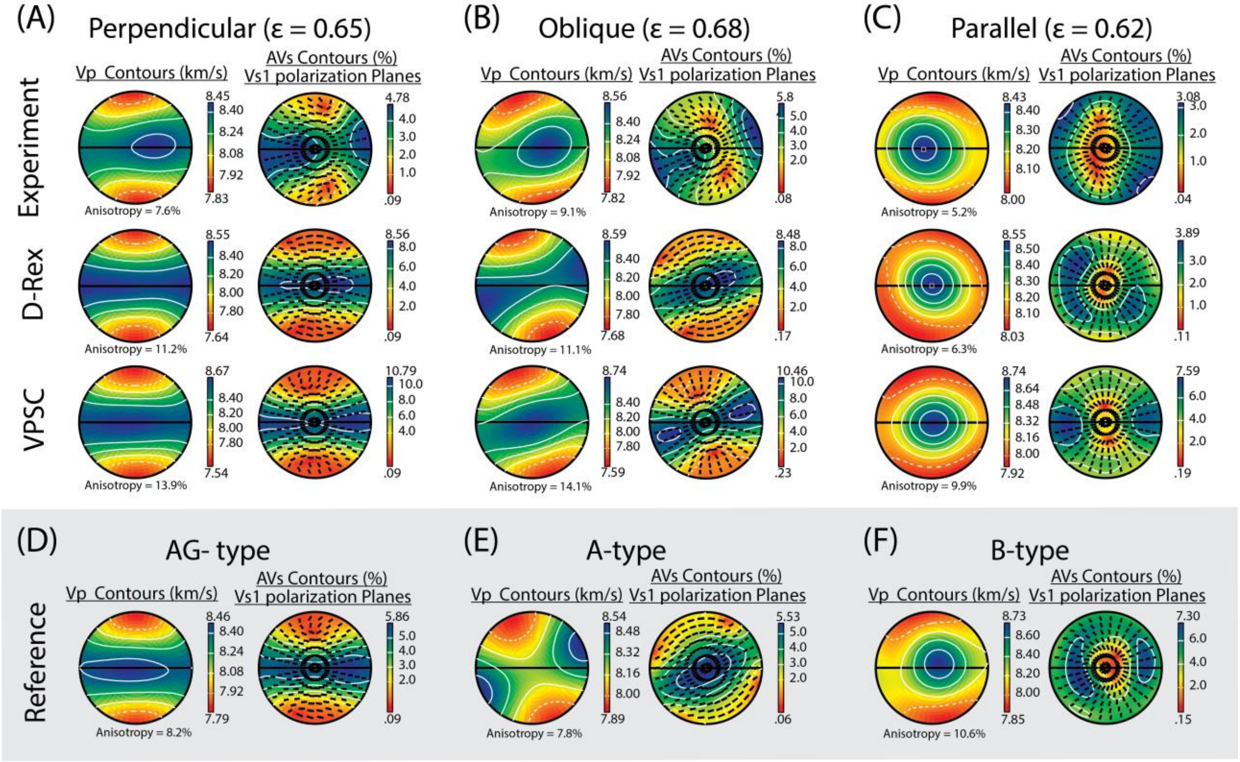

Figure 3.8 – Pole figures showing anisotropic seismic properties calculated from textures of experiments and models projected in the lower hemisphere. Three seismic properties are shown for each model or sample: Vp [km/sec] (left), AVs [%](AVs = 200 (Vs_{max} - Vs_{min}) / (Vs_{max} + Vs_{min}), color, and the polarization, vector, of the fast shear waves (right). Color contours ranges from red (low velocities) to

blue (high velocities). We show experiments and models for the three sample configurations: perpendicular (A), oblique (B) and parallel (C). Seismic anisotropy calculated for experiments and models are compared at the same strain, as in Figure 3.2. (D, E and F) Several reference samples to be compared with the present study: (D) an AG-type fabric, represented by undeformed Åheim dunite, (E) an A-type fabric (sample PI-284) from the experiments of [Zhang et al., 2000] deformed experimentally under anhydrous conditions in simple shear, and (F) a B-type fabric (sample JK-21), deformed experimentally by [Jung and Karato, 2001] under hydrous conditions in simple shear.

When CPO symmetries are orthorhombic (and hence do not exhibit transverse isotropy) a maximum in P-wave velocity along a specific radial azimuth is expected. This P-wave velocity maximum should be parallel to the X direction in A-type fabric and parallel to the Y direction for B-type fabric (Jung and Karato, 2001). Although both models and experiments have the same dominant slip system as the AG-type CPOs regardless of the initial configuration, transient texture development produces seismic anisotropy that may be similar signature to orthorhombic A-type or B-type textures. That suggests that the relationship between seismic anisotropies and mantle flow is non-unique in regimes where a transient stage of texture evolution is expected.

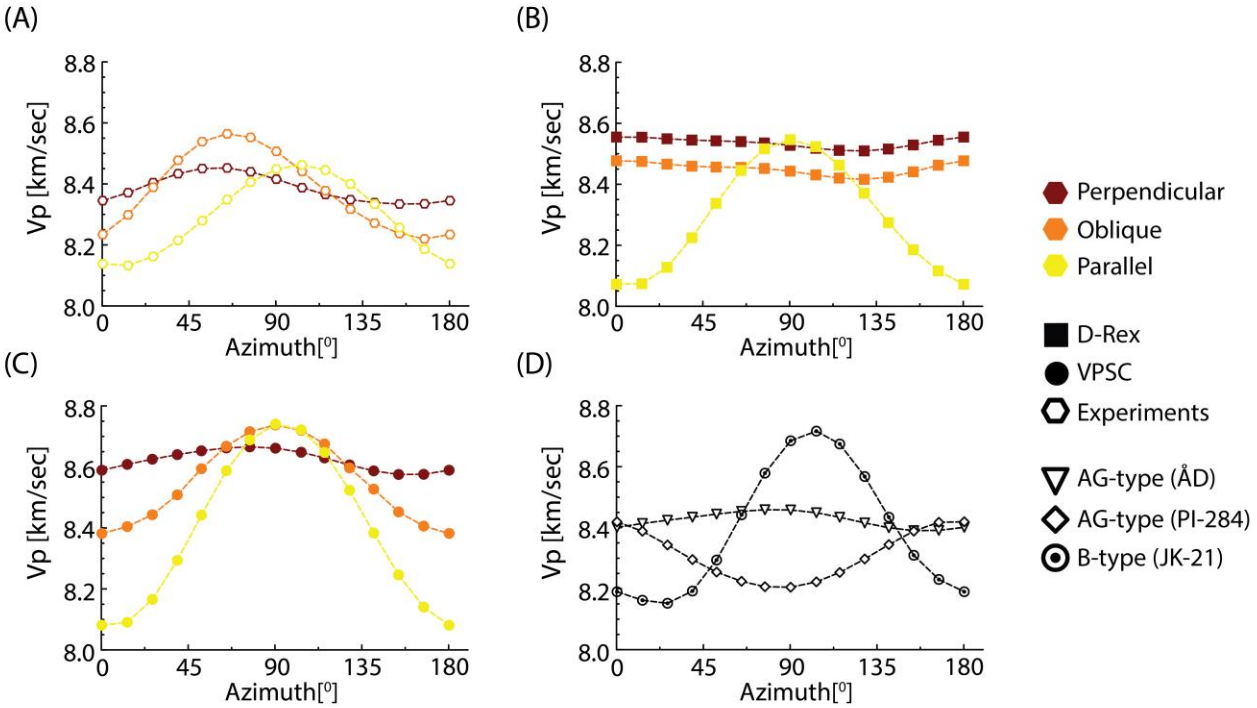

Figure 3.9 – P-wave velocity is plotted against azimuthal angle (in degrees) along the radial X – Y plane. 0 and 180 degrees correspond to the sample X direction; 90 degrees corresponds to the sample Y direction. Vp variation with respect to the azimuth angles is shown for perpendicular (dark red), oblique (orange), and parallel (yellow) configurations, in (A) experiments (hollow symbols), (B) D-Rex (square symbols), and (C) VPSC (circle symbols), respectively. (D) Variation of Vp with azimuth is calculated for the three reference textures shown in Figure 3.8D, 3.8E, and 3.8F. Samples with well-developed axial girdles exhibit the lowest azimuthal anisotropy. However, many samples, especially those deformed in the parallel configuration, exhibit significant anisotropy. The anisotropy of the samples in the parallel and oblique configurations have anisotropy signatures that are very similar to the B-type reference sample, although the CPOs were generated under very different conditions.

3.4.6 Simple shear deformation

In many plate boundary settings deformation is likely to include elements of both simple and pure shear (Tommasi et al., 1999). Indeed, recent models of mantle flow around subducting slab show that compressional or tensional coaxial deformation, due slab roll back and three-dimensional flow, could be the dominant deformation geometry in these settings (Di Leo et al., 2014; Faccenda and Capitanio, 2013; Kneller and van Keken, 2007; Long and Silver, 2009). To permit direct comparison between experiments and models, the present study focused on deformation with a uniaxial shortening geometry. However, to extend the results of this study to more general scenarios we have conducted some additional simulations of CPO evolution in simple shear.

Evolution of CPO in simple shear is illustrated through the rotation of the [100] maxima (approximating the fast seismic direction) as a function of strain (Fig. 3.10). The [100] maxima orientation, ψ, is defined here as the angle between the point maxima (i.e., the orientation of the largest eigenvalue) and the X direction. For these simulations a strong (M = 0.31) orthorhombic A-type CPO was created using D-Rex, with the [100] axes aligned parallel to the shear direction (X axis). This CPO was rotated, mainly along the XY, XZ, and YZ planes, for a total of 33 different initial orientations. This assortment of initial textures was then deformed in simple shear to a maximum strain of $\gamma = 5.5$ (Fig. 3.10). Due to the large strains required for these simulations, we show results only for the D-Rex model. The collection of curves shows two stages. At low to moderate strains CPO evolution is transient, with the [100] orientation are distributed broadly in orientation space. Most models exhibit a [100] maxima that is highly oblique to the shear direction, and there is significant variation amongst the different simulations. The second stage of evolution occurs at larger strains ($\gamma > 4$), in which a quasi-steady-state is reached, and the [100] maximum is generally within 0 - 10° of the shear direction. Notably, the critical strains required to reset pre-existing CPO are quite consistent with observations from natural samples (Skemer et al., 2012; Warren et al., 2008).

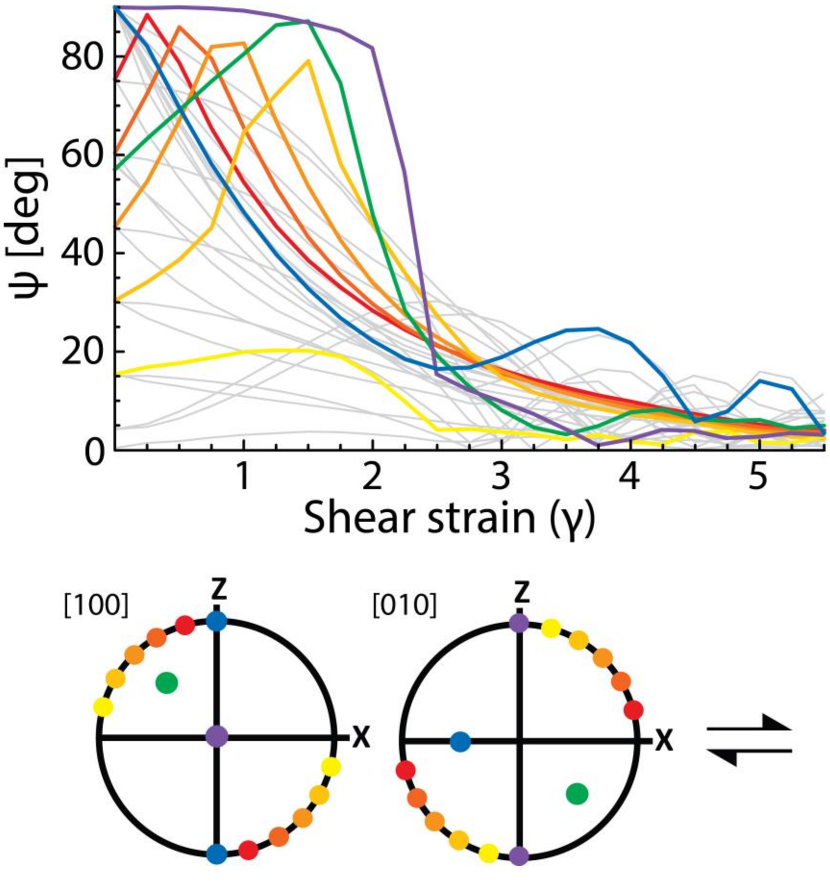

Figure 3.10 – Simple shear simulations generated using the D-Rex model ($M^* = 10$) for a range of initial orientations. To represent the first stage of deformation, a strong orthorhombic texture (M = 0.31) was rotated into 33 different orientations, mostly along the XY, XZ, and YZ planes. A second stage

of deformation was then imposed, up to $\gamma = 5.5$. CPO evolution is described by the angle of rotation, ψ, which is defined as the smallest angle between the [100] point maxima and the X direction (i.e., $0 < \psi < 90$). The curves show the evolution of ψ with respect to shear strain (γ), for each of the starting orientations. Of the 33 simulations, 25 are shown in gray to illustrate the range of possible orientations that might be expected given a large number of starting configurations. 8 representative simulations are shown in colors corresponding to specific initial configurations (shown in the key). Curves in yellow-orange-red reflect the scenario where a sample is sheared first with one shear sense, and then the opposite shear sense, along similar shear planes – a plausible scenario as material is advected through the mantle wedge. Collectively, these curves document a long transient stage ($\gamma = 0$ to ~4) where there is significant variability in CPO orientation, and a subsequent stage ($\gamma > 4$) where CPOs reach a quasi-steady state and the obliquity between the CPO and the flow direction is smaller and generally predictable.

3.5 Conclusions

In this study, D-Rex and VPSC models are used to evaluate texture evolution of olivine aggregates for a variety of initial conditions, simulating distinct deformation histories. These models were compared with recent experiments by Boneh and Skemer (2014). Both experiments and numerical models show that deformation history has a significant impact on the evolution of olivine CPO. For each of the initial deformation configurations, CPO and the consequent anisotropic signature is observed to evolve differently. Moreover, the evolution of CPO in each deformation configuration deviates markedly from the evolution of experiments and models initiated with random textures. In a uniaxial deformation geometry to strains of $\varepsilon = 2$, models in various configurations do not converge to the predicted steady-state texture. Models run to larger strains in simple shear, appear to converge to steady state textures at $\gamma > 3$. This is significantly larger than previously assumed, but is largely consistent with observations from mantle shear zones. It should also be noted that these critical strains for reorientation are similar in magnitude to strains generated by corner-flow in a subduction setting (e.g., McKenzie, 1979). As such, forward or inverse models that seek to relate seismic anisotropy to mantle flow must be cautious in their interpretations, as olivine appears to exhibit long transient intervals during which CPO has not reached steady state.

Appendix

Table A3.1. Summary of D-Rex runs with 22 strain steps of: texture symmetry, texture strength and seismic anisotropy for each of the initial configuration (see text for details).

Model	Configuration	Strain	$P_{[100]}$	$G_{[100]}$	$R_{[100]}$	$P_{[010]}$	$G_{[010]}$	$R_{[010]}$	$P_{[001]}$	$G_{[001]}$	$R_{[001]}$	BA-index	M-index	AVp [%]
D-Rex	Perpendicular	0.01	0.025	0.552	0.423	0.499	0.108	0.392	0.042	0.436	0.523	0.111	-	-
D-Rex	Perpendicular	0.05	0.024	0.574	0.402	0.523	0.103	0.374	0.043	0.458	0.500	0.102	-	-
D-Rex	Perpendicular	0.1	0.022	0.599	0.379	0.549	0.098	0.354	0.045	0.482	0.474	0.093	0.16	8.6
D-Rex	Perpendicular	0.2	0.022	0.641	0.337	0.596	0.088	0.316	0.049	0.525	0.426	0.081	0.18	8.6
D-Rex	Perpendicular	0.3	0.024	0.675	0.301	0.638	0.079	0.283	0.054	0.562	0.384	0.073	0.20	8.9
D-Rex	Perpendicular	0.4	0.030	0.704	0.267	0.675	0.072	0.253	0.059	0.594	0.347	0.068	0.22	9.4
D-Rex	Perpendicular	0.5	0.037	0.726	0.238	0.707	0.065	0.228	0.065	0.615	0.320	0.066	0.24	9.9
D-Rex	Perpendicular	0.6	0.045	0.744	0.211	0.734	0.060	0.207	0.071	0.638	0.291	0.066	0.25	10.4
D-Rex	Perpendicular	0.7	0.053	0.759	0.188	0.757	0.055	0.189	0.077	0.652	0.271	0.066	0.27	10.8
D-Rex	Perpendicular	0.8	0.062	0.772	0.166	0.778	0.050	0.173	0.084	0.662	0.254	0.067	0.28	11.4
D-Rex	Perpendicular	0.9	0.071	0.782	0.147	0.796	0.045	0.159	0.091	0.670	0.239	0.068	0.29	11.9
D-Rex	Perpendicular	1	0.080	0.790	0.130	0.812	0.041	0.147	0.097	0.677	0.226	0.070	0.30	12.4
D-Rex	Perpendicular	1.1	0.088	0.798	0.114	0.827	0.037	0.136	0.104	0.683	0.213	0.071	0.31	12.8
D-Rex	Perpendicular	1.2	0.096	0.804	0.101	0.840	0.034	0.126	0.109	0.688	0.203	0.073	0.32	13.2
D-Rex	Perpendicular	1.3	0.102	0.810	0.088	0.851	0.032	0.117	0.114	0.692	0.194	0.074	0.33	13.6
D-Rex	Perpendicular	1.4	0.107	0.816	0.076	0.861	0.030	0.109	0.118	0.696	0.187	0.075	0.34	14
D-Rex	Perpendicular	1.5	0.112	0.823	0.066	0.870	0.030	0.101	0.121	0.699	0.181	0.076	0.34	14.4
D-Rex	Perpendicular	1.6	0.114	0.830	0.056	0.877	0.030	0.094	0.123	0.701	0.176	0.077	0.35	14.8
D-Rex	Perpendicular	1.7	0.115	0.837	0.047	0.883	0.030	0.088	0.124	0.704	0.173	0.077	0.35	15
D-Rex	Perpendicular	1.8	0.114	0.846	0.040	0.887	0.031	0.082	0.123	0.707	0.171	0.076	0.36	15.2
D-Rex	Perpendicular	1.9	0.112	0.856	0.033	0.891	0.032	0.077	0.120	0.710	0.170	0.075	0.36	15.1
D-Rex	Perpendicular	2	0.108	0.865	0.027	0.893	0.033	0.074	0.117	0.713	0.170	0.073	0.36	14.8
D-Rex	Oblique	0.01	0.026	0.548	0.426	0.494	0.112	0.394	0.044	0.428	0.528	0.115	-	-
D-Rex	Oblique	0.05	0.025	0.558	0.417	0.499	0.122	0.379	0.056	0.421	0.523	0.120	-	-
D-Rex	Oblique	0.1	0.028	0.568	0.405	0.506	0.131	0.363	0.069	0.414	0.517	0.126	0.14	9.2
D-Rex	Oblique	0.2	0.041	0.581	0.379	0.525	0.143	0.332	0.097	0.404	0.499	0.140	0.15	10.2
D-Rex	Oblique	0.3	0.061	0.587	0.351	0.548	0.149	0.304	0.124	0.399	0.477	0.154	0.16	10.8
D-Rex	Oblique	0.4	0.086	0.591	0.323	0.575	0.148	0.277	0.151	0.398	0.451	0.166	0.17	11.3
D-Rex	Oblique	0.5	0.112	0.592	0.296	0.604	0.143	0.254	0.176	0.400	0.424	0.175	0.18	11.6
D-Rex	Oblique	0.6	0.138	0.592	0.271	0.631	0.135	0.234	0.200	0.402	0.398	0.182	0.19	11.9
D-Rex	Oblique	0.7	0.163	0.591	0.246	0.657	0.125	0.218	0.222	0.403	0.375	0.188	0.20	12.2
D-Rex	Oblique	0.8	0.187	0.591	0.222	0.682	0.115	0.203	0.242	0.404	0.354	0.192	0.21	12.5
D-Rex	Oblique	0.9	0.208	0.593	0.200	0.705	0.104	0.191	0.258	0.407	0.335	0.194	0.23	12.8
D-Rex	Oblique	1	0.226	0.595	0.179	0.727	0.093	0.179	0.273	0.410	0.317	0.195	0.24	13
D-Rex	Oblique	1.1	0.244	0.598	0.158	0.749	0.083	0.168	0.285	0.415	0.299	0.195	0.25	13.3
D-Rex	Oblique	1.2	0.259	0.601	0.139	0.769	0.073	0.158	0.296	0.421	0.283	0.194	0.26	13.6
D-Rex	Oblique	1.3	0.273	0.605	0.122	0.788	0.065	0.148	0.305	0.427	0.267	0.193	0.26	13.8
D-Rex	Oblique	1.4	0.284	0.609	0.107	0.805	0.058	0.138	0.314	0.434	0.253	0.192	0.27	14
D-Rex	Oblique	1.5	0.294	0.614	0.092	0.820	0.052	0.128	0.321	0.441	0.239	0.192	0.28	14.2
D-Rex	Oblique	1.6	0.302	0.619	0.080	0.834	0.048	0.119	0.326	0.447	0.227	0.191	0.29	14.4
D-Rex	Oblique	1.7	0.308	0.624	0.068	0.845	0.044	0.110	0.330	0.453	0.217	0.190	0.29	14.6
D-Rex	Oblique	1.8	0.311	0.631	0.058	0.855	0.042	0.103	0.332	0.459	0.209	0.189	0.30	14.9
D-Rex	Oblique	1.9	0.314	0.638	0.049	0.863	0.040	0.097	0.333	0.464	0.203	0.187	0.31	15.2
D-Rex	Oblique	2	0.315	0.645	0.041	0.870	0.039	0.092	0.332	0.469	0.199	0.185	0.31	15.5

D-Rex	Parallel	0.01	0.029	0.537	0.434	0.486	0.119	0.395	0.041	0.427	0.532	0.123	-	-
D-Rex	Parallel	0.05	0.044	0.499	0.458	0.459	0.154	0.387	0.040	0.415	0.546	0.166	-	-
D-Rex	Parallel	0.1	0.063	0.451	0.486	0.425	0.198	0.377	0.041	0.397	0.562	0.220	0.13	6.9
D-Rex	Parallel	0.2	0.098	0.353	0.549	0.354	0.291	0.355	0.050	0.355	0.595	0.335	0.12	5.9
D-Rex	Parallel	0.3	0.130	0.253	0.617	0.279	0.389	0.332	0.066	0.307	0.627	0.460	0.11	5.1
D-Rex	Parallel	0.4	0.157	0.151	0.692	0.200	0.492	0.308	0.090	0.253	0.657	0.610	0.11	4.4
D-Rex	Parallel	0.5	0.175	0.068	0.756	0.124	0.591	0.285	0.116	0.201	0.683	0.773	0.10	4.6
D-Rex	Parallel	0.6	0.164	0.093	0.742	0.059	0.672	0.269	0.144	0.154	0.703	0.778	0.10	5.1
D-Rex	Parallel	0.7	0.135	0.186	0.679	0.057	0.699	0.245	0.169	0.116	0.715	0.673	0.10	5.6
D-Rex	Parallel	0.8	0.102	0.288	0.610	0.114	0.659	0.227	0.193	0.085	0.722	0.557	0.10	6.1
D-Rex	Parallel	0.9	0.070	0.385	0.545	0.175	0.613	0.213	0.214	0.062	0.724	0.466	0.10	6.5
D-Rex	Parallel	1	0.039	0.477	0.484	0.233	0.567	0.200	0.233	0.048	0.719	0.392	0.10	7.4
D-Rex	Parallel	1.1	0.018	0.558	0.424	0.290	0.521	0.189	0.250	0.044	0.706	0.337	0.11	8.4
D-Rex	Parallel	1.2	0.034	0.594	0.371	0.341	0.479	0.180	0.264	0.049	0.688	0.319	0.11	9.4
D-Rex	Parallel	1.3	0.062	0.616	0.323	0.387	0.441	0.172	0.276	0.057	0.667	0.312	0.12	10.1
D-Rex	Parallel	1.4	0.088	0.633	0.279	0.429	0.406	0.165	0.287	0.066	0.647	0.304	0.12	10.8
D-Rex	Parallel	1.5	0.114	0.647	0.238	0.468	0.374	0.158	0.297	0.075	0.627	0.297	0.13	11.4
D-Rex	Parallel	1.6	0.137	0.660	0.203	0.502	0.347	0.152	0.307	0.083	0.610	0.290	0.13	12
D-Rex	Parallel	1.7	0.156	0.672	0.172	0.530	0.324	0.146	0.314	0.090	0.596	0.283	0.14	12.4
D-Rex	Parallel	1.8	0.172	0.684	0.144	0.556	0.304	0.140	0.321	0.096	0.584	0.277	0.15	12.8
D-Rex	Parallel	1.9	0.183	0.696	0.120	0.576	0.289	0.135	0.325	0.100	0.575	0.271	0.15	13.1
D-Rex	Parallel	2	0.192	0.709	0.100	0.593	0.277	0.130	0.327	0.105	0.568	0.266	0.16	13.3
D-Rex	Random	0.01	0.005	0.014	0.982	0.002	0.009	0.989	0.005	0.009	0.985	0.523		
D-Rex	Random	0.05	0.012	0.024	0.964	0.028	0.008	0.964	0.008	0.017	0.975	0.281		
D-Rex	Random	0.1	0.013	0.067	0.920	0.061	0.008	0.931	0.009	0.037	0.954	0.138	0.00	6.9
D-Rex	Random	0.2	0.007	0.170	0.824	0.135	0.006	0.859	0.008	0.089	0.903	0.040	0.01	5.9
D-Rex	Random	0.3	0.009	0.225	0.766	0.197	0.007	0.796	0.006	0.158	0.836	0.036	0.01	5.1
D-Rex	Random	0.4	0.009	0.313	0.677	0.265	0.019	0.716	0.001	0.216	0.784	0.048	0.03	4.4
D-Rex	Random	0.5	0.002	0.373	0.625	0.322	0.016	0.663	0.006	0.270	0.723	0.026	0.04	4.6
D-Rex	Random	0.6	0.007	0.427	0.566	0.385	0.003	0.612	0.008	0.329	0.663	0.012	0.05	5.1
D-Rex	Random	0.7	0.010	0.489	0.501	0.431	0.005	0.565	0.008	0.356	0.635	0.016	0.07	5.6
D-Rex	Random	0.8	0.002	0.549	0.449	0.473	0.012	0.515	0.004	0.398	0.598	0.014	0.08	6.1
D-Rex	Random	0.9	0.009	0.595	0.397	0.525	0.022	0.453	0.003	0.456	0.541	0.027	0.10	6.5
D-Rex	Random	1	0.025	0.627	0.348	0.548	0.007	0.445	0.026	0.421	0.553	0.026	0.11	7.4
D-Rex	Random	1.1	0.031	0.658	0.311	0.596	0.003	0.402	0.030	0.474	0.496	0.025	0.13	8.4
D-Rex	Random	1.2	0.012	0.713	0.275	0.605	0.008	0.387	0.016	0.474	0.511	0.015	0.14	9.4
D-Rex	Random	1.3	0.033	0.761	0.206	0.648	0.008	0.343	0.007	0.530	0.463	0.027	0.15	10.1
D-Rex	Random	1.4	0.004	0.799	0.197	0.675	0.008	0.318	0.008	0.542	0.450	0.008	0.16	10.8
D-Rex	Random	1.5	0.010	0.820	0.170	0.686	0.023	0.292	0.021	0.532	0.447	0.022	0.17	11.4
D-Rex	Random	1.6	0.015	0.832	0.154	0.723	0.008	0.270	0.018	0.585	0.397	0.014	0.18	12
D-Rex	Random	1.7	0.037	0.840	0.124	0.725	0.009	0.266	0.036	0.543	0.421	0.027	0.19	12.4
D-Rex	Random	1.8	0.023	0.872	0.105	0.750	0.015	0.235	0.016	0.596	0.388	0.023	0.20	12.8
D-Rex	Random	1.9	0.014	0.907	0.078	0.776	0.014	0.210	0.015	0.622	0.363	0.017	0.22	13.1
D-Rex	Random	2	0.015	0.908	0.077	0.768	0.009	0.223	0.019	0.599	0.382	0.014	0.21	13.3

Table A3.2. Summary of VPSC runs with 22 strain steps of: texture symmetry, texture strength and seismic anisotropy for each of the initial configuration (see text for details).

Model	Configuration	Strain	$P_{[100]}$	$G_{[100]}$	$R_{[100]}$	$P_{[010]}$	$G_{[010]}$	$R_{[010]}$	$P_{[001]}$	$G_{[001]}$	$R_{[001]}$	BA-index	M-index	AVp [%]
VPSC	Perpendicular	0.01	0.026	0.569	0.405	0.506	0.108	0.386	0.041	0.432	0.528	0.110	-	-
VPSC	Perpendicular	0.05	0.027	0.656	0.318	0.555	0.101	0.343	0.039	0.442	0.519	0.097	-	-
VPSC	Perpendicular	0.1	0.028	0.745	0.227	0.614	0.093	0.293	0.035	0.469	0.496	0.083	0.22	10.4
VPSC	Perpendicular	0.2	0.031	0.856	0.113	0.722	0.076	0.202	0.026	0.572	0.402	0.065	0.28	11.8
VPSC	Perpendicular	0.3	0.036	0.905	0.059	0.813	0.057	0.130	0.018	0.697	0.286	0.052	0.33	12.8
VPSC	Perpendicular	0.4	0.046	0.921	0.033	0.880	0.039	0.081	0.028	0.785	0.187	0.045	0.37	13.4
VPSC	Perpendicular	0.5	0.062	0.920	0.019	0.923	0.025	0.052	0.049	0.828	0.123	0.045	0.39	13.9
VPSC	Perpendicular	0.6	0.076	0.913	0.011	0.951	0.015	0.033	0.070	0.852	0.078	0.046	0.41	14.2
VPSC	Perpendicular	0.7	0.092	0.900	0.007	0.970	0.013	0.017	0.086	0.868	0.046	0.053	0.42	14.4
VPSC	Perpendicular	0.8	0.106	0.890	0.005	0.980	0.008	0.012	0.101	0.867	0.031	0.057	0.43	14.6
VPSC	Perpendicular	0.9	0.115	0.882	0.003	0.986	0.006	0.009	0.112	0.865	0.023	0.061	0.43	14.9
VPSC	Perpendicular	1	0.158	0.833	0.009	0.982	0.005	0.013	0.159	0.817	0.025	0.082	0.44	15.1
VPSC	Perpendicular	1.1	0.134	0.862	0.003	0.990	0.002	0.008	0.134	0.851	0.016	0.068	0.44	15
VPSC	Perpendicular	1.2	0.143	0.855	0.003	0.994	0.002	0.004	0.142	0.850	0.008	0.072	0.44	15.1
VPSC	Perpendicular	1.3	0.156	0.843	0.002	0.996	0.001	0.003	0.155	0.839	0.006	0.078	0.45	15.3
VPSC	Perpendicular	1.4	0.154	0.845	0.001	0.997	0.001	0.002	0.154	0.841	0.005	0.078	0.45	15.2
VPSC	Perpendicular	1.5	0.173	0.825	0.002	0.996	0.002	0.002	0.172	0.824	0.004	0.087	0.45	15.3
VPSC	Perpendicular	1.6	0.173	0.826	0.002	0.997	0.000	0.003	0.172	0.823	0.004	0.087	0.45	15.4
VPSC	Perpendicular	1.7	0.183	0.816	0.001	0.997	0.001	0.002	0.184	0.812	0.005	0.092	0.45	15.4
VPSC	Perpendicular	1.8	0.193	0.803	0.004	0.994	0.002	0.004	0.193	0.800	0.007	0.098	0.45	15.5
VPSC	Perpendicular	1.9	0.199	0.798	0.003	0.994	0.002	0.004	0.200	0.793	0.008	0.101	0.45	15.5
VPSC	Perpendicular	2	0.192	0.805	0.003	0.995	0.002	0.003	0.194	0.800	0.006	0.097	0.45	15.5
VPSC	Oblique	0.01	0.029	0.550	0.421	0.495	0.114	0.391	0.037	0.433	0.529	0.119	-	-
VPSC	Oblique	0.05	0.045	0.567	0.388	0.502	0.132	0.366	0.023	0.446	0.531	0.140	-	-
VPSC	Oblique	0.1	0.064	0.600	0.336	0.517	0.148	0.335	0.010	0.459	0.532	0.159	0.17	9.5
VPSC	Oblique	0.2	0.090	0.680	0.230	0.561	0.164	0.274	0.025	0.456	0.519	0.172	0.20	10.8
VPSC	Oblique	0.3	0.110	0.738	0.151	0.621	0.162	0.217	0.045	0.473	0.481	0.168	0.24	11.9
VPSC	Oblique	0.4	0.130	0.768	0.102	0.690	0.144	0.165	0.070	0.515	0.415	0.159	0.27	12.8
VPSC	Oblique	0.5	0.154	0.775	0.071	0.759	0.119	0.123	0.102	0.563	0.335	0.150	0.31	13.6
VPSC	Oblique	0.6	0.181	0.768	0.051	0.819	0.090	0.091	0.141	0.603	0.256	0.145	0.35	14.3
VPSC	Oblique	0.7	0.208	0.757	0.035	0.873	0.064	0.063	0.179	0.640	0.181	0.142	0.39	14.9
VPSC	Oblique	0.8	0.237	0.738	0.025	0.915	0.040	0.046	0.218	0.660	0.122	0.142	0.42	15.4
VPSC	Oblique	0.9	0.263	0.719	0.018	0.939	0.028	0.033	0.250	0.663	0.087	0.149	0.44	15.87
VPSC	Oblique	1	0.288	0.698	0.014	0.953	0.022	0.025	0.278	0.654	0.068	0.157	0.46	16.1
VPSC	Oblique	1.1	0.310	0.680	0.010	0.966	0.016	0.019	0.304	0.647	0.049	0.165	0.47	16.4
VPSC	Oblique	1.2	0.332	0.660	0.008	0.974	0.014	0.013	0.327	0.637	0.037	0.174	0.48	16.7
VPSC	Oblique	1.3	0.350	0.643	0.007	0.979	0.013	0.008	0.345	0.627	0.028	0.183	0.49	16.9
VPSC	Oblique	1.4	0.379	0.616	0.006	0.984	0.010	0.006	0.375	0.604	0.021	0.195	0.50	17.2
VPSC	Oblique	1.5	0.407	0.588	0.005	0.988	0.007	0.005	0.405	0.579	0.016	0.208	0.52	17.5
VPSC	Oblique	1.6	0.427	0.568	0.004	0.989	0.006	0.005	0.426	0.561	0.013	0.218	0.53	17.8
VPSC	Oblique	1.7	0.442	0.554	0.004	0.991	0.005	0.004	0.442	0.548	0.011	0.224	0.54	17.9
VPSC	Oblique	1.8	0.452	0.545	0.003	0.993	0.004	0.003	0.453	0.538	0.009	0.229	0.54	18.1
VPSC	Oblique	1.9	0.461	0.536	0.002	0.994	0.003	0.003	0.462	0.531	0.007	0.233	0.55	18.1
VPSC	Oblique	2	0.467	0.531	0.002	0.995	0.002	0.003	0.467	0.527	0.006	0.235	0.55	18.2

VPSC	Parallel	0.01	0.035	0.525	0.440	0.485	0.121	0.395	0.034	0.438	0.529	0.131	-	-
VPSC	Parallel	0.05	0.083	0.428	0.489	0.449	0.166	0.385	0.001	0.461	0.538	0.216	-	-
VPSC	Parallel	0.1	0.145	0.307	0.549	0.404	0.222	0.374	0.035	0.435	0.531	0.338	0.13	8.2
VPSC	Parallel	0.2	0.256	0.091	0.654	0.318	0.329	0.353	0.093	0.365	0.542	0.623	0.12	8
VPSC	Parallel	0.3	0.302	0.093	0.605	0.240	0.427	0.333	0.134	0.302	0.564	0.702	0.12	8
VPSC	Parallel	0.4	0.305	0.224	0.471	0.168	0.519	0.313	0.157	0.245	0.598	0.666	0.13	8.4
VPSC	Parallel	0.5	0.308	0.324	0.368	0.099	0.611	0.290	0.165	0.192	0.643	0.674	0.13	9.3
VPSC	Parallel	0.6	0.312	0.398	0.290	0.032	0.703	0.265	0.160	0.142	0.698	0.698	0.14	10.2
VPSC	Parallel	0.7	0.317	0.451	0.232	0.035	0.726	0.240	0.146	0.091	0.763	0.684	0.15	11
VPSC	Parallel	0.8	0.324	0.487	0.189	0.099	0.687	0.214	0.126	0.040	0.835	0.637	0.15	11.7
VPSC	Parallel	0.9	0.333	0.510	0.157	0.160	0.649	0.191	0.095	0.022	0.883	0.599	0.16	12.3
VPSC	Parallel	1	0.344	0.525	0.131	0.217	0.612	0.171	0.046	0.079	0.876	0.567	0.16	12.9
VPSC	Parallel	1.1	0.358	0.532	0.110	0.274	0.574	0.152	0.008	0.127	0.865	0.540	0.17	13.4
VPSC	Parallel	1.2	0.374	0.531	0.095	0.328	0.538	0.134	0.062	0.088	0.850	0.517	0.19	13.9
VPSC	Parallel	1.3	0.392	0.526	0.082	0.376	0.504	0.119	0.113	0.055	0.832	0.500	0.21	14.4
VPSC	Parallel	1.4	0.411	0.516	0.073	0.419	0.475	0.106	0.160	0.029	0.811	0.487	0.23	14.8
VPSC	Parallel	1.5	0.432	0.504	0.064	0.458	0.447	0.095	0.204	0.013	0.783	0.478	0.26	15.3
VPSC	Parallel	1.6	0.453	0.490	0.058	0.497	0.420	0.084	0.242	0.021	0.737	0.469	0.28	15.7
VPSC	Parallel	1.7	0.474	0.475	0.051	0.532	0.395	0.074	0.277	0.035	0.688	0.463	0.30	16.2
VPSC	Parallel	1.8	0.495	0.459	0.046	0.563	0.373	0.064	0.309	0.050	0.641	0.458	0.33	16.6
VPSC	Parallel	1.9	0.515	0.443	0.041	0.591	0.353	0.056	0.339	0.062	0.599	0.456	0.35	16.9
VPSC	Parallel	2	0.536	0.428	0.036	0.623	0.330	0.047	0.371	0.076	0.553	0.451	0.37	17.4
VPSC	Random	0.01	0.005	0.019	0.976	0.012	0.024	0.964	0.007	0.006	0.987	0.450	-	-
VPSC	Random	0.05	0.003	0.109	0.888	0.039	0.014	0.948	0.018	0.005	0.977	0.144	-	-
VPSC	Random	0.1	0.002	0.229	0.769	0.078	0.010	0.912	0.037	0.006	0.957	0.063	0.01	2.3
VPSC	Random	0.2	0.001	0.436	0.563	0.156	0.007	0.838	0.062	0.005	0.934	0.022	0.03	4.3
VPSC	Random	0.3	0.001	0.591	0.408	0.232	0.004	0.764	0.064	0.002	0.934	0.009	0.06	5.9
VPSC	Random	0.4	0.001	0.700	0.299	0.306	0.003	0.691	0.046	0.002	0.953	0.005	0.08	7.2
VPSC	Random	0.5	0.002	0.776	0.223	0.379	0.002	0.619	0.012	0.007	0.981	0.004	0.11	8.2
VPSC	Random	0.6	0.003	0.826	0.171	0.449	0.002	0.548	0.003	0.069	0.928	0.004	0.13	9.1
VPSC	Random	0.7	0.006	0.860	0.134	0.515	0.005	0.480	0.007	0.160	0.833	0.009	0.16	9.8
VPSC	Random	0.8	0.010	0.883	0.108	0.575	0.009	0.416	0.012	0.250	0.738	0.013	0.18	10.4
VPSC	Random	0.9	0.012	0.901	0.088	0.628	0.014	0.358	0.016	0.335	0.650	0.017	0.21	10.9
VPSC	Random	1	0.013	0.915	0.072	0.674	0.010	0.316	0.019	0.410	0.571	0.014	0.24	11.4
VPSC	Random	1.1	0.014	0.927	0.059	0.714	0.018	0.267	0.022	0.476	0.503	0.020	0.26	11.7
VPSC	Random	1.2	0.015	0.936	0.049	0.749	0.017	0.234	0.023	0.534	0.444	0.019	0.28	12
VPSC	Random	1.3	0.016	0.943	0.041	0.777	0.016	0.207	0.023	0.580	0.397	0.018	0.30	12.3
VPSC	Random	1.4	0.017	0.948	0.035	0.799	0.017	0.184	0.025	0.617	0.359	0.019	0.31	12.5
VPSC	Random	1.5	0.018	0.952	0.030	0.818	0.016	0.165	0.026	0.649	0.325	0.019	0.32	12.7
VPSC	Random	1.6	0.018	0.957	0.025	0.837	0.014	0.149	0.025	0.682	0.293	0.017	0.33	12.8
VPSC	Random	1.7	0.017	0.961	0.022	0.852	0.013	0.135	0.023	0.710	0.267	0.016	0.34	13
VPSC	Random	1.8	0.018	0.963	0.019	0.867	0.013	0.120	0.024	0.734	0.241	0.017	0.35	13.1
VPSC	Random	1.9	0.020	0.964	0.017	0.876	0.013	0.111	0.026	0.750	0.225	0.017	0.35	13.2
VPSC	Random	2	0.021	0.965	0.015	0.892	0.012	0.096	0.026	0.778	0.196	0.017	0.36	13.3

Chapter 4: Modeling olivine CPO evolution – Assessing model predictions for complex strain histories

Parts of this chapter are excerpted from:

Hansen, L. N., C. P. Conrad, Y. Boneh, P. Skemer, J. M. Warren, and D. L. Kohlstedt (2016), Viscous anisotropy of textured olivine aggregates: 2. Micromechanical model, J. Geophys. Res. Solid Earth, 121, doi:10.1002/2016JB013240.

Abstract

The relationship between flow in the upper mantle and seismic anisotropy is often simulated using one of several numerical tools (e.g., Castelnau et al., 2009; Dawson and Wenk, 2000). In order to make robust predictions for how olivine CPO evolves with different patterns of mantle flow, numerical models for predicting olivine CPO must be able to account for variety of deformation patterns and histories (e.g., Chapters 2 and 3). In this study, two commonly-used numerical models for simulating olivine CPO, VPSC and D-Rex, using the parameterization developed in Chapter 3 , are used to reproduce four different deformation configurations from experiments and from a shear zone in the Josephine Peridotite (Hansen and Warren, 2015; Hansen et al., 2016; Hansen et al., 2014). The deformation configurations differ in their stress tensor and/or their strain history. The CPO evolutions is quantified using measures of the texture's strength, orientation, and symmetry. In general, both models were found to overpredict the textural strength but are able to reproduce successfully the CPO orientation and symmetry. D-Rex, which implements a scheme for dynamic recrystallization, predicts better the weaker textural strength and the alignment of orientation of the reference examples in comparison to the predictions by VPSC. VPSC dramatically overpredicts the textural strength. It is concluded that

models are able to reproduce different deformation geometries and strain histories well in terms of the orientation and symmetry but poorly in terms of the magnitude of texture strength.

4.1 Introduction

Globally, flow in the mantle is characterized by upwelling at mid-oceanic ridges and downwelling at subduction-zones (e.g., Turcotte and Oxburgh, 1972). However, even this simple flow pattern incorporates various deformation geometries (McKenzie, 1979), which will influence the relationship between deformation history and texture evolution (Castelnau et al., 2009; Skemer et al., 2012). Both aspects of deformation geometry and history need to be taken into account when modeling deformation in the mantle. CPO evolution models are used when interpreting seismic anisotropy to infer flow kinematics (inverse modeling) or when using geodynamic models of mantle flow to predict characteristics of seismic anisotropy (forward modeling). Both inverse and forward modeling require a clear understanding of how olivine CPO evolves with complex strain histories, and the use of appropriate numerical tools in simulating texture evolution in the mantle (Lev and Hager, 2008).The experiments of Boneh and Skemer (2014) investigated the effect of pre-existing texture on CPO evolution and demonstrated that evolution of olivine CPO towards steady-state require larger strains when such effects are considered. Furthermore, Boneh et al., (2015) showed that the effect of deformation history can be seen also in numerical models of textural evolution (VPSC and D-Rex), which were previously parameterized only by comparison with experiments initiated with no pre-existing texture. Here, I will use VPSC and D-Rex (with the new parametrization determined in Boneh et al., 2015) to simulate deformations in four different configurations with different deformation geometries or pre-existing texture. The CPO evolution of the models is compared with CPO evolution from experiments (Hansen et al., 2016; Hansen et al., 2014), and a natural shear-zone

(Hansen and Warren, 2015). The models' reliability in reproducing CPO evolution from experiments and natural shear-zone will be assessed.

4.2 Methods

4.2.1 VPSC and D-Rex - parameterization and comparative Data

I use the numerical models VPSC (Tommasi et al., 2000) and D-Rex (Kaminski and Ribe, 2001), which are described in section 3.2. The parametrizations used in these calculations are the one found in Boneh et al., (2015) to account best for the effects of deformation history – $\alpha = 100$ (VPSC) and $M^* = 10$, $\lambda = 5$, and $\chi = 5$ (D-Rex).

Models are compared to data from experiments and from a natural shear zone. Experimental data on olivine CPO evolution was originally published by Hansen et al., (2014) and Hansen et al., (2016a) and data from a shear zone in the Josephine Peridotite by Hansen and Warren (2015). The experiments were performed in a Paterson apparatus at the University of Minnesota at 300 MPa confining pressure and T = 1200 °C. Deformation was achieved in both extension and torsion deformation geometries (Figure 4a). Starting samples composed of Fo50 powder were hot-pressed, resulting in an aggregate with no significant olivine CPO (Hansen et al., 2014, and 2016a). The CPO evolution from within the Josephine shear-zone is used as an example of a situation in which the pre-existing outcrop-scale texture of the peridotite is overprinted by subsequent localized deformation (e.g., Skemer et al., 2010; Warren et al., 2008).

4.2.2 Texture parameter

In order to quantify and accurately compare different CPO we use three texture elements (described in detail in Section 2.2): strength, orientation, and symmetry (Boneh et al., 2014).

Texture strength is quantified using statistical tools either related to the orientation distribution function (ODF) using the 'J-index' (J) (Bunge, 2013), or by the distribution of misorientation axis between all grains using the 'M-index' (M) (Skemer et al., 2005). J- ranges between 1 (random distribution of orientations) and infinity (single crystal) and M ranges from 0 (random distribution of orientations) and 1 (single crystal). Texture orientation is quantified using the angle between the corresponding eigenvectors λ_1, λ_2, and λ_3 with respect to the deformation axis (shear direction). The orientation of the olivine [100] axis is quantified by the angle between the largest eigenvector (λ_1) orientation and the shear direction. The orientation of olivine [010] and [001] axes tend to spread along a plane, forming a girdle, and their orientation is quantified using angle between the smallest eigenvector (λ_3) and the shear direction. For example when the girdle is oriented along the shear plane, the largest and intermediate eigenvectors λ_1 and λ_2 will be oriented somewhere along the shear plane, and λ_3 will be oriented normal to the shear direction. Texture symmetry is quantified using the parameters: P, G, and R (Vollmer, 1990). These parameters are a function of the eigenvectors (see eq. 2.1-2.3, Section 2.2.2) and they reflect how much the texture is aligned to one direction - point maxima (P), spread along a plane - girdle (G), or scattered randomly (R).

4.2.3 Deformation configurations

Four deformation configurations are considered: (1) extension, (2) torsion, (3) torsion, post-extension, and (4) simple shear with an initial CPO of the Josephine peridotite. Deformation in torsion has a non-coaxial geometry and is used in experiments for achieving high shear-strains; near the edge of the deforming cylinder deformation is nearly simple shear (Paterson and Olgaard, 2000).

Figure 4.1 shows the four deformation configurations used in this chapter. The strain history for each deformation configuration is different. For deformation configuration of (uniaxial) extension (Fig. 4.1a), experiments and models start with random crystallographic orientation (i.e., J-index ~ 1 and M-index ~ 0) and run to maximum strain of 1. For deformation configuration of torsion (Fig. 4.1b), experiments and models start with random crystallographic orientation as well. Experiments were sheared up to shear strain of ~20, however the models run only to strain of 10 due to numerical instabilities in high strains. For deformation configuration of torsion post-extension (Fig. 4.1c), experiments were run to strain of 3, and the comparable models run to strain of 5. The initial texture was taken from the extension experiment (Fig. 4.1) with strengths of J-index = 3 and M-index = 0.1. For deformation configuration of the Josephine shear-zone -initial texture of the Josephine peridotite deformed in simple shear (Fig. 4.1d), the field data and models are shown up to shear strain of 5. The initial texture of the Josephine peridotite has strengths of J-index = 3.8, M-index = 0.09.

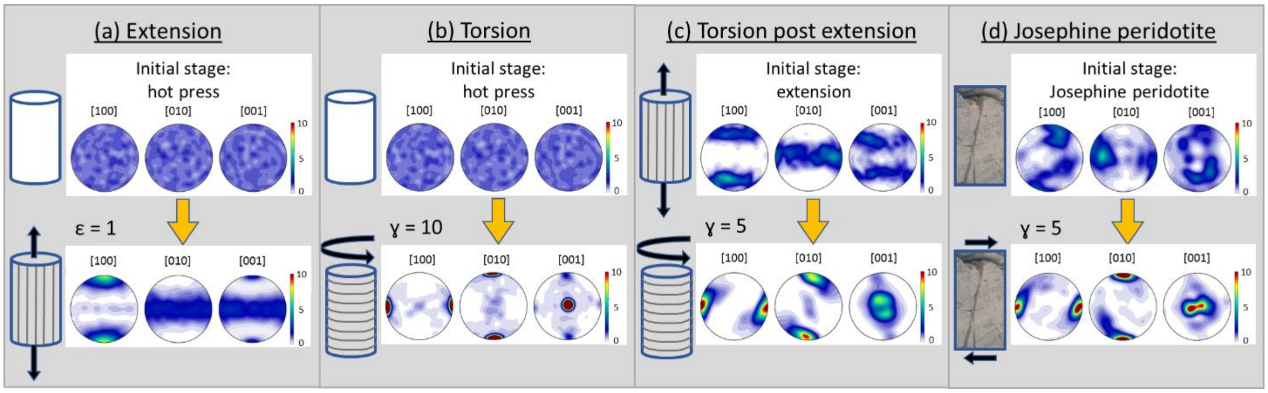

Figure 4.1 – Deformation configurations used in this chapter. (a) Extension – deformation in uniaxial extension starting with no initial texture (hot pressed). (b) Torsion – deformation in non-coaxial shear geometry starting with no initial texture. (c) Torsion post-extension – deformation in non-coaxial shear geometry starting with initial texture derived from a previous deformation stage of extension, i.e., deformation in (a). (d) Josephine peridotite – deformation in coaxial simple shear starting with an initial texture of the Josephine peridotite. Pole figures show the olivine CPO for [100], [010] and [001] (from left to right) with multiples of uniform distribution ranges from 0 to 10 (shows as a bar on the right). The CPO pole figures at the top row shows the initial CPO. In order to illustrate the expected final CPO at the maximum strain used for each configuration I show the pole figures predicted by D-Rex (bottom row).

4.3 Results

The results section will compare predictions of models with the data-set from literature for each texture element: strength (Section 4.3.1), orientation (Section 4.3.2), and symmetry (Section 4.3.3). For each section the CPO for the four deformation configurations will be shown.

4.3.1 Texture strength

The strength of CPO for the four deformation configurations is shown in Figure 4.2 using the J-index (left column) and the M-index (right column). In extension, the evolution of textural strength is minimal for the relatively small range of uniaxial extensional strains (ε = 0 – 1). The maximum strengths are J = 4.0 and M = 0.11 for the experiments, J = 5.8 and M = 0.24, for VPSC, and J = 1.9 and M = 0.04 for D-Rex. VPSC and D-Rex follow the general trend of increasing strength seen in the experiments where VPSC and D-Rex slightly over- or under-predict the strength in the experiments, respectively.

In torsion, experiments show an initial increase of texture strength with strain up to ɣ = 5 followed by a stable though variable strength for shear strains between ɣ = 5 – 20, where strengths range between J = 10 - 30, and M = 0.35 - 0.65. The models follow the initial increase in the texture strength of the experiments for strain range of ɣ = 0 – 5, however, for larger shear strains, ɣ > 5 the J-index and M-index exhibit different strength evolution. The J-index exhibits similar behavior for VPSC and D-Rex models: both continuously increase with strain (up to J = 40-50) significantly over-predicting the texture strength observed in the experiments. In contrast, M-index calculations indicate that strength evolution of D-Rex follows the initial increase and then stabilized around a strength in the range of the experiments (M = 0.35 – 0.5), while strength of the texture predicted by the VPSC model increases continuously up to M = 0.6 - 0.7.

For deformation in torsion post-extension, for both experiments and models, the texture strength systematically increases over the strain range shown (ɣ = 0 – 3), however, VPSC significantly overpredicts the strengths while D-Rex predicts a weaker texture that is more consistent with the experiments.

For the Josephine shear-zone, the texture from the field does not show a significant change in textural strength with strain. Models, as seen in the torsion and torsion post-extension configurations, show a systematic increase of the texture strength.

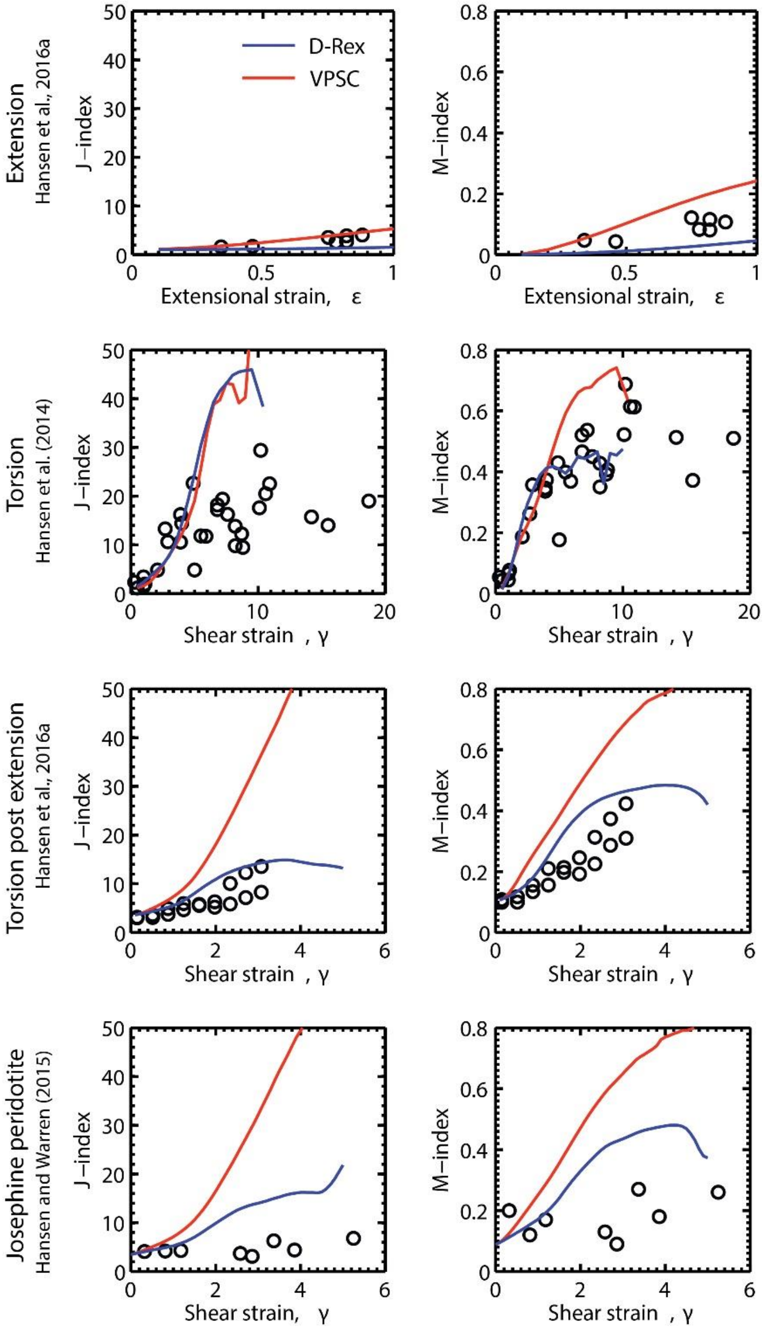

Figure 4.2 – Texture strength represented by J-index and M-index plotted as a function of strain. VPSC (red line) and D-Rex (blue line) models are compared with experimental and field data from Hansen and Warren (2015), Hansen et al., (2016a), and Hansen et al., (2014) (black circles). The evolution of texture strength is shown for the four deformation configurations shown in Figure 4.1: extension, torsion, torsion post extension, and an example from the Josephine peridotite. Modified from Hansen et al., (2016b).

4.3.2 Texture orientation

The evolution of CPO orientation for the four deformation configurations is shown in Figure 4.3, represented by the angle between the maximum and minimum eigenvector (λ_1 and λ_3) and the shear direction.

In extension, the evolution of the orientation varies monotonically, and is reproduced well by the models for the [100] and [010] axis. However, for the [100] axis the experiments show a small angle between λ_1 and the extension direction, which is not predicted by the models. There is also a large discrepancy between the experiments and models for the [001] axis where the angle between λ_3 and the maximum extension direction is between 50-90° in the experiments but close to 0° (i.e., aligned with the direction of maximum stress) in the models.

In torsion, the evolution of the texture orientation is characterized by an initial stage of rapid rotation for shear of $\gamma = 0 – 3$, followed by a steady orientation for larger strains ($\gamma = 3 – 20$). For the [100] axis the experiments have the λ_1 rotating towards the shear direction, aligning with the shear direction at $\gamma = 3$. D-Rex shows a similar orientation evolution as the experiments, but VPSC predicts that the λ_1 orientation stabilizes at a 20-degree angle to the shear direction, which is not seen in the experimental data. For the [010] axis, the experiments have the λ_3 rotate rapidly towards the shear direction with quasi-steady alignment at $\gamma = 3$, however both models show non-stable behavior of the texture, which is indicated by large variations of the [010] λ_3 orientation. For the [001] axis, experiments show scattering around angle of ~20 - 40° of λ_3 to the shear direction. D-Rex predicts smaller λ_3 angle then the experiments, and VPSC predicts values in the range of the experiments.

For deformation in torsion post-extension, after initial rotation of the λ_1 [100], λ_3 [010], and λ_3 [001] from normal to the shear direction towards the shear direction the orientation stabilized at $\gamma \sim 3$ with an angle of 15 - 20° to the shear direction. Generally, the experiments and models agree with each other for the [100], [010], and [001] axis.

For the Josephine shear-zone, the reorientation of the CPO with strain is slower than the model predictions for [100] axis. For the [010] axis, VPSC fit the field data well but D-Rex show unstable texture orientation. For the [001] axis the orientation is very scattered (similarly to the scatter observed for [001] in other deformation configurations).

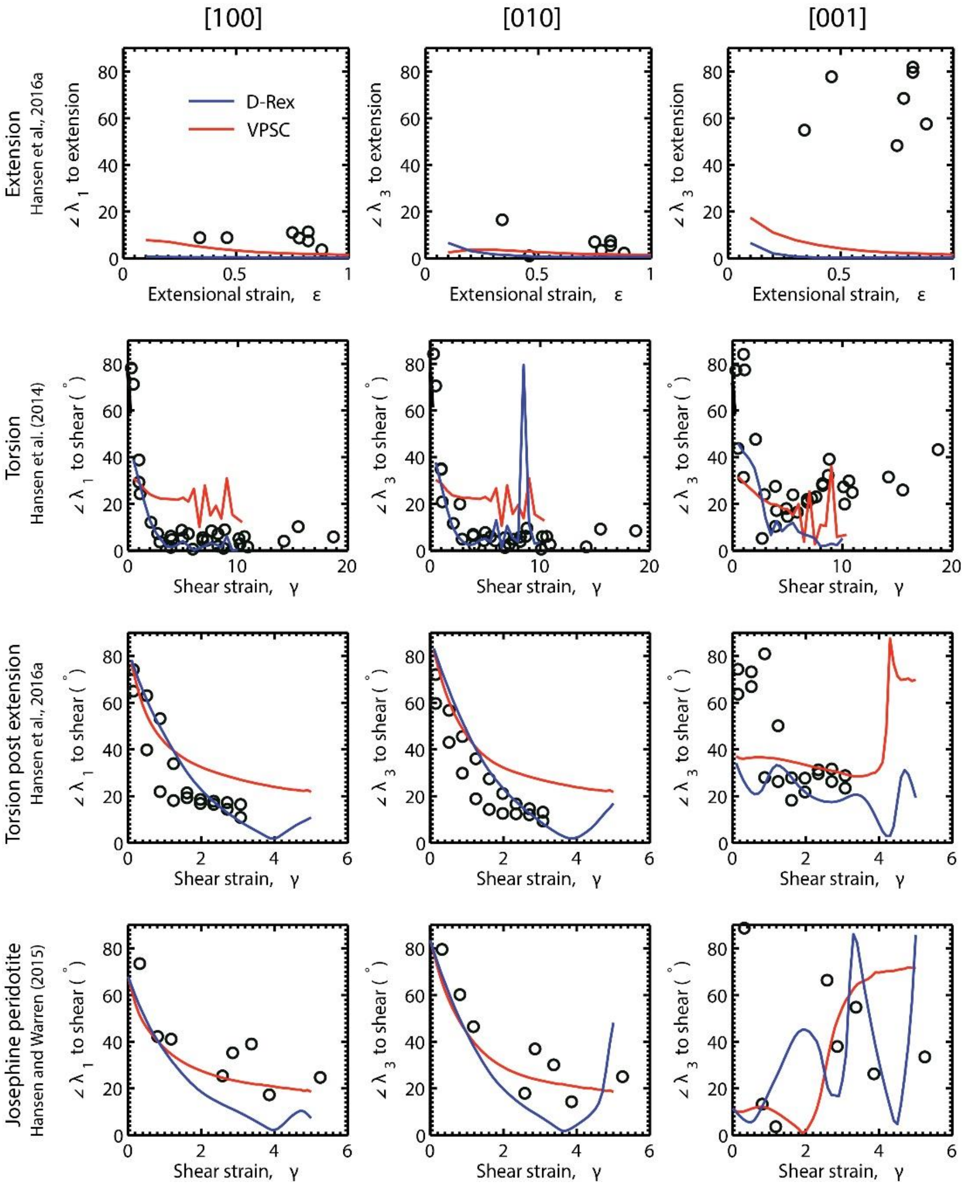

Figure 4.3 – Evolution of the textural orientation shown by the angle between [100] λ_1 and the extension or shear direction (left column), the angles between [010] λ_3 to the extension or shear direction (middle column), and the angle between [001] λ_3 to the extension or shear direction (right column). VPSC (red line) and D-Rex (blue line) models are compared with data from the literature (black circles)(Hansen and Warren, 2015; Hansen et al., 2016; Hansen et al., 2014). Modified from Hansen et al., (2016b).

4.3.3 Texture symmetry

The CPO symmetry for the four deformation configurations is shown in Figure 4.4 using P-G-R ternary diagrams. In extension, the evolution of textural symmetry is relatively minor.

The experiments $P_{[100]}$ axis gradually increases with strain, which is consistent with the model predictions (although the models over-predict the magnitude of P). For the [010] axis the texture symmetry of the experiments show a development of a girdle, which is predicted by the models as well. For the [001] axis the experiments show no symmetry development (random, $R_{[001]} \sim 1$) while both models predict development of a girdle similarly to the one predicted for [010].

In torsion, the experiments symmetry evolution with strain is more scattered but generally develops into a strong point maxima (especially the $P_{[100]}$). For the symmetry of the [010] axis the experiments show a dominant $G_{[010]}$ for the low-medium strains replaced by a dominant $P_{[010]}$ for the high strains. The two models predict the increase of $P_{[010]}$ with differences in the $G_{[010]}$ component: the $G_{[010]}$ in VPSC is much stronger and fits the experiments better than the $G_{[010]}$ in D-Rex.

For deformation in torsion post-extension, experiment's $P_{[100]}$ and $P_{[010]}$ show a clear increase, a trend, which is predicted by the models (again, models overpredict the strength of P). For the [001] axis the experiments develop a dominant girdle component ($G_{[001]}>P_{[001]}$), which is not reproduced by the models.

For Josephine shear-zone, the field samples show minor evolution of the symmetry component. However, models, as expected show a clear strong trend of strengthening for the three axes.

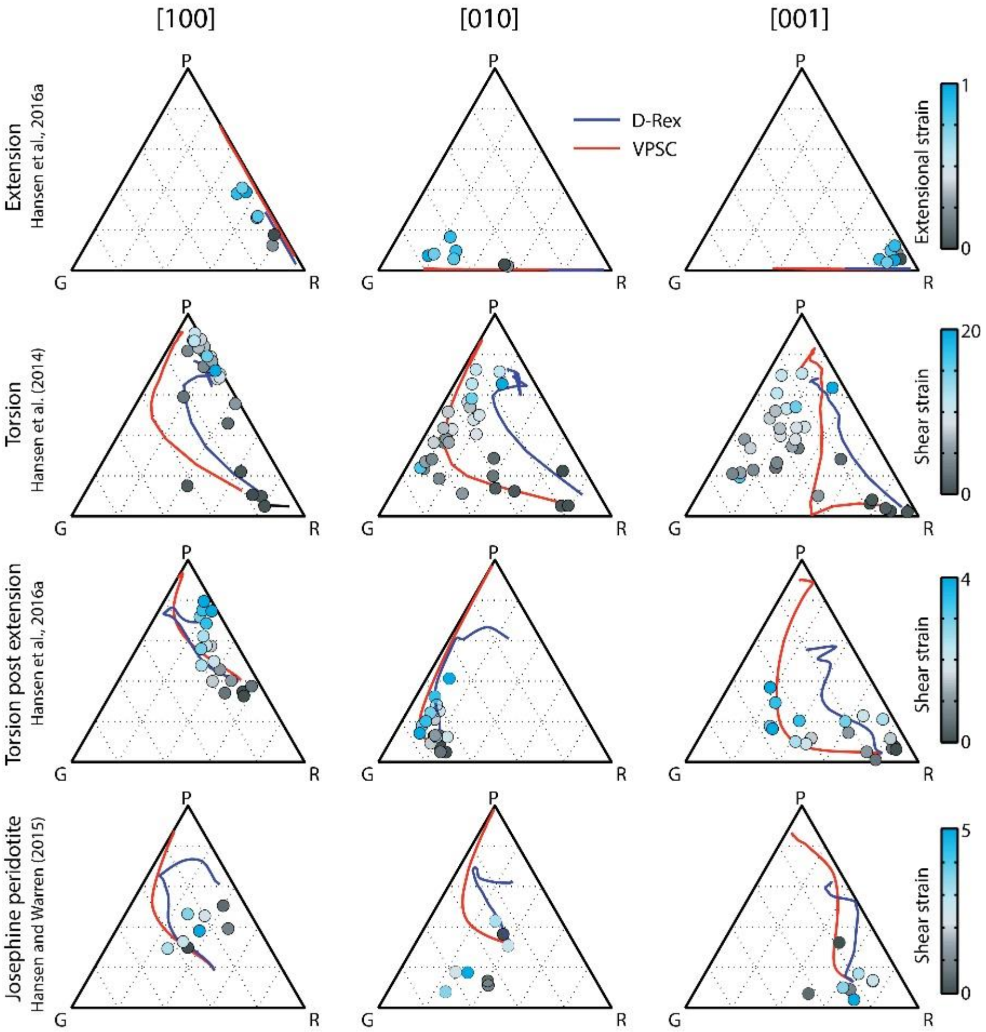

Figure 4.4 – Evolution of the textural symmetry shown by ternary diagrams of P (point maxima), G (girdle) and R (random). Coloring of the samples data points reflect strains (black to blue shown on the left bar). VPSC (red line) and D-Rex (blue line) models are compared with data from the literature (circles)(Hansen and Warren, 2015; Hansen et al., 2016; Hansen et al., 2014). Symmetry is shown for the four deformation configurations shown in Fig. 4.1: extension, torsion, torsion post extension, and Josephine peridotite. Modified from Hansen et al., (2016b).

4.4 Discussion and Conclusions

Interpreting olivine CPO can be complicated when the sample texture evolved due to a sequence of deformation stages with different deformation geometries (Chapters 2 and 3; also, see Skemer and Hansen, 2016). Chapters 2 and 3 focused on CPO evolution under deformation in a uniaxial compression geometry and the effect of a change in the compression direction (i.e., ‘perpendicular’, ‘oblique’, and ‘parallel’). However, flow in the mantle is associated with a variety of deformation geometries, which may include axial extension, simple shear, and more general shear. The texture simulations in this chapter follow four deformation configurations with uniaxial extension and/or simple shear. Previously published work with the same deformation configurations allow us to assess and compare them with models predictions.

The simulations, in general, predict well the CPO evolution of the extension experiments. Interestingly, the symmetry of [001] axis in these experiments show no significant CPO ($R_{[001]}$ ~ 0), although the models predict a development of a girdle (Fig. 4.4). The CPO due to extension is less developed compared with the models which may suggest higher activity of recovery processes such as grain boundary migration during extension.

Three of the four configurations deform in shear, and differ by their starting texture, i.e. ‘Torsion’, ‘Torsion post extension’, and ‘Josephine peridotite’ (Fig. 4.1b, c, and d, respectively). An important element of deformation in simple shear is the induced rotation of CPO. The rotation of CPO towards shear direction is important for the interpretation of fast seismic direction as the direction of mantle flow (e.g., Skemer et al., 2012). Comparing the angle between [100] λ_1 and shear direction for the three deformation configurations reveals the effect of the pre-existing texture on CPO rotation. Experiments with no initial texture (‘Torsion’) show [100] axes aligned with shear direction at $\gamma = 3$. However, in samples starting with initial texture (‘Torsion post extension’) the [100] axes rotate more slowly and are still ~15-20° away from the shear direction at $\gamma = 3$. The models show less variation in the CPO evolution between experiments started with randomly oriented and pre-textured samples probably due to the relatively weak pre-existing texture from the extension experiment. D-Rex includes the effects of dynamic recrystallization, which facilitates the alignment of [100] with shear direction as previously shown in experiments (e.g., Zhang and Karato, 1995). For this reason, D-Rex better predicts the CPO orientation in the experiments in comparison to VPSC.

The CPO from the Josephine shear-zone shown to be weaker and slower to evolve. Most noticeable is the difference in texture strength. The CPO strength from the shear zone is significantly weaker compared with both models and experiments. This suggests that, at least under these conditions, CPO in the mantle may be weaker than CPO from experiments or models. Secondary phases or other heterogeneities may explain some of the difference between the CPO from Josephine peridotite and the synthetic samples used in the experiments by Hansen et al., (2014) and Hansen et al., (2016a). The models further overpredict the texture strength since they assume deformation merely by dislocation-creep (which induces a crystallographic rotation and CPO) but do not include other deformation mechanisms that do not develop or even potentially weakens an existing CPO (such as: dislocation climb, diffusion creep, or grain-boundary-sliding) (e.g., Fliervoet et al., 1999; Wheeler, 2009). The strong texture developed by the models also leads to numerical instabilities which can be seen in both models when the strains are high ($\gamma > 5$). These are not observed in the experiments and are interpreted to be numerical artifacts.

To conclude, both the widely-used D-Rex and VPSC models predict well the dominant features of CPO evolution from experiments and from the field with couple of drawbacks. Since VPSC does not include dynamic recrystallization, it over-predicts textural strength and is unable to reproduce some of the lattice-rotations. D-Rex predicts better the textural evolution and the textural strength, although its physical meaning is more elusive and relies on some ad-hoc assumptions.

Chapter 5: Oriented grain growth and modification of 'frozen anisotropy' in the lithospheric mantle

An edited version of this chapter will be submitted to *'Geophysical Research Letters'* of the American Geophysical Union.

Boneh Y., Wallis D., Hansen L., Krawczynski M. J., Skemer P., Oriented grain growth and modification of 'frozen anisotropy' in the lithospheric mantle, *In prep*.

Abstract

Seismic anisotropy throughout the oceanic lithosphere is often assumed to be generated by fossilized texture formed during deformation at asthenospheric temperatures close to the ridge. Here we investigate the effect of high-temperature and high-pressure static annealing on the texture of previously deformed olivine aggregates to simulate residence of deformed peridotite in the lithosphere. Our experiments indicate that the orientation and magnitude of crystallographic preferred orientation (CPO) will evolve due to the preferential growth of grains with low dislocation densities. These observations suggest that texture and stored elastic strain energy promote a style of grain growth that modifies the CPO of a deformed aggregate. We demonstrate that these microstructural changes alter the orientation distributions and magnitudes of seismic wave velocities and anisotropy. Therefore, static annealing may complicate the inference of past deformation kinematics from seismic anisotropy in the oceanic lithosphere.

5.1 Introduction

The upper mantle is seismically anisotropic (Burgos et al., 2014; Schaeffer and Lebedev, 2013), which is mainly attributed to elastically anisotropic olivine crystals aligned in a crystallographic preferred orientation (CPO) (Ben Ismaïl and Mainprice, 1998; Mainprice, 2015;

Nicolas and Christensen, 1987). CPO in olivine is typically interpreted to result from solid-state plastic deformation. As such, interpretation of seismic anisotropy is the primary approach for inferring the kinematics of mantle flow (e.g., Christensen, 1984; Karato et al., 2008; Skemer and Hansen, 2016a).

The interpretation of seismic anisotropy is particularly challenging near plate boundaries, where flow patterns are complex (e.g., Boneh and Skemer, 2014; Skemer et al., 2012). However even beneath the interiors of oceanic plates, which are assumed to be kinematically simple, there is still vigorous debate about the depths, magnitudes, and orientations of seismic anisotropy (e.g., Becker et al., 2014; Lin et al., 2016). Many studies assume that the orientation of anisotropy in the highly viscous lithospheric mantle is "locked-in" and records the kinematics of deformation during its formation at the mid-ocean ridge, while anisotropy in the asthenosphere is continuously overprinted by current plate motion. This basic model is supported by numerous studies that detect layered anisotropy in both the oceanic and continental lithosphere (e.g., Barruol et al., 1997; Silver and Chan, 1991; Silver and Savage, 1994; Wolfe and Silver, 1998; Yuan and Romanowicz, 2010).

However, the validity of this model rests on two assumptions: first, that due to temperature-dependent changes in rock rheology the mantle does not deform significantly below a certain temperature, and second, that deformation is the only process that affects CPO. Here, we explore this second assumption by investigating the influence of high temperature and high pressure static annealing on the stability of olivine CPO.

5.2 Methods

The starting material for these experiments was a synthetic Fo_{50} olivine aggregate, which was previously deformed in torsion at 0.3 GPa and 1200° C in a Paterson apparatus at the

University of Minnesota (sample PT0718; for full description of the sample fabrication and deformation see: Hansen et al., 2016). Fo_{50} is a reliable analogue to Fo_{90} olivine in terms of its mechanical and textural behavior, but has a lower viscosity under the same deformation conditions, which facilitates high shear strain torsion experiments (Hansen et al., 2012a; Hansen et al., 2014; Hansen et al., 2012b; Zhao et al., 2009). We cut the deformed sample into three equal-sized slices along longitudinal sections parallel to both the radial direction and the axis of the initially cylindrical sample. As the sample was deformed in torsion, there is a linear gradient in shear strain from the outer edge to the center of the cylinder. The portions of the sample used in this study were deformed to shear strains from $\gamma = 7–10$.

Following the torsional deformation, olivine grains in the sample are 11 ± 8 µm in size, with aspect ratios of approximately 2:1. The olivine CPO is strong, with [100] axes parallel to the shear direction and [010] axes perpendicular to the shear plane, which corresponds to the A-type CPO of (Jung and Karato, 2001) (Fig. 5.1a). The narrow size distribution of dynamically recrystallized grains, the strength of the CPO, and comparison to samples deformed to a wide range of strains in similar experiments suggest that the microstructure is near steady-state (Hansen et al., 2012a; Hansen et al., 2014; Hansen et al., 2012b).

In the annealing stage of the experiments, the samples were held at constant temperature and hydrostatic pressure, using $BaCO_3$ and MgO as the pressure medium and spacers respectively, in a solid-medium piston-cylinder apparatus. Each sample was surrounded with Fo_{50} powder, which was identical to the powder used to synthesize the original sample, and packed inside a nickel capsule. The three samples were annealed at 1 GPa and 1250° C for 4, 20, or 168 hours, respectively. During each run, pressure was increased to 1 GPa at room temperature and then temperature was increased by 50° C per minute with a 6 minute pause at 900° C to allow the system to stabilize. Samples were quenched by shutting off the power to the furnace, which reduces the sample temperature to less than 100° C in under 30 seconds.

Thick sections of the annealed samples were prepared with a cross sectional area of ~ 1 mm^2 oriented parallel to the Y-Z plane of the starting deformed sample, i.e., within the plane that includes the radial direction (Y-axis) and the normal to the shear plane (Z-axis), and perpendicular to the shear direction (X-axis)(Fig. 5.1). Samples were polished using SiC and diamond abrasives down to 0.25 micron, followed by chemical-mechanical polishing using colloidal silica. Microstructural elements including grain size, intra- and inter-granular misorientation, and crystallographic orientation were characterized in two stages. First, large areas were mapped using conventional electron backscatter diffraction (EBSD). These data were acquired using a JEOL 7001-FLV scanning electron microscope (SEM) at 20 kV with an Oxford Instruments Nordlys F+ EBSD detector. Second, key areas were selected and mapped using high-angular resolution EBSD (HR-EBSD, Wallis et al., 2016; Wilkinson et al., 2006). These data were acquired using an FEI Quanta 650 field emission gun SEM at 30 kV with an Oxford Instruments Nordlys S EBSD detector. All data were acquired with SEMs operated in low-vacuum mode. EBSD maps have a step size of either 1 or 5 microns and HR-EBSD maps have a step size of 0.6 μm. Data were analyzed using Oxford Instruments HKL software and MTEX – a MATLAB based toolbox for analyzing crystallographic textures (Mainprice et al., 2014). Extrapolation of unindexed pixels was performed using an HKL noise reduction algorithm, in which pixels with five adjacent pixels with common orientation were filled. Selected additional extrapolation was conducted manually, using band-contrast imaging to identify boundaries between grains. HR-EBSD post-processing uses cross-correlation of regions of interest in diffraction patterns to achieve angular resolution of approximately 0.01° in misorientation angles (Wilkinson et al., 2006). This method is used to quantify lattice distortion by measuring the intracrystalline angular curvature variations and expressing these values as a density of geometrically necessary dislocation (GND) (El-Dasher et al., 2003; Ruggles and Fullwood, 2013). See Wallis et al. (2016) for further details of this method.

5.3 Results

Experimental samples show a distinct and progressive change in microstructure as a function of the duration of static annealing. These microstructural changes include an evolution of the grain-size distribution and a marked change in dislocation density. Figure 5.1 presents representative EBSD maps of the grain-scale microstructure and pole figures of the CPO of the starting sample, the pre-deformed sample, and of samples F052, F042, and F037, which were annealed for 4, 20, and 168 hours, respectively. Sample F052, annealed for 4 hours (Fig. 5.1b), contains large domains of grains that are comparable in size to the starting material (hereafter referred to as ‘matrix’). Within this matrix are embedded a small number of grains, each about an order of magnitude larger than matrix grains (hereafter referred to as ‘porphyroblasts’), which have grown rapidly at the expense of matrix grains. We distinguish the two groups using a threshold of 100 μm, with grains smaller than 100 μm defined as matrix, and grains larger than 100 μm defined as porphyroblasts. Sample F042, annealed for 20 hours (Fig. 5.1c), exhibits a similar bimodal grain-size distribution, but with a larger areal fraction of porphyroblasts. Sample F037, which was annealed for 168 hours (Fig. 5.1d), is almost entirely composed of large porphyroblasts (0.5–2mm), with only a few remnant matrix grains. Figure 5.2a displays the evolution of area fraction occupied by the matrix (blue line) and the porphyroblasts (red line).

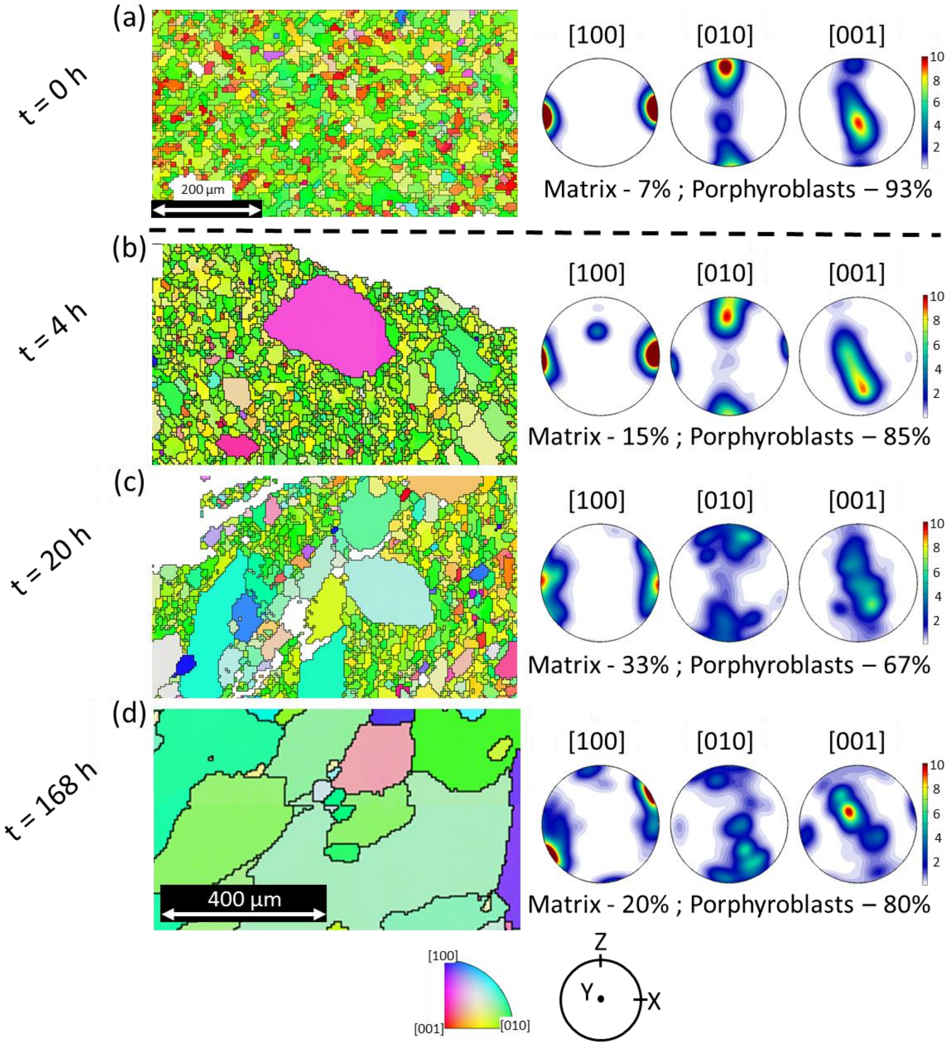

Figure 5.1 – Electron backscatter diffraction (EBSD) maps for (a) starting, pre-deformed sample, and samples annealed for (b) 4 hours, (c) 20 hours, and (d) 168 hours. Grain colors represent the orientation of the olivine crystal axes with respect to the normal to the shear plane (the Z-axis). Upper hemisphere pole figures show the associated crystallographic preferred orientation (CPO) of olivine where colors represent multiples of uniform distribution. Area fraction of matrix grains (d < 100 µm) and porphyroblasts (d > 100 µm) for each map is given in percentage beneath the corresponding pole figures.

Crystallographic data are presented as pole figures depicting the orientation of [100], [010] and [001] axes from each pixel in the original deformation reference frame (Fig. 5.1). The complete data set, in which each pixel is represented equally in the pole figures, is used to capture the relative importance of the larger grains when the grain-size distribution is bimodal. The starting CPO is a strong A-type with the [100] axis oriented parallel to the shear direction

(X-axis), indicative of grain rotations dominated by slip on the (010)[100] system. After 4 hours of annealing, there is some dispersion of the original CPO that corresponds to the addition of the orientations of the growing porphyroblasts (Fig. 5.1b). After 20 hours of annealing, the original CPO is still clearly evident, but with the addition of a new secondary [100] peak at a small angle to the shear direction (Fig. 5.1c). After 168 hours of annealing, the dominant peak in the [100] pole figure shifts to a new orientation that is ~10–15° from the shear direction; only a weak peak remains parallel to the X-axis. The porphyroblasts comprise more than 80% of the sample area and therefore dominate the overall texture (Fig. 5.1d).

Data are combined from the three annealing experiments to show how CPO of the matrix population compares to the porphyroblast population (Fig. 5.2). The matrix exhibits a simple orthorhombic CPO pattern (Fig. 5.2b) similar to the starting material (Fig. 5.1a). The porphyroblast CPO is more complex (Fig. 5.2c). It is characterized by peaks that are rotated ~10–15° from the matrix orientation, with some additional peaks oriented at a high angle (~100–110°) to the matrix CPO. The different groups of crystallographic orientations can be seen most clearly in the [100] pole figure. The primary point maximum is oriented at a 10–15° angle from the shear direction (within the X-Z plane). A secondary point maximum arises from a group of crystals with [100] axes oriented parallel to the shear direction, and are similar to the texture of the matrix. There is also a set of crystals with [100] axes oriented ~100–110° to the shear plane at a small angle to the Z-axis. The [010] pole figure contains grains oriented either in the original orientation, with [010] normal to the shear plane (parallel to Z), or rotated away from Z towards the Y-axis. The [001] pole figure exhibits a dominant point maximum parallel to the Y-axis with two additional prominent maxima 90° from each other on the X-Z plane.

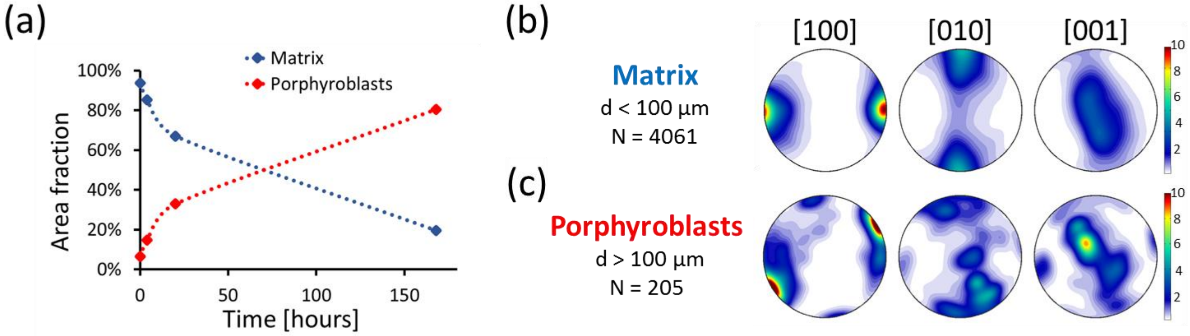

Figure 5.2 – (a) Evolution of area fraction comprised of matrix or porphyroblasts from the three annealing samples plotted against annealing time. (b) and (c) Combined crystallographic preferred orientations (CPOs) of (b) matrix grains and (c) porphyroblasts.

Figure 5.3 displays a single porphyroblast from sample F052 (marked by a red star) surrounded by matrix on three sides. The porphyroblast is characterized by generally straight boundaries that are cuspate in a few locations where the boundary is enveloped small relict matrix grains. In contrast, the matrix grains have bulging grain-boundaries that are similar to those observed in the starting material (Fig. 5.3a, c). The porphyroblast orientation is rotated 90° about the Y-axis from the matrix orientation, with [100] oriented normal to the original slip plane and the [010] axis oriented towards the shear direction (Fig. 5.3b). The porphyroblast has a mean apparent GND density of 5.2 x 10^{12} m^{-2}. This density is at the noise level of the measurement for the mapping step size used (Wallis et al., 2016) and therefore represents an upper bound on the GND density within the porphyroblast. In contrast, the matrix has a mean GND density of 5.7×10^{14} m^{-2}, which is at least two orders of magnitude greater than that of the porphyroblast and does not appear to be significantly modified by the annealing process. The boundaries between the porphyroblast and the matrix are typically high angle, with misorientation angles between 75 and 110°. In contrast, boundaries within the matrix, which still retains a strong texture, have an average misorientation angle of 30° with standard deviation of 16° (Fig. 5.3c). A compilation of the grain-boundary misorientations from all three samples exhibit a clear shift in the overall distribution from grain boundaries with low misorientation for matrix grains to grain boundaries with high misorientation for the porphyroblasts (Fig. 5.3d).

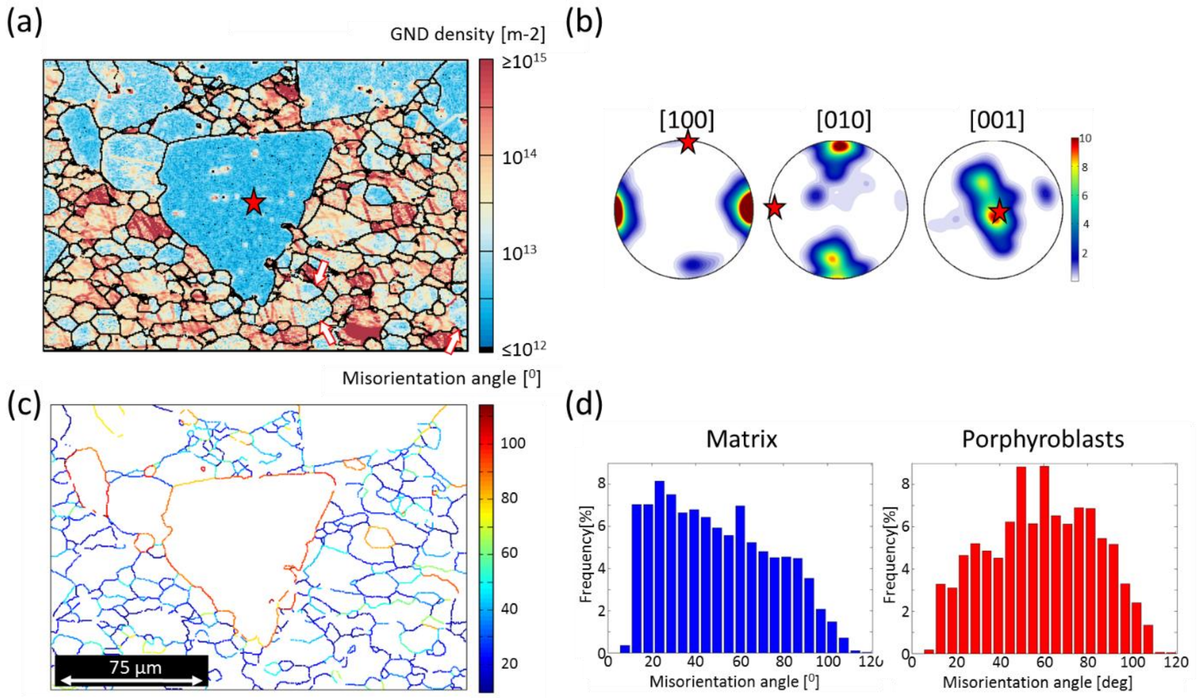

Figure 5.3 - (a) Densities of geometrically necessary dislocations (GNDs) estimated from high-angular resolution electron backscatter diffraction data. A notable porphyroblast is marked with a red star. Some elongate matrix grains with spatial variation in dislocation density, possibly representing the initial stage of primary grain boundary migration, are marked with white arrows. (b) CPO of the analyzed area excluding the porphyroblast, which is marked as a red star. (c) Map of the same area as (a) highlighting grain boundary misorientation angles (d) Distribution of grain boundary misorientation angles between the matrix and porphyroblast grains.

5.4 Discussion

5.4.1 *Interpretation of microstructural observations*

Static annealing of polycrystalline materials involves a variety of processes, including dislocation annihilation and grain growth, both of which decrease the total energy stored in the material. Studies of the kinetics of grain growth in synthetic olivine aggregates typically show evidence for grain growth in which the grain-size distribution remains narrow, with a log-normal distribution (Faul and Scott, 2006; Karato, 1989; Nichols and Mackwell, 1991). This type of grain growth is generally referred to as (spatially) continuous or ‘normal’, reflecting the continuous shift of unimodal grain-size distribution as the mean grain-size increase (e.g., Atkinson, 1988). However, in starting materials that are less homogeneous, grain growth may proceed by (spatially) discontinuous or ‘abnormal’ grain growth leading to a grain-size distribution that is highly bimodal (Hillert, 1965; Humphreys and Hatherly, 2004; Rollett et al., 1989). The noticeable microstructural evolution in our experiments, from an initially homogeneous microstructure with grain sizes around 30 μm and curved grain boundaries, to a microstructure that is dominated by grains that are 100–1000 μm in diameter with straight grain boundaries (Fig. 5.1 – 5.3), is typical of discontinuous grain-growth. Cooper and Kohlstedt (1984) have observed discontinuous grain growth in olivine aggregates comprises of 4 or 10 % basaltic melt and some initial larger grains. Although the driving forces for GBM in Cooper and Kohlstedt are differ compared with this study the intrinsic calculated mobilities are similar (for the grain-boundary mobility calculations see Appendix).

For grains to grow discontinuously at the expense of other grains, two conditions must be met: (1) before discontinuous growth commences, a small number of grains in the aggregate must be larger than other grains, by at least a factor of two (Hillert, 1965; Thompson et al., 1987), and (2) the kinetics of growth of the matrix (relict small grains) must be intrinsically slow or inhibited. In our experiments, the low dislocation-density of the porphyroblasts suggests that a small, selective group of grains with relatively low dislocation-density grew rapidly at the expense of neighboring grains with high dislocation-density during the initial stages of annealing. This primary stage of growth, driven by gradients in strain energy associated with the dislocation content, produced a set of grains that are roughly double the size of their neighbors, satisfying the first condition for discontinuous grain-growth. Figure 5.3a contains some examples of larger, elongate grains with gradients in dislocation density, which are interpreted to be examples of grains with boundaries that have migrated during the primary stage of recovery. For the second condition, a mechanism for inhibiting grain growth of matrix grains is needed. There are several mechanisms by which grain growth can be inhibited or slowed, including pinning of grain boundaries by secondary phases (Evans et al., 2001; Humphreys, 1997b; Rios, 1997), the presence of impurities at grain boundaries (Bhattacharyya et al., 2015; Powers and Glaeser, 1998; Skemer and Karato, 2007), and the presence of a strong CPO with a low mean surface energy (Abbruzzese and Lücke, 1986; Eichelkraut et al., 1988). Since sample PT0718 is monomineralic and synthetic, it is unlikely that secondary phases or impurities play a significant role in the inihibition of grain-boundary migration (GBM). Therefore we infer that strong CPO is the explanation for the inhibition of normal grain-growth in our experiments, which is consistant with theoretical predictions (Abbruzzese and Lücke, 1986; Eichelkraut et al., 1988; Humphreys, 1997a; Novikov and Novikov, 1997, p. 102 - 111; Rollett et al., 1989) and experimental observations (Kim et al., 2007; Mishin et al., 2010; Zahid et al., 2009).

5.4.2 CPO modification during static annealing - comparison with previous studies

The results presented here indicate that static annealing of olivine results in discontinuous grain growth and both weakens and rotates pre-existing CPO. Previous studies, spanning several geologic materials, that investigated the style of static grain growth and the degree to which the strength and orientation of CPO is modified came to varied conclusions. Heilbronner and Tullis (2002) performed post-deformation annealing experiments on quartzite samples. Annealing in their experiments resulted in an increase of the mean grain-size by a factor of 2–5 by continuous grain growth. The CPO preserved its orientation but decreased in strength. However, other studies on quartz have found that *c*-axis orientations may be modified during annealing by orientation-dependent growth, resulting in increased CPO strength (Green, 1967), or modification of the *c*-axis CPO from a dominant point maxima to a broader girdled circle in the direction of applied compression (Gleason and Tullis, 1990; Green II et al., 1970). Stöckhert and Duyster (1999) have documented a transient stage of discontinuous grain growth in quartz veins. The porphyroblasts in their study have a distinctly different CPO than the surrounding matrix grains. The authors postulate that the discontinuous grain growth was promoted by the pre-existing CPO of the matrix and the variation of the grain-boundary energy with misorientation angle (Stöckhert and Duyster, 1999). In ice, GBM was interpreted to weaken and even reset the CPO during grain-growth (Samyn et al., 2008; Wilson, 1982), and to produce a girdle of *c*-axis orientations with an angle to the compression axis during syn-deformational GBM (Montagnat et al., 2015). Additional grain growth experiments on calcite and rock-analogue materials such as octachloropropane have generally concluded that the post-annealing CPO may be weaker but is overall similar to the original CPO (Covey-Crump, 1997; Park et al., 2001). In summary, some studies conclude that during annealing the initial CPO is preserved, while others, show that the CPO can be modified in terms of its strength or/and its orientation.

5.4.3 Implications for CPO evolution and seismic anisotropy

It is well-documented that shear deformation of olivine typically leads to strengthening and rotation of CPO, which under a wide range of conditions will align the olivine [100] axes with the direction of flow (Kaminski and Ribe, 2001; Skemer et al., 2012; Wenk et al., 1991; Zhang and Karato, 1995). The process of aligning olivine grains is complex, however, as it reflects the competition between several deformation and recovery processes. Through deformation, the ‘primary’ CPO is aligned with the deformation kinematics while recovery processes, like dynamic recrystallization, are overcome by crystallographic rotation due to plastic deformation (Karato, 1987). Zhang et al., (2000) demonstrated that during deformation and associated dynamic recrystallization, a fraction of olivine grains with low dislocation-density and low Schmid factor tend to grow at the expense of adjacent grains with high dislocation-density and high Schmid factor. This fraction of grains with low dislocation density form a secondary peak in the [100] pole figure (Fig. 5.4a), which is also seen in many natural samples (e.g., Ben Ismaïl and Mainprice, 1998), and is interpreted to result from syn-deformational GBM (Kaminski and Ribe, 2001; Lee et al., 2002). Experimental studies to strains of 1.5 demonstrate that this secondary peak weakens with progressive deformation and the primary point maximum emerges parallel to the shear direction (Zhang and Karato, 1995).

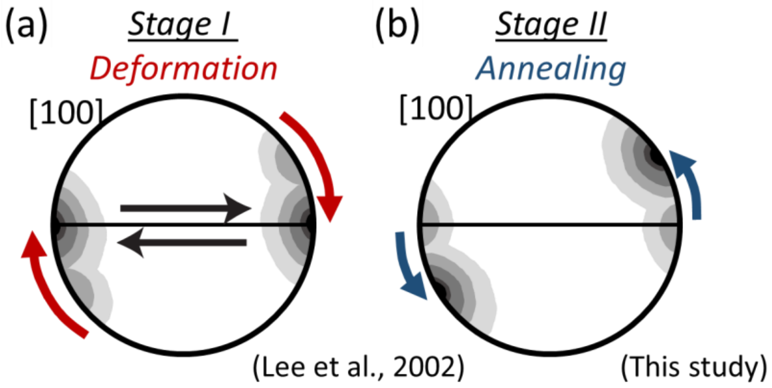

Figure 5.4 - Schematic illustration depicting the stages for olivine [100] CPO during (a) deformation and (b) subsequent annealing. (a) Stage I - During deformation, after sufficient strain, the dominant peak is aligned with the shear direction. A secondary peak on the plane of rotation is interpreted to result from syn-deformational grain-boundary migration (Lee et al., 2002; Zhang et al., 2000). (b) Stage II – During annealing subsequent to stage I, a reversal occurs in which the secondary peak, at an angle to the shear direction, becomes dominant on the expense of the original peak.

In our annealing experiments, we observe a reversal of the CPO evolution. Starting from the orientation of a typical olivine A-type fabric, we observe growth of grains that are misoriented with respect to the original CPO (Fig. 5.4b). This produces a secondary peak in the [100] pole figure that strengthens with annealing time (Fig. 5.1 and 5.4). At some point between 20 and 168 hours, this secondary, oblique peak becomes dominant (Fig. 5.1 and 5.4), modifying the associated seismological signature (Figure 5.5).

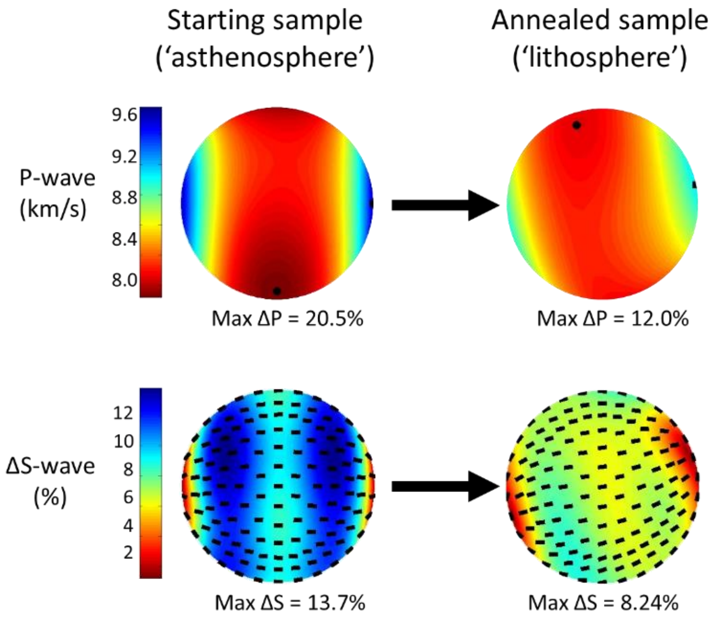

Figure 5.5 – Modification of the anisotropic signature of seismic waves due to static annealing of an olivine polycrystal with pre-existing CPO. Pole figures show the orientation distributions of P-wave velocities (top) and the magnitudes and polarization directions of S-waves (bottom). The deformed starting sample, PT0178, is analogous to deformed asthenosphere with a strong A-type CPO. The CPO of porphyrobstast grains (i.e., Figure 5.2c) is analogous to a lithospheric layer after cooling and the cessation of deformation at asthenospheric temperatures. Pole figures were calculated using MSAT (Walker and Wookey, 2012) using elastic constants for olivine from Abramson et al. (1997).

While CPO in the asthenosphere potentially records the composite signature of both previous and current deformation events (e.g., Chastel et al., 1993), CPO in the lithosphere is often interpreted to record past deformation events and remain unmodified by ongoing deformation in the underlying asthenosphere (Deschamps et al., 2008). This 'frozen' or 'fossil' texture, can significantly affect the overall seismic signature of the upper mantle (e.g., Savage, 1999). However, it is unclear whether seismic anisotropy generated in the lithosphere truly reflects CPO introduced near mid-ocean ridges, or if additional modification has occurred. In this study, we have demonstrated that CPO may continue to evolve under static conditions due to preferential growth of grains in particular orientations. Figure 5.5 reveals the consequences of microstructural evolution during annealing on P-wave velocities and anisotropy of S-wave velocities. In a dunite with the CPO of the deformed sample PT0718, P-wave anisotropy is approximately 20%. In contrast, in dunite with the CPO of the porphyroblast grains (Figure 5.2c), P-waves would exhibit anisotropy of only 12%. S-wave anisotropy is similarly reduced, from 13.7% to 8.2%. Moreover, the orientation of the fast directions is rotated by 10-15 degrees. These changes in the orientation distributions and magnitudes of seismic anisotropy offer an explanation for the general global trend of greater seismic anisotropy in the asthenosphere compared with the lithosphere (Beghein et al., 2014; Burgos et al., 2014).

5.5 Conclusions

CPO forms during creep by dislocation-mediated deformation mechanisms, and relationships between seismic anisotropy, CPO, and kinematics, are often used to infer flow patterns in the upper mantle (e.g., Karato et al., 2008; Skemer and Hansen, 2016b). However, recent studies have shown that CPO doesn’t necessarily record only the ongoing deformation but may retain a record of, or be otherwise influenced by, former deformation episodes (Blackman et al., 2002; Boneh et al., 2015; Boneh and Skemer, 2014; Hansen et al., 2014). Discontinuous grain-growth, which occurs readily during high-temperature annealing of textured olivine samples leads to significant modification of the CPO. This implies that CPO, and hence seismic anisotropy, will continue to evolve, even during periods of tectonic quiescence. These observations challenge the view that CPO in the lithosphere is frozen and generally remains unchanged. Interpretation of seismic anisotropy generated in the lithosphere must consider that CPO formed under asthenospheric temperatures and incorporated into the lithosphere may have weakened and rotated with time.

Appendix

Mobility is a fundamental property of grain boundaries and may be used to model grain-growth and other processes. To estimate the mobility of the large olivine grain boundary in Figure 5.3 we use the following relation for the velocity of a moving interface (V)

$$V = MF \qquad (5.1A)$$

where M is the grain boundary mobility, which has an Arrhenius form ($M = M_0 e^{-E/RT}$), and F is the driving force per unit area. We assume the driving force for grain boundary migration results from both the difference in grain boundary energy and the difference in strain energy between the abnormally growing grain and the matrix. The driving force per unit area due to grain boundary energy is expressed as:

$$F_b = 3\gamma/d\,, \qquad (5.2A)$$

where γ is the grain-boundary energy (~0.9 J/m^2 for olivine; Cooper and Kohlstedt, 1982), and d is the diameter of the matrix grains. The driving force per unit area due to strain energy is given by:

$$F_s = \mu b^2(\Delta\rho)\,, \qquad (5.3A)$$

where μ is the shear modulus, b is the length of the Burgers vector, and $\Delta\rho$ is the difference in dislocation-density across the boundary of interest. We sum the driving forces due to the grain-boundary and strain energies ($F = F_b + F_s$). Using equations 5.2A and 5.3A, and μ = 50 GPa and b = 0.6 nm, we calculate the grain boundary surface energy to be $2.5 \times 10^5\ [\frac{N}{m^2}]$, the strain energy to be $1.0{\times}10^7\ \left[\frac{N}{m^2}\right]$. The grain boundary velocity is assumed to be constant through the duration of the experiment:

$$V = \frac{d_p - d}{dt} \qquad (5.4A)$$

where d_p is the final diameter of the porphyroblast highlighted in Figure 5.3, d is the mean diameter of the matrix grains, and *dt* is the duration of the experiment during which temperature was at its maximum. V is calculated to be 6.9×10^{-9} m/s. From equation 1 grain-boundary mobility is calculated to be $M_b = 6.6 \times 10^{-16}\ [\frac{\mathrm{m}^3}{\mathrm{N\ s}}]$ at the experimental temperature of 1250° C. This value can be compared with grain boundary mobility for Fo_{92} olivine determined by Cooper and Kohlstedt (1984), who calculate $M_b = 1.6 \times 10^{-15}\ [\frac{\mathrm{m}^3}{\mathrm{N\ s}}]$ and $M_b = 2.3 \times 10^{-15}\ [\frac{\mathrm{m}^3}{\mathrm{N\ s}}]$, at T = 1300 and 1400° C respectively.

Chapter 6: Conclusions and future work

Olivine, the most abundant mineral in the upper mantle, is seismically anisotropic and often used to infer the kinematics of mantle flow. Here we have demonstrated that the integrated deformation history of the mantle can affect olivine CPO and the associated seismic anisotropy. For variety of deformation paths, olivine CPO can evolve differently and exhibit protracted transient textural transitions. In addition, CPO can be modified under conditions of static annealing due to a microstructural change.

The rate at which olivine crystals become aligned with progressive deformation, or the preservation of existing crystallographic alignment is critical to the interpretation of seismic anisotropy. However, the non-unique relations between CPO and deformation history events are problematic when interpreting seismic anisotropy in the mantle or when interpreting the texture of exhumed mantle in terms of deformation events.

I have demonstrated here the effects of a pre-existing texture on the evolution of olivine CPO under both dynamic or static conditions. It is important to mention that the texture evolution, either by a change of the deformation tensor or by static annealing, is not arbitrary. There are systematic paths by which texture may evolve with respect to the deformation history. The different evolutionary pathways may be related to: (a) the current deformation regime, (b) the pre-existing texture symmetry, (c) texture orientation, and (d) texture strength. This work suggests that future work on the characterization of possible CPO evolution paths for different mantle scenarios is necessary in order to account for the effect of deformation history on seismic anisotropy.

In addition, we have only considered here deformation of olivine under dry conditions with relatively low-medium stress and a dominant [100](010) slip system, commonly referred to as ‘A-type’. There are 5 possible olivine types (A-E), which vary with deformation conditions and water content (e.g., Karato et al., 2008). The textural transition that was investigated here is a result of changes of the deformation tensor, but with no change in the dominant slip systems. However, when deformation conditions change, a change of texture may be expected due to changes in olivine’s slip system activity. Such a textural transition has not been studied extensively and further exploration is required.

References

Abbruzzese, G., Lücke, K., 1986. A theory of texture controlled grain growth—I. Derivation and general discussion of the model. Acta Metallurgica 34, 905-914.

Abramson, E.H., Brown, M., Slutsky, L.J., Zaug, J., 1997. The elastic constants of San Carlos olivine up to 17 GPa. J. Geophys. Res. 102, 12,252-212,263.

Alpert, L. A., Miller M. S., Becker T. W., and Allam A. A., 2013, Structure beneath the Alboran from geodynamic flow models and seismic anisotropy, Journal of Geophysical Research: Solid Earth, 118(8), 4265-4277.

Antonangeli, D., Occelli, F., Requardt, H., Badro, J., Fiquet, G., Krisch, M., 2004. Elastic anisotropy in textured hcp-iron to 112 GPa from sound wave propagation measurements. Earth and Planetary Science Letters 225, 243-251.

Atkinson, H., 1988. Overview no. 65: Theories of normal grain growth in pure single phase systems. Acta Metallurgica 36, 469-491.

Ave Lallemant, H., 1975. Mechanisms of preferred orientations of olivine in tectonite peridotite. Geology 3, 653.

Ave'lallemant, H.G., Carter, N.L., 1970. Syntectonic recrystallization of olivine and modes of flow in the upper mantle. Geological Society of America Bulletin 81, 2203-2220.

Bachmann, F., Hielscher R., and Schaeben H., 2010, Texture analysis with MTEX–free and open source software toolbox, Solid State Phenomena, 160, 63-68.

Bai, Q., Mackwell S. J., and Kohlstedt D. L., 1991, High-temperature creep of olivine single crystals 1. Mechanical results for buffered samples, J. Geophys. Res., 96(B2), 2441-2463.

Barruol, G., Helffrich, G., Vauchez, A., 1997. Shear wave splitting around the northern Atlantic: frozen Pangaean lithospheric anisotropy? Tectonophysics 279, 135-148.

Becker, T. W., Conrad C. P., Schaeffer A. J., and Lebedev S., 2014, Origin of azimuthal seismic anisotropy in oceanic plates and mantle, Earth Planet. Sci. Lett., 401, 236-250.

Becker, T. W., Chevrot S., Schulte-Pelkum V., and Blackman D. K., 2006a, Statistical properties of seismic anisotropy predicted by upper mantle geodynamic models, Journal of Geophysical Research: Solid Earth (1978–2012), 111(B8).

Becker, T. W., Schulte-Pelkum V., Blackman D. K., Kellogg J. B., and O'Connell R. J., 2006b, Mantle flow under the western United States from shear wave splitting, Earth Planet. Sci. Lett., 247(3–4), 235-251.

Becker, T.W., Kellogg, J.B., Ekström, G., O'Connell, R.J., 2003. Comparison of azimuthal seismic anisotropy from surface waves and finite strain from global mantle-circulation models. Geophysical Journal International 155, 696-714.

Beghein, C., Yuan, K., Schmerr, N., Xing, Z., 2014. Changes in seismic anisotropy shed light on the nature of the Gutenberg discontinuity. Science 343, 1237-1240.

Bell, D.R., Rossman, G.R., Maldener, J., Endisch, D., Rauch, F., 2003. Hydroxide in olivine: A quantitative determination of the absolute amount and calibration of the IR spectrum. Journal of Geophysical Research: Solid Earth (1978–2012) 108.

Ben Ismaïl, W., Mainprice, D., 1998. An olivine fabric database: an overview of upper mantle fabrics and seismic anisotropy. Tectonophysics 296, 145-157.

Berckhemer, H., Kampfmann, W., Aulbach, E., Schmeling, H., 1982. Shear modulus and< i> Q</i> of forsterite and dunite near partial melting from forced-oscillation experiments. Phys. Earth Planet. Inter. 29, 30-41.

Bestmann, M., Kunze, K., Matthews, A., 2000. Evolution of a calcite marble shear zone complex on Thassos Island, Greece: microstructural and textural fabrics and their kinematic significance. Journal of Structural Geology 22, 1789-1807.

Bhattacharyya, J., Agnew, S., Muralidharan, G., 2015. Texture enhancement during grain growth of magnesium alloy AZ31B. Acta Materialia 86, 80-94.

Blackman, D., 2007, Use of mineral physics, with geodynamic modelling and seismology, to investigate flow in the Earth's mantle, Reports on Progress in Physics, 70(5), 659.

Blackman, D. K., and Kendall J. M., 2002, Seismic anisotropy in the upper mantle 2. Predictions for current plate boundary flow models, Geochemistry, Geophysics, Geosystems, 3(9), 8602.

Blackman, D. K., Kendall J., Dawson P. R., Wenk H., Boyce D., and Morgan J. P., 1996, Teleseismic imaging of subaxial flow at mid-ocean ridges: traveltime effects of anisotropic mineral texture in the mantle, Geophysical Journal International, 127(2), 415-426.

Blackman, D. K., Wenk H., Kendall J. M., 2002. Seismic anisotropy of the upper mantle 1. Factors that affect mineral texture and effective elastic properties. Geochemistry, Geophysics, Geosystems 3, 1-24.

Boneh, Y., Morales, L.F., Kaminski, E., Skemer, P., 2015. Modeling olivine CPO evolution with complex deformation histories: Implications for the interpretation of seismic anisotropy in the mantle. Geochemistry, Geophysics, Geosystems 16, 3436-3455.

Boneh, Y., Skemer, P., 2014. The effect of deformation history on the evolution of olivine CPO. Earth and Planetary Science Letters 406, 213-222.

Bonnin, M., Tommasi A., Hassani R., Chevrot S., Wookey J., and Barruol G., 2012, Numerical modelling of the upper-mantle anisotropy beneath a migrating strike-slip plate boundary: the San Andreas Fault system, Geophysical Journal International, 191(2), 436-458.

Boullier, A.M., Nicolas, A., 1975. Classification of textures and fabrics of peridotite xenoliths from South African kimberlites. Physics and Chemistry of the Earth 9, 467IN7469-468475.

Bunge, H.-J., 2013. Texture analysis in materials science: mathematical methods. Elsevier.

Burgos, G., Montagner, J.P., Beucler, E., Capdeville, Y., Mocquet, A., Drilleau, M., 2014. Oceanic lithosphere-asthenosphere boundary from surface wave dispersion data. Journal of Geophysical Research: Solid Earth 119, 1079-1093.

Bystricky, M., Kunze, K., Burlini, L., Burg, J.-P., 2000. High shear strain of olivine aggregates: rheological and seismic consequences. Science 290, 1564-1567.

Castañeda, P. P., 2002, Second-order homogenization estimates for nonlinear composites incorporating field fluctuations: I—theory, Journal of the Mechanics and Physics of Solids, 50(4), 737-757.

Castelnau, O., Blackman, D., Becker, T., 2009. Numerical simulations of texture development and associated rheological anisotropy in regions of complex mantle flow. Geophysical Research Letters 36, L12304.

Castelnau, O., Brenner, R., Lebensohn, R., 2006. The effect of strain heterogeneity on the work hardening of polycrystals predicted by mean-field approaches. Acta materialia 54, 2745-2756.

Castelnau, O., Blackman D., Lebensohn R., and Ponte Castañeda P., 2008, Micromechanical modeling of the viscoplastic behavior of olivine, Journal of Geophysical Research: Solid Earth (1978–2012), 113(B9).

Castelnau, O., Cordier P., Lebensohn R., Merkel S., and Raterron P., 2010, Microstructures and rheology of the Earth's upper mantle inferred from a multiscale approach, Comptes Rendus Physique, 11(3), 304-315.

Chastel, Y.B., Dawson, P.R., Wenk, H.R., Bennett, K., 1993. Anisotropic convection with implications for the upper mantle. Journal of Geophysical Research: Solid Earth (1978–2012) 98, 17757-17771.

Chopra, P.N., Paterson, M.S., 1981. The Experimental Deformation of Dunite. Tectonophysics 78, 453-473.

Chopra, P.N., Paterson, M.S., 1984. The role of water in the deformation of dunite. J Geophys Res Solid Earth 89, 7861-7876.

Christensen, N.I., 1984. The magnitude, symmetry and origin of upper mantle anisotropy based on fabric analyses of ultramafic tectonites. Geophysical Journal International 76, 89-111.

Conder, J. A., and Wiens D. A., 2007, Rapid mantle flow beneath the Tonga volcanic arc, Earth Planet. Sci. Lett., 264(1), 299-307.

Conrad, C.P., Behn, M.D., Silver, P.G., 2007. Global mantle flow and the development of seismic anisotropy: Differences between the oceanic and continental upper mantle. J. Geophys. Res. 112, B07317.

Couvy, H., Frost, D.J., Heidelbach, F., Nyilas, K., Ungár, T., Mackwell, S.J., Cordier, P., 2004. Shear deformation experiments of forsterite at 11 GPa-1400°C in the multianvil apparatus. Eur. J. Miner. 16, 877-889.

Covey-Crump, S., 1997. The high temperature static recovery and recrystallization behaviour of cold-worked Carrara marble. Journal of Structural Geology 19, 225-241.

Dawson, P.R., Wenk, H.-R., 2000. Texturing of the upper mantle during convection. Philosophical Magazine A 80, 573-598.

Dempsey, E.D., Prior, D.J., Mariani, E., Toy, V.G., Tatham, D.J., 2011. Mica-controlled anisotropy within mid-to-upper crustal mylonites: an EBSD study of mica fabrics in the Alpine Fault Zone, New Zealand. Geological Society, London, Special Publications 360, 33-47.

Deschamps, F., Lebedev, S., Meier, T., Trampert, J., 2008. Stratified seismic anisotropy reveals past and present deformation beneath the East-central United States. Earth and Planetary Science Letters 274, 489-498.

Detrez, F., Castelnau O., Cordier P., Merkel S., and Raterron P., 2015, Effective viscoplastic behavior of polycrystalline aggregates lacking four independent slip systems inferred from homogenization methods; application to olivine, Journal of the Mechanics and Physics of Solids, 83, 199-220.

Di Leo, J., Walker, A., Li, Z.H., Wookey, J., Ribe, N., Kendall, J.M., Tommasi, A., 2014. Development of texture and seismic anisotropy during the onset of subduction. Geochemistry, Geophysics, Geosystems.

Druiventak, A., Trepmann, C.A., Renner, J., Hanke, K., 2011. Low-temperature plasticity of olivine during high stress deformation of peridotite at lithospheric conditions—An experimental study. Earth Planet. Sci. Lett. 311, 199-211.

Druken, K., Kincaid C., and Griffiths R., 2013, Directions of seismic anisotropy in laboratory models of mantle plumes, Geophysical Research Letters, 40(14), 3544-3549.

Druken, K., Long M., and Kincaid C., 2011, Patterns in seismic anisotropy driven by rollback subduction beneath the High Lava Plains, Geophysical Research Letters, 38(13).

Durham, W. B., and Goetze C., 1977, Plastic flow of oriented single crystals of olivine 1. Mechanical data, J. Geophys. Res., 82(36), 5737-5753.

Dziewonski, A.M., Anderson, D.L., 1981. Preliminary reference Earth model. Physics of the Earth and Planetary Interiors 25, 297-356.

Eichelkraut, H., Abbruzzese, G., Lücke, K., 1988. A theory of texture controlled grain growth—II. Numerical and analytical treatment of grain growth in the presence of two texture components. Acta Metallurgica 36, 55-68.

El-Dasher, B., Adams, B., Rollett, A., 2003. Viewpoint: experimental recovery of geometrically necessary dislocation density in polycrystals. Scripta materialia 48, 141-145.

Eshelby, J. D., 1957, The determination of the elastic field of an ellipsoidal inclusion, and related problems, paper presented at Proceedings of the Royal Society of London A: Mathematical, Physical and Engineering Sciences, The Royal Society.

Evans, B., Renner, J., Hirth, G., 2001. A few remarks on the kinetics of static grain growth in rocks. International Journal of Earth Sciences 90, 88-103.

Faccenda, M., and Capitanio F., 2013, Seismic anisotropy around subduction zones: Insights from three-dimensional modeling of upper mantle deformation and SKS splitting calculations, Geochemistry, Geophysics, Geosystems, 14(1), 243-262.

Faccenda, M., Capitanio, F., 2012. Development of mantle seismic anisotropy during subduction-induced 3-D flow. Geophysical Research Letters 39.

Falus, G., Tommasi A., and Soustelle V., 2011, The effect of dynamic recrystallization on olivine crystal preferred orientations in mantle xenoliths deformed under varied stress conditions, Journal of Structural Geology, 33(11), 1528-1540.

Faul, U.H., Scott, D., 2006. Grain growth in partially molten olivine aggregates. Contributions to Mineralogy and Petrology 151, 101-111.

Fliervoet, T.F., Drury, M.R., Chopra, P.N., 1999. Crystallographic preferred orientations and misorientations in some olivine rocks deformed by diffusion or dislocation creep. Tectonophysics 303, 1-27.

Gleason, G., Tullis, J., 1990. The effect of annealing on the lattice preferred orientations of deformed quartz aggregates. EOS, Transactions of the American Geophysical Union 71, 1657.

Green II, H., Griggs, D., Christie, J., 1970. Syntectonic and annealing recrystallization of fine-grained quartz aggregates, Experimental and Natural Rock Deformation/Experimentelle und natürliche Gesteinsverformung. Springer, pp. 272-335.

Green, H., 1967. Quartz: extreme preferred orientation produced by annealing. Science 157, 1444-1447.

Hansen, L.N., Warren, J.M., 2015. Quantifying the effect of pyroxene on deformation of peridotite in a natural shear zone. Journal of Geophysical Research: Solid Earth 120, 2717-2738.

Hansen, L.N., Warren, J.M., Zimmerman, M.E., Kohlstedt, D.L., 2016a. Viscous anisotropy of textured olivine aggregates, Part 1: Measurement of the magnitude and evolution of anisotropy. Earth and Planetary Science Letters 445, 92-103.

Hansen, L.N., Conrad, C.P., Boneh, Y., Skemer, P., Warren, J.M. and Kohlstedt, D.L., 2016b. Viscous anisotropy of textured olivine aggregates: 2. Micromechanical model. Journal of Geophysical Research: Solid Earth, 121(10), pp.7137-7160.

Hansen, L.N., Zhao, Y.-H., Zimmerman, M.E., Kohlstedt, D.L., 2014. Protracted fabric evolution in olivine: Implications for the relationship among strain, crystallographic fabric, and seismic anisotropy. Earth Planet. Sci. Lett. 387, 157-168.

Hansen, L.N., Zimmerman, M.E., Kohlstedt, D.L., 2012a. Laboratory measurements of the viscous anisotropy of olivine aggregates. Nature 492, 415-418.

Hansen, L., Zimmerman, M., Kohlstedt, D., 2012b. The influence of microstructure on deformation of olivine in the grain-boundary sliding regime. Journal of Geophysical Research: Solid Earth 117.

Hedjazian, N., and Kaminski E., ,2014, Defining a proxy for the interpretation of seismic anisotropy in non-Newtonian mantle flows, Geophysical Research Letters, 41(20), 7065-7072.

Hess, H., 1964. Seismic anisotropy of the uppermost mantle under oceans.

Higgie, K., and Tommasi A., 2012, Feedbacks between deformation and melt distribution in the crust–mantle transition zone of the Oman ophiolite, Earth Planet. Sci. Lett., 359, 61-72.

Hillert, M., 1965. On the theory of normal and abnormal grain growth. Acta metallurgica 13, 227-238.

Hirth, G., Kohlstedt, D., 2003. Rheology of the upper mantle and the mantle wedge: A view from the experimentalists. Geophysical Monograph Series 138, 83-105.

Humphreys, F., 1997a. A unified theory of recovery, recrystallization and grain growth, based on the stability and growth of cellular microstructures—I. The basic model. Acta Materialia 45, 4231-4240.

Humphreys, F., 1997b. A unified theory of recovery, recrystallization and grain growth, based on the stability and growth of cellular microstructures—II. The effect of second-phase particles. Acta materialia 45, 5031-5039.

Humphreys, F.J., Hatherly, M., 2004. Recrystallization and Related Annealing Phenomena. Pergamon, Amsterdam.

Jackson, I., Paterson, M., Fitz Gerald, J., 1992. Seismic wave dispersion and attenuation in Åheim dunite: an experimental study. Geophysical Journal International 108, 517-534.

Jadamec, M., Billen, M., 2012. The role of rheology and slab shape on rapid mantle flow: Three-dimensional numerical models of the Alaska slab edge. Journal of Geophysical Research: Solid Earth (1978–2012) 117.

Jiang, Z., Prior, D.J., Wheeler, J., 2000. Albite crystallographic preferred orientation and grain misorientation distribution in a low-grade mylonite: implications for granular flow. Journal of Structural Geology 22, 1663-1674.

Jin, Z., Bai, Q., Kohlstedt, D., 1994. High-temperature creep of olivine crystals from four localities. Phys. Earth Planet. Inter. 82, 55-64.

Jung, H., Karato, S.-i., 2001. Water-induced fabric transitions in olivine. Science 293, 1460-1463.

Jung, H., Katayama, I., Jiang, Z., Hiraga, T., Karato, S., 2006. Effect of water and stress on the lattice-preferred orientation of olivine. Tectonophysics 421, 1-22.

Jung, H., Mo, W., Green, H.W., 2009. Upper mantle seismic anisotropy resulting from pressure-induced slip transition in olivine. Nature Geoscience 2, 73-77.

Kaminski, É., and Ribe N. M., 2002, Timescales for the evolution of seismic anisotropy in mantle flow, Geochemistry, Geophysics, Geosystems, 3(8), 1-17.

Kaminski, É., Ribe, N.M., 2001. A kinematic model for recrystallization and texture development in olivine polycrystals. Earth and Planetary Science Letters 189, 253-267.

Kaminski, E., Ribe, N.M., Browaeys, J.T., 2004. D-Rex, a program for calculation of seismic anisotropy due to crystal lattice preferred orientation in the convective upper mantle. Geophysical Journal International 158, 744-752.

Karato, S., 1989. Grain growth kinetics in olivine aggregates. Tectonophysics 168, 255-273.

Karato, S., Paterson M. S., and FitzGerald J. D., 1986, Rheology of synthetic olivine aggregates: influence of grain size and water, J. Geophys. Res., 91, 8151-8176.

Karato, S.I., 1987. Seismic anisotropy due to lattice preferred orientation of minerals: kinematic or dynamic? High-Pressure Research in Mineral Physics: A Volume in Honor of Syun-iti Akimoto, 455-471.

Karato, S.-i., 1988. The role of recrystallization in the preferred orientation of olivine. Phys. Earth Planet. Inter. 51, 107-122.

Karato, S.-i., Jung, H., Katayama, I., Skemer, P., 2008. Geodynamic significance of seismic anisotropy of the upper mantle: new insights from laboratory studies. Annu. Rev. Earth Planet. Sci. 36, 59-95.

Karato, S.-i., Wu, P., 1993. Rheology of the upper mantle: A synthesis, Science, pp. 771-778.

Katayama, I., Karato, S.-i., 2006. Effect of temperature on the B-to C-type olivine fabric transition and implication for flow pattern in subduction zones. Phys. Earth Planet. Inter. 157, 33-45.

Keefner, J. W., Mackwell S. J., Kohlstedt D. L., and Heidelbach F., 2011, Dependence of dislocation creep of dunite on oxygen fugacity: Implications for viscosity variations in Earth's mantle, Journal of Geophysical Research: Solid Earth, 116(B5), B05201.

Keefner, J., Mackwell, S., Kohlstedt, D., 2005. Dunite viscosity dependence on oxygen fugacity, 36th Annual Lunar and Planetary Science Conference, p. 1915.

Kern, H., Wenk, H.-R., 1983. Calcite texture development in experimentally induced ductile shear zones. Contributions to Mineralogy and Petrology 83, 231-236.

Kim, H.-C., Kang, C.-G., Huh, M.-Y., Engler, O., 2007. Effect of primary recrystallization texture on abnormal grain growth in an aluminum alloy. Scripta materialia 57, 325-327.

Kneller, E. A., and van Keken P. E., 2007, Trench-parallel flow and seismic anisotropy in the Mariana and Andean subduction systems, Nature, 450(7173), 1222-1225.

Knoll, M., Tommasi A., Logé R. E., and Signorelli J. W., 2009, A multiscale approach to model the anisotropic deformation of lithospheric plates, Geochemistry, Geophysics, Geosystems, 10(8).

Lassak, T. M., Fouch M. J., Hall C. E., and Kaminski É., 2006, Seismic characterization of mantle flow in subduction systems: Can we resolve a hydrated mantle wedge?, Earth Planet. Sci. Lett., 243(3), 632-649.

Law, R., Schmid, S., Wheeler, J., 1990. Simple shear deformation and quartz crystallographic fabrics: a possible natural example from the Torridon area of NW Scotland. Journal of Structural Geology 12, 29-45.

Lebensohn, R., and Tomé C., 1993, A self-consistent anisotropic approach for the simulation of plastic deformation and texture development of polycrystals: application to zirconium alloys, Acta Metallurgica et Materialia, 41(9), 2611-2624.

Lee, K.-H., Jian, Z., Karato, S.-i., 2002. A scanning electron micropscope study of the effects of dynamic recrystallisation on lattice preferred orientation in olivine. Tectonophysics 351, 331-341.

Leo, J.F., Walker, A.M., Li, Z.H., Wookey, J., Ribe, N.M., Kendall, J.M., Tommasi, A., 2014. Development of texture and seismic anisotropy during the onset of subduction. Geochemistry, Geophysics, Geosystems 15, 192-212.

Lev, E., Hager, B.H., 2008. Prediction of anisotropy from flow models: A comparison of three methods. Geochemistry, Geophysics, Geosystems 9.

Li, Z.H., Di Leo, J.F., Ribe, N.M., 2014. Subduction-induced mantle flow, finite strain and seismic anisotropy: Numerical modeling. Journal of Geophysical Research: Solid Earth.

Lin, P.-Y.P., Gaherty, J.B., Jin, G., Collins, J.A., Lizarralde, D., Evans, R.L., Hirth, G., 2016. High-resolution seismic constraints on flow dynamics in the oceanic asthenosphere. Nature.

Lloyd, G., Law, R., Mainprice, D., Wheeler, J., 1992. Microstructural and crystal fabric evolution during shear zone formation. Journal of Structural Geology 14, 1079-1100.

Long, M.D., Becker, T.W., 2010. Mantle dynamics and seismic anisotropy. Earth Planet. Sci. Lett. 297, 341-354.

Long, M.D., Silver, P.G., 2008. The subduction zone flow field from seismic anisotropy: A global view. Science 319, 315-318.

Long, M.D., Silver, P.G., 2009. Mantle flow in subduction systems: The subslab flow field and implications for mantle dynamics. Journal of Geophysical Research: Solid Earth (1978–2012) 114.

Mackwell, S.J., Kohlstedt, D.L., 1990. Diffusion of hydrogen in olivine: implications for water in the mantle. Journal of Geophysical Research: Solid Earth (1978–2012) 95, 5079-5088.

Mainprice, D., 1990. A fortran program to calculate seismic anisotropy from the lattice preferred orientation of minerals. Computers and Geosciences 16, 385-393.

Mainprice, D., 2007. Seismic anisotropy of the deep Earth from a mineral and rock physics perspective. Treatese of Geophysics, vol. 2, 437-491.

Mainprice, D., 2015. 2.20 - Seismic Anisotropy of the Deep Earth from a Mineral and Rock Physics Perspective, in: Schubert, G. (Ed.), Treatise on Geophysics (Second Edition). Elsevier, Oxford, pp. 487-538.

Mainprice, D., Bachmann, F., Hielscher, R., Schaeben, H., 2014. Descriptive tools for the analysis of texture projects with large datasets using MTEX: strength, symmetry and components. Geological Society, London, Special Publications 409, SP409. 408.

Mainprice, D., Barruol, G., Ben Ismaïl, W., 2000. The seismic anisotropy of the Earth's Mantle: From single crystal to polycrystal, in: Karato, S.-i., Forte, A.M., Liebermann, R.C., Master, G., Stixrude, L. (Eds.), Earth's deep interior: Mineral physics and tomography from the atomic to the global scale. American Geophysical Union, Waschington, D.C., pp. 237-264.

Mainprice, D., Hielscher R., and Schaeben H., 2011, Calculating anisotropic physical properties from texture data using the MTEX open-source package, Geological Society, London, Special Publications, 360(1), 175-192.

Mao, H.-k., Shu, J., Shen, G., Hemley, R.J., Li, B., Singh, A.K., 1998. Elasticity and rheology of iron above 220 GPa and the nature of the Earth's inner core. Nature 396, 741-743.

McKenzie, D., 1979. Finite deformation during fluid flow. Geophysical Journal of the Royal Astronomical Society 58, 689-715.

Mendelson, M.I., 1969. Average grain size in polycrystalline ceramics. Journal of the American Ceramic Society 52, 443-446.

Merkel, S., McNamara, A.K., Kubo, A., Speziale, S., Miyagi, L., Meng, Y., Duffy, T.S., Wenk, H.-R., 2007. Deformation of (Mg, Fe) SiO3 post-perovskite and D"anisotropy. Science 316, 1729-1732.

Michibayashi, K., Mainprice, D., 2004. The role of pre-existing mechanical anisotropy on shear zone development within oceanic mantle lithosphere: an example from the Oman ophiolite. Journal of Petrology 45, 405-414.

Mishin, O., Jensen, D.J., Hansen, N., 2010. Evolution of microstructure and texture during annealing of aluminum AA1050 cold rolled to high and ultrahigh strains. Metallurgical and Materials Transactions A 41, 2936-2948.

Miyagi, L., Kanitpanyacharoen, W., Kaercher, P., Lee, K.K., Wenk, H.-R., 2010. Slip systems in MgSiO3 post-perovskite: implications for D″ anisotropy. Science 329, 1639-1641.

Molinari, A., Canova G. R., and Azhy S., 1987, A self-consistent approach of the large deformation crystal polycrystal viscoplasticity, Acta Metall., 35, 2983-2994.

Montagnat, M., Chauve, T., Barou, F., Tommasi, A., Beausir, B., Fressengeas, C., 2015. Analysis of dynamic recrystallization of ice from EBSD orientation mapping. Frontiers in Earth Science 3.

Montagner, J.-P., 2002. Upper mantle low anisotropy channels below the Pacific Plate. Earth Planet. Sci. Lett. 202, 263-274.

Montagner, J.-P., Tanimoto, T., 1991. Global upper mantle tomography of seismic velocities and anisotropies. J. Geophys. Res. 96, 20337-20320,20351.

Montési, L.G., 2013. Fabric development as the key for forming ductile shear zones and enabling plate tectonics. Journal of Structural Geology.

Morales, L. F. G., and Tommasi A., 2011, Composition, textures, seismic and thermal anisotropies of xenoliths from a thin and hot lithospheric mantle (Summit Lake, southern Canadian Cordillera), Tectonophysics, 507(1), 1-15.

Nichols, S.J., Mackwell, S.J., 1991. Grain growth in porous olivine aggregates. Physics and Chemistry of Minerals 18, 269-278.

Nicolas, A., and Christensen N. I., 1987, Formation of anisotropy in upper mantle peridotites - A review., in Composition, structure and dynamics of the lithosphere-astenosphere system, edited by K. Fuchs and C. Froidevaux, AGU, Washingtown, D.C.

Nicolas, A., Boudier, F., Boullier, A.M., 1973. Mechanism of flow in naturally and experimentally deformed peridotites. American Journal of Science 273, 853-876.

Nicolas, A., Christensen, N.I., 1987. Formation of anisotropy in upper mantle peridotites: A review. Geodynamics Series 16, 111-123.

Nitsan, U., 1974. Stability field of olivine with respect to oxidation and reduction. J. Geophys. Res. 79, 706-711.

Novikov, V., Novikov, V.I.U.r.e., 1997. Grain growth and control of microstructure and texture in polycrystalline materials. CRC.

Paczkowski, K., Montési L. G., Long M. D., and Thissen C. J., 2014, Three-dimensional flow in the subslab mantle, Geochemistry, Geophysics, Geosystems, 15(10), 3989-4008.

Park, Y., Ree, J.-H., Kim, S., 2001. Lattice preferred orientation in deformed-then-annealed material: observations from experimental and natural polycrystalline aggregates. International Journal of Earth Sciences 90, 127-135.

Paterson, M.S., 1982. The determination of hydroxyl by infrared absorption in quartz, silicates glasses and similar materials. Bulletin de minéralogie 105, 20-29.

Paterson, M.S., Olgaard, D.L., 2000. Rock deformation tests to large shear strains in torsion. Journal of Structural Geology 22, 1341-1358.

Powers, J., Glaeser, A., 1998. Grain boundary migration in ceramics. Interface Science 6, 23-39.

Prior, D.J., Wheeler, J., 1999. Feldspar fabrics in a greenschist facies albite-rich mylonite from electron backscatter diffraction. Tectonophysics 303, 29-49.

Ramsay, J., 1967. Folding and fracturing of rock, MacGraw-Hill, New York.

Raterron, P., Chen, J., Li, L., Weidner, D., Cordier, P., 2007. Pressure-induced slip-system transition in forsterite: Single-crystal rheological properties at mantle pressure and temperature. Amer. Miner. 92, 1436-1445.

Raterron, P., Detrez F., Castelnau O., Bollinger C., Cordier P., and Merkel S., 2014, Multiscale modeling of upper mantle plasticity: From single-crystal rheology to multiphase aggregate deformation, Phys. Earth Planet. Inter., 228(0), 232-243.

Ribe, N.M., Yu, Y., 1991. A theory for plastic deformation and textural evolution of olivine polycrystals. Journal of Geophysical Research: Solid Earth (1978–2012) 96, 8325-8335.

Rios, P.R., 1997. Abnormal grain growth development from uniform grain size distributions. Acta Materialia 45, 1785-1789.

Rollett, A., Srolovitz, D., Anderson, M., 1989. Simulation and theory of abnormal grain growth—anisotropic grain boundary energies and mobilities. Acta metallurgica 37, 1227-1240.

Ruggles, T., Fullwood, D., 2013. Estimations of bulk geometrically necessary dislocation density using high resolution EBSD. Ultramicroscopy 133, 8-15.

Sachs, G., 1928, Plasticity problems in metals, Trans. Faraday Soc., 24, 84-92, doi:10.1039/TF9282400084.

Samyn, D., Svensson, A., Fitzsimons, S., 2008. Dynamic implications of discontinuous recrystallization in cold basal ice: Taylor Glacier, Antarctica. Journal of Geophysical Research: Earth Surface 113.

Savage, M., 1999. Seismic anisotropy and mantle deformation: What have we learned from shear wave splitting? Reviews of Geophysics 37, 65-106.

Savransky, D., and Kasdin N. J., 2012, An Efficient Method for Extracting Euler Angles from Direction Cosine Matrices, Unpublished manuscript, https://github.com/dsavransky/dynamicsMATLAB.

Schaeffer, A., Lebedev, S., 2013. Global shear speed structure of the upper mantle and transition zone. Geophysical Journal International.

Silver, P., Mainprice, D., Ismail, W.B., Tommasi, A., Barruol, G., 1999. Mantle structural geology from seismic anisotropy. Mantle Petrology: Field Observations and High Pressure Experimentation. A Tribute to Francis R.(Joe) Boyd, Y. Fei, C. Bertka, and BO Mysen, Eds., The Geochemical Society, Houston.

Silver, P.G., Chan, W.W., 1991. Shear wave splitting and subcontinental mantle deformation. Journal of Geophysical Research: Solid Earth 96, 16429-16454.

Silver, P.G., Savage, M.K., 1994. The interpretation of shear-wave splitting parameters in the presence of two anisotropic layers. Geophysical Journal International 119, 949-963.

Skemer, P., and Karato S.-i., 2008, Sheared lherzolite xenoliths revisited, J. Geophys. Res., 113(B7), B07205.

Skemer, P., Hansen, L.N., 2016. Inferring upper-mantle flow from seismic anisotropy: An experimental perspective. Tectonophysics 668-669, 1-14.

Skemer, P., Karato, S.-i., 2007. Effects of solute segregation on the grain-growth kinetics of orthopyroxene with implications for the deformation of the upper mantle. Physics of the Earth and Planetary Interiors 164, 186-196.

Skemer, P., Katayama, I., Jiang, Z., Karato, S.-i., 2005. The misorientation index: Development of a new method for calculating the strength of lattice-preferred orientation. Tectonophysics 411, 157-167.

Skemer, P., Sundberg, M., Hirth, G., Cooper, R., 2011. Torsion experiments on coarse-grained dunite: implications for microstructural evolution when diffusion creep is suppressed. Geological Society, London, Special Publications 360, 211-223.

Skemer, P., Warren, J.M., Hansen, L.N., Hirth, G., Kelemen, P.B., 2013. The influence of water and LPO on the initiation and evolution of mantle shear zones. Earth Planet. Sci. Lett. 375, 222-233.

Skemer, P., Warren, J.M., Hirth, G., 2012. The influence of deformation history on the interpretation of seismic anisotropy. Geochemistry, Geophysics, Geosystems 13.

Skemer, P., Warren, J.M., Kelemen, P.B., Hirth, G., 2010. Microstructural and Rheological Evolution of a Mantle Shear Zone. Journal of Petrology 51, 43-53.

Song, T.R.A., Kawakatsu, H., 2012. Subduction of oceanic asthenosphere: Evidence from sub-slab seismic anisotropy. Geophysical Research Letters 39.

Stöckhert, B., Duyster, J., 1999. Discontinuous grain growth in recrystallised vein quartz—implications for grain boundary structure, grain boundary mobility, crystallographic preferred orientation, and stress history. Journal of Structural Geology 21, 1477-1490.

Tanimoto, T., Anderson, D.L., 1985. Lateral heterogeneity and azimuthal anisotropy of the upper mantle: Love and Rayleigh waves 100–250 s. Journal of Geophysical Research: Solid Earth (1978–2012) 90, 1842-1858.

Taylor, G. I., 1938, Plastic strain in metals, J. Inst. Met., 62, 307-324.

Thompson, C., Frost, H., Spaepen, F., 1987. The relative rates of secondary and normal grain growth. Acta Metallurgica 35, 887-890.

Tommasi, A., 1998, Forward modeling of the development of seismic anisotropy in the upper mantle, Earth Planet. Sci. Lett., 160, 1-13.

Tommasi, A., Vauchez A., and Ionov D. A., 2008, Deformation, static recrystallization, and reactive melt transport in shallow subcontinental mantle xenoliths (Tok Cenozoic volcanic field, SE Siberia), Earth Planet. Sci. Lett., 272(1–2), 65-77.

Tommasi, A., Tikoff B., and Vauchez A., 1999, Upper mantle tectonics: Three-dimensional deformation, olivine crystallographic fabric and seismic properties, Earth Planet. Sci. Lett., 168, 173-186.

Tommasi, A., Knoll, M., Vauchez, A., Signorelli, J.W., Thoraval, C., Logé, R., 2009. Structural reactivation in plate tectonics controlled by olivine crystal anisotropy. Nature Geoscience 2, 423-427.

Tommasi, A., Mainprice, D., Canova, G., Chastel, Y., 2000. Viscoplastic self-consistent and equilibrium-based modeling of olivine lattice preferred orientations: Implications for upper mantle seismic anisotropy. J. Geophys. Res. 105, 7893-7908.

Toy, V.G., Prior, D.J., Norris, R.J., 2008. Quartz fabrics in the Alpine Fault mylonites: Influence of pre-existing preferred orientations on fabric development during progressive uplift. Journal of Structural Geology 30, 602-621.

Tullis, J., Yund, R.A., 1985. Dynamic recrystallization of feldspar: a mechanism for ductile shear zone formation. Geology 13, 238-241.

Turcotte, D.L., Oxburgh, E., 1972. Mantle convection and the new global tectonics. Annual Review of Fluid Mechanics 4, 33-66.

Van der Wal, D., Chopra, P., Drury, M., Gerald, J.F., 1993. Relationships between dynamically recrystallized grain size and deformation conditions in experimentally deformed olivine rocks. Geophysical Research Letters 20, 1479-1482.

Vauchez, A., F. Dineur, and R. Rudnick (2005), Microstructure, texture and seismic anisotropy of the lithospheric mantle above a mantle plume: insights from the Labait volcano xenoliths (Tanzania), Earth Planet. Sci. Lett., 232(3), 295-314, doi:10.1016/j.epsl.2005.01.024.

Vollmer, F.W., 1990. An application of eigenvalue methods to structural domain analysis. Geological Society of America Bulletin 102, 786-791.

Walker, A.M., Wookey, J., 2012. MSAT—A new toolkit for the analysis of elastic and seismic anisotropy. Computers & Geosciences 49, 81-90.

Wallis, D., Hansen, L.N., Britton, T.B., Wilkinson, A.J., 2016. Geometrically necessary dislocation densities in olivine obtained using high-angular resolution electron backscatter diffraction. Ultramicroscopy.

Warren, J. M., and Hirth G., 2006, Grain size sensitive deformation mechanisms in naturally deformed peridotites, Earth Planet. Sci. Lett., 248(1–2), 438-450.

Warren, J.M., Hirth, G., Kelemen, P.B., 2008. Evolution of olivine lattice preferred orientation during simple shear in the mantle. Earth and Planetary Science Letters 272, 501-512.

Webber, C., Newman, J., Holyoke III, C.W., Little, T., Tikoff, B., 2010. Fabric development in cm-scale shear zones in ultramafic rocks, Red Hills, New Zealand. Tectonophysics 489, 55-75.

Wendt, A.S., Mainprice, D., Rutter, E., Wirth, R., 1998. A joint study of experimental deformation and experimentally induced microstructures of pretextured peridotites. J. Geophys. Res. 103, 18205-18221.

Wenk, H., Van Houtte, P., 2004. Texture and anisotropy. Reports on Progress in Physics 67, 1367.

Wenk, H.-R., Armann, M., Burlini, L., Kunze, K., Bortolotti, M., 2009. Large strain shearing of halite: Experimental and theoretical evidence for dynamic texture changes. Earth and Planetary Science Letters 280, 205-210.

Wenk, H.R., Bennett, K., Canova, G.R., Molinari, A., 1991. Modelling plastic deformation of peridotite with the self-consistent theory. J. Geophys. Res. 96, 8337-8349.

Wenk, H.R., Christie, J.M., 1991. Review paper. Comments on the interpretation of deformation textures in rocks. Journal of Structural Geology 13, 1091-1110.

Wenk, H.R., Tomé, C.N., 1999. Modeling dynamic recrystallisation of olivine aggregates deformed in simple shear. J Geophys Res Solid Earth 104, 25513- 25527.

Wheeler, J., 2009, The preservation of seismic anisotropy in the Earth's mantle during diffusion creep, Geophysical Journal International, 178(3), 1723-1732.

Wilkinson, A.J., Meaden, G., Dingley, D.J., 2006. High resolution mapping of strains and rotations using electron backscatter diffraction. Materials Science and Technology 22, 1271-1278.

Wilson, C., 1982. Texture and grain growth during the annealing of ice. Textures Microstruct 5, 19-31.

Wolfe, C.J., Silver, P.G., 1998. Seismic anisotropy of oceanic upper mantle: Shear wave splitting methodologies and observations. Journal of Geophysical Research: Solid Earth 103, 749-771.

Yuan, H., Romanowicz, B., 2010. Lithospheric layering in the North American craton. Nature 466, 1063-1068.

Zahid, G., Huang, Y., Prangnell, P., 2009. Microstructure and texture evolution during annealing a cryogenic-SPD processed Al-alloy with a nanoscale lamellar HAGB grain structure. Acta Materialia 57, 3509-3521.

Zhang, S., Karato, S.-i., 1995. Lattice preferred orientation of olivine aggregates deformed in simple shear. Nature 375, 774-777.

Zhang, S., Karato, S.-i., Fitzgerald, J., Faul, U.H., Zhou, Y., 2000. Simple shear deformation of olivine aggregates. Tectonophysics 316, 133-152.

Zhao, Y.-H., Zimmerman, M.E., Kohlstedt, D.L., 2009. Effect of iron content on the creep behavior of olivine: 1. Anhydrous conditions. Earth and Planetary Science Letters 287, 229-240.